The Stellar Mass-Size Evolution of Galaxies From $z = 7$ to $z = 0$

Moein Mosleh

ISBN 978-90-8891-642-7

9 789088 916427 >

The Stellar Mass-Size Evolution of Galaxies From $z = 7$ to $z = 0$

PROEFSCHRIFT

ter verkrijging van
de graad van Doctor aan de Universiteit Leiden,
op gezag van de Rector Magnificus prof. mr. C. J. J. M. Stolker,
volgens besluit van het College voor Promoties
te verdedigen op woensdag 12 juni 2013
klokke 15.00 uur

door

Moein Mosleh
geboren te Shiraz, Iran
in 1980

Promotiecommisie

Promotor: Prof. dr. M. Franx

Co-Promoter: Dr. R. J. Williams   Carnegie Observatories
Overige leden: Prof. dr. H. J. A. Rottgering
              Prof. dr. K. Kuijken
              Dr. J. Brinchmann
              Prof. dr. J. Schaye
              Dr. A. Bunker   University of Oxford

To Mom, Dad and Mahsan

"Adam's sons are body limbs, to say;
For they're created of the same clay.
Should one organ be troubled by pain,
Others would suffer severe strain.
Thou, careless of people's suffering,
Deserve not the name, human being."

Saadi Shirazi

Contents

Introduction

1

1.1 History

At the beginning of the twentieth century, the Milky Way Galaxy was believed to occupy more or less the whole Universe. It was not until the 1920's that the existence of galaxies external to the Milky Way was established. Pioneering efforts by astronomers such as Edwin Hubble proved that many of the nebulae objects observed at the time, were indeed galaxies outside our Milky Way. Many external galaxies were found and observed afterwards. In order to address them in a convenient and easy way, astronomers classified these objects according to their structures and shapes, or in short, morphology. The first classification scheme for galaxies was introduced by Hubble (1926) and has become known as Hubble tuning fork. This system, which is still in use today breaks galaxies into *elliptical*, *lenticular*, *spiral*, *irregular*. and each can be divided into subclasses based on the existence of extra features such as bars. The differences between various types, in fact, reflect the differences in their physical properties. Since then, astronomers have attempted to quantify the physical properties of galaxies in detail.

Spiral galaxies were found to have different stellar populations than ellipticals. The amount of gas and recent star formation of these galaxies are distinct from the ellipticals and they have bluer colors. The stellar populations of elliptical galaxies are old with redder colors and they tend to be more massive than the spirals (Kauffmann et al. 2003, Blanton et al. 2005). In general, observed quantities such as color, shape, luminosity, current star-formation rate, stellar and dynamical mass, circular velocity and velocity dispersion are the empirical properties for distinguishing galaxies and studying their underlying physics. (See more in review by Blanton & Moustakas 2009)

The diversity of galaxy populations observed in the present-day Universe raised questions about the origin of these differences. Astronomers strive to discover the story of formation and evolution of galaxies in theoretical and observational frameworks. The theoretical framework established in the 1960-70's (e.g., Eggen et al. 1962, Sandage et al. 1970, Press & Schechter 1974) describes the formation of galaxies from gravitational instability of density perturbations in the dark matter distribution and condensation of gas.

According to galaxy formation theory, as the dark matter halo collapses, shock heating will cause the gas within that halo to cool. The cooling will eliminate the pressure of the gas, however, in order to prevent the gas from ending up all at the center, some initial angular momentum of gas (acquired via tidal torques in the early Universe) is required. This helps to assemble the gas into a rotating disk (see e.g., Mo et al. 1998). However, different models can use different assumptions for density profiles of the dark matter halos and also for the initial dependence of the gas angular momentum on their dark matter halos. It is also not clear whether the gas angular momentum can change with time or how the star formation and feedback processes have an effect on changes of the structural properties of galaxies, such as their sizes.

There are mainly two different scenarios for the formation of bulges of late-type galaxies: One assumes that they are formed through merging and the other process is based on disk instabilities. The formation of the bulge through merging of two or more galaxies requires accretion of cold gas later on to form a disk around the bulge. Consequently, the bulge component can potentially have different stellar population properties in com-

parison to the disk. In the disk-instability scenario, the low angular momentum material near the center will finally transfer into the bulge. Nevertheless, many other assumptions need to be taken into account (e.g., feedback processes) for a full understanding of the formation and evolution of a typical late-type galaxy.

The formation of early-type galaxies is also not well understood. One scenario for the formation of these galaxies is from mergers of galaxies. Based on simulations, mergers of disk galaxies can reproduce similar properties of a typical elliptical galaxy (e.g., Hernquist 1992). Although this general model can predict simple properties of these galaxies, many properties still do not agree with the observations.

Therefore, direct observations are essential to test galaxy formation models. These observations should not only include complete samples of nearby galaxies, but also require large samples of galaxies at earlier stages of the Universe. As a result, identification of the first and most distant galaxies started to become more important by the mid-1970's and still continues today. The frontier of distant galaxies moved to redshifts of $z \sim 1 - 4$ in the 1990's corresponding to lookback times of $\sim 7 - 12$ Gyr. Thanks to deep and ultra deep observations during the last decade, the samples of high redshift galaxies have substantially increased and the limit is now pushed further to $z \sim 10$ (Bouwens et al. 2012).

1.2 Galaxies at High Redshifts

Observations of galaxies at high redshifts reveal that their properties are very different compared to galaxies in the nearby Universe (e.g., Conselice & Arnold 2009, Ravindranath et al. 2006) and the Hubble sequence was not in place for most of the galaxies. Therefore, looking back to a time when galaxies are observed to have different physical properties is important for understanding galaxy evolution. This provides essential clues for interpreting how galaxies assembled their stellar masses and structures with time.

There have been several novel techniques developed for identifying galaxies at high redshifts (i.e., $z \gtrsim 1$) over the last two decades. These methods rely on particular features in galaxy spectral energy distributions. Multi-wavelength observations normally assist to find these features. Although these techniques have been efficient for detecting high-z galaxies, they are still suffering from incompleteness.

One of the first methods relies on the rest-frame UV color of galaxies. As the spectral energy distribution of distant galaxies is shifted to longer wavelengths, their rest-frame UV spectrum can be observed in optical filters. In addition, the flux short-ward of the Lyman limit is almost completely absorbed by neutral hydrogen in the intergalactic medium (IGM). The combination of these two phenomenon helped isolate UV-bright star-forming galaxies at $z \sim 3$ in the *UGR* color-color diagram. These galaxies are called Lyman Break Galaxies (LBGs) (Steidel et al. 1996). In order to detect galaxies at higher redshifts ($z \gtrsim 4$), this method was modified using redder sets of filters (e.g., Ouchi et al. 2004, Bouwens et al. 2007, 2011). Based on the rest-frame UV selection, star-forming galaxies at lower redshifts, $1.4 < z < 2.5$, are also selected (BM/BX galaxies: Adelberger et al. 2004, Steidel et al. 2004). Although this technique has been successful in detecting high

redshift star forming galaxies, this method misses passive or dusty star-forming galaxies at these redshifts.

Using another spectral feature of galaxies in their optical rest-frame (Balmer/4000 Å break), another technique was developed to isolate galaxies with negligible levels of star formation at $z \gtrsim 2$ (Franx et al. 2003). This technique benefits from using the observed color of galaxies in the near infrared filters ($J_{Vega} - K_{Vega} > 2.3$). These galaxies which are called Distant Red Galaxies (DRGs) typically dominate the high stellar mass regime of galaxies at $z \sim 2$. The other method based on optical/near Infrared color is the so-called *BzK* method developed by Daddi et al. (2004). This technique can isolate star-forming and passive galaxies at $1.4 \lesssim z \lesssim 2.5$.

Sub-millimetre galaxies (SMGs) (Smail et al. 1997, Hughes et al. 1998) are systems at high redshift with a large amount of radiation in the far-IR due to their obscured star-formation or AGN activity. They are very massive and luminous. However, their link to galaxies in the local Universe is not yet understood. Another efficient method for identifying high-z galaxies is using narrowband filter to detect galaxies with large hydrogen Lyα emission-line equivalent widths. These galaxies are normally faint and their relation to the other populations of galaxies are yet to be well resolved.

Although the sample size of galaxies at high redshift is increasing they are still much smaller than surveys of the local Universe such as the Sloan Digital Sky Survey (SDSS). However, the properties of these high redshift galaxies provide important insight for understanding the formation and evolution of galaxies.

1.3   Scaling Relations

One of the key unsolved problems in astrophysics is to understand the formation and evolution of galaxies. There are many complementary approaches to study the evolution of galaxies and infer how distant galaxies are connected to galaxies in the present day Universe. These canonical ways are either focused on the evolution of the luminosity/mass functions of galaxies, the evolution of the star formation rate/stellar mass density, or the evolution of the observed scaling relations of galaxies. For instance, the luminosity function describes the number density of galaxies within a small luminosity range. This can constrain the overall abundances of galaxies at each epoch, therefore the evolution of the luminosity function with redshift provides essential information for understanding the evolution history of galaxies.

Galaxies show great diversity in their physical parameters, such as luminosity, stellar mass, size and rotational velocity. Interestingly, galaxies obey well-defined scaling relations between some of these quantities. For instance, the relation between the luminosity and rotational velocity of spiral galaxies is know as a 'Tully-Fisher' relation (Tully & Fisher 1977) which basically defines a correlation between dynamical mass and the luminosity of galaxies. The relation between the velocity dispersion and luminosity of elliptical galaxies is known as a 'Faber-Jackson' relation (Faber & Jackson 1976) in which accordingly, elliptical galaxies with larger velocity dispersions are brighter.
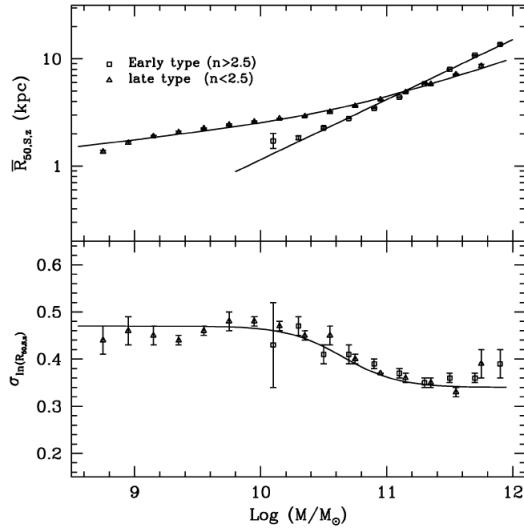
Figure 1.1 – The Stellar mass-size relation for late-type and early-type galaxies in the SDSS (top panel) and the size dispersion as a function of the stellar mass(bottom panel) from study by Shen et al. (2003)

It is essential to study the galaxy scaling relations over a wide range of redshifts. This can help to determine how galaxies move along these relations with time and accordingly, make it possible to test plausible model(s) for their evolution. In general, the slopes, zero points and scatters of these scaling relations at different epochs are fundamentally important to constrain models of galaxy formation.

However, there are some difficulties to obtain accurate measurements for some of the quantities used in these scaling relations. For instance, measuring the rotational velocity or velocity dispersion of the faint galaxies at high redshifts requires deep spectroscopic observations. Acquiring these quantities for a large sample of galaxies is a very time consuming process. Moreover, as the galaxies get fainter, the robustness of these measurements normally reduces. Therefore, constraining the correlations between some of these quantities becomes a difficult task for high redshift galaxies.

Among the scaling relations, the relation between the stellar mass and the size of galaxies has considerable importance. The size of galaxies can be measured using single-band imaging (photometry). The stellar mass of the galaxies can also be measured robustly, thanks to the multi-wavelength photometry and stellar population synthesis modelling. Therefore, there is less difficulties to estimate these properties for a larger sample of galaxies at high redshifts in comparison to some of the quantities mentioned above. In addition, the stellar mass and size of galaxies are two important ingredients for characterizing galaxies and have important physical meanings. Studying these quantities at different epochs will help investigate how the structures of the nearby galaxies have been
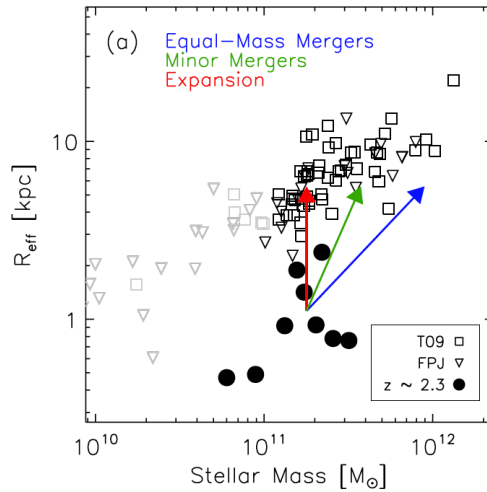
Figure 1.2 – The relative distributions of the stellar mass and size of quiescent galaxies at $z \sim 2$ and in the local Universe. The arrows show the predictions of evolution of sizes for each model with redshift. (Figure is taken From Bezanson et al. (2009).

formed and what were the properties of their progenitors at high redshifts. In brief, this can help to constrain evolutionary scenarios of galaxy formation and evolution.

The stellar mass-size relation of galaxies in the present day Universe is pointed out first in Kauffmann et al. (2003) and well characterized by Shen et al. (2003), using large samples of galaxies in the Sloan Digital Sky Survey (SDSS). The top panel of Figure 1.1 shows the mass-size relation for late-type and early-type galaxies studied by Shen et al. (2003). The relation is shown to be different for late-type and early-type galaxies. The early-types have a steeper relation at high stellar mass. This reflects the different history of formation and the stellar mass assembly for each kind of galaxy. The size dispersions (bottom panel of Figure 1.1) also vary as a function of the stellar mass and the scatter decreases for massive galaxies.

Pioneering studies on the sizes of galaxies at higher redshifts were carried out in the 1990's (e.g., LBGs at $z \sim 3$ by Giavalisco et al. (1996) or Lilly et al. (1998) for galaxies up to $z \sim 1$.) However, the results of different studies were not in agreement due to difficulties in obtaining a large sample of galaxies at higher redshifts and the selection effects caused by surface brightness limits. However, the study of the size-luminosity relation of galaxies improved later, using deep ground and space based observations. These studies revealed that the sizes of galaxies at earlier time were smaller compare to galaxies in the local universe within a similar mass/luminosity range (e.g., Trujillo et al. 2006b, Zirm et al. 2007, van Dokkum et al. 2008). This means that sizes of massive galaxies within a given stellar mass should have been increased up to a factor of ~ 6 with time.

The process of size growth for galaxies can be different for each type and can vary at

each epoch. Star-forming galaxies at high redshifts (e.g., at $z \sim 2$), have a larger fraction of gas per stellar mass compare to their counterparts at low redshifts (e.g., Erb et al. 2006). One plausible scenario for increasing sizes of these galaxies could be the accretion of gas into the disk (cold accretion) and converting that into stars (e.g., Law et al. 2012).

Observations have also illustrated that early-type galaxies at high redshifts are significantly smaller. There are two main questions about these galaxies; first is how these galaxies are formed at high redshift and second is to understand how they are connected to their low redshift analogs. The formation of these compact quiescent galaxies at high redshifts are yet to be understood. Nevertheless, there are several mechanisms proposed to explain the growth of these quiescent galaxies with time, such as major mergers, minor mergers or adiabatic expansion (e.g., Khochfar & Silk 2009, Naab et al. 2009, Bezanson et al. 2009, Fan et al. 2008). These mechanisms can change the stellar mass and profiles of galaxies in different way.

The observed stellar mass-size relation of these massive quiescent galaxies would help to constrain these models. Equal-mass merging of gas-poor systems (major mergers), could double sizes and stellar masses of these galaxies. Minor mergers, can increase the size of spheroids more significantly than the stellar masses, because this process nearly conserves the central densities and velocity dispersions. The puffing up scenario via adiabatic expansion, suggests the idea of expelling a large amount of material efficiently, through some sort of feedbacks (e.g., quasar feedback); however, in this process, the central density and velocity dispersion of a typical early-type galaxy will change. (see Figure 1.2 for more details). In general, comparing observed scaling relations at different redshifts (epochs) with results from simulations can help to verify different scenarios of galaxy formation and evolution.

1.4   This Thesis

The uncertainties associated with the observed properties of galaxies can be further improved by additional observations using deeper data that covers larger area and well-defined complete samples. The multi-wavelength surveys are potent tools for these studies. Using the advantages of recent infrared galaxy surveys, with the aid of ancillary optical and near infrared data, make it possible for observers to study the properties of different kinds of galaxies at a wide range of redshifts and pushing the observational limits to the epoch of galaxy formation ($z \sim 10$).

This thesis focuses on assessing how the structural properties such as the sizes and the surface brightness profiles of galaxies change with time. In particular, we study the stellar mass-size relation of galaxies from $z = 7$ to $z = 0$, using recent deep observations in the near Infrared. Using deep optical and near-IR surveys, helped to characterize the spectral energy distributions (SEDs) of galaxies at a wide range of redshifts, especially at the peak of star-formation activity ($z \sim 2$). Studying galaxy properties and the scaling relations at different epochs can place important constrains on the underlying processes assumed for galaxy mass and structural assembly (e.g., accretion of gas onto galaxies or minor/major

mergers), feedback effects.

Chapter 2: In this chapter, we present the first study of galaxy size evolution using a sample of objects with spectroscopic redshifts between $z \sim 0.5 - 3.5$ in the GOODS-North field. Most studies use photometric redshifts to measure the evolution of mass-size relations with time. Using spectroscopic samples can remove some biases based on photometric studies. We further investigate the half-light radii of different types of UV-bright star-forming galaxies at high redshifts; i.e., sizes of galaxies such as Lyman Break Galaxies, BM/BX galaxies and Lyman Break analog at $z \sim 1$ are measured. In addition, we compare the sizes of these galaxies with other types of star-forming galaxies, such as star-forming *BzKs* and sub-millimeter galaxies (SMGs). The positions of these galaxies on the mass-size plane may provide clues about their relation to other galaxy populations.

Chapter 3: The newly installed Wide Field Camera 3 (WFC3) camera on the *Hubble Space Telescope* and the ultra-deep near-infrared imaging of the Hubble Ultra Deep Field (HUDF) helped to identify numerous candidates of Lyman Break Galaxies (LBGs) to the early stages of galaxy formation (e.g., out to $z \sim 8$). Many studies have focused on the evolution of the luminosity function, stellar mass and star-formation rates of the LBGs at these high redshifts (e.g., Bouwens et al. 2011, Gonzalez et al. 2011). However, the stellar mass-size relation of these galaxies at $z \gtrsim 4$ were not addressed in great detail. Therefore, in this chapter we take advantage of the ultra-deep WFC3/IR and IRAC observations in the HUDF and Early Release Science (ERS) field to study the stellar mass-size relation of LBGs out to the redshift of $z \sim 7$. At $z \gtrsim 4$, the rest-frame optical light shifts to mid-IR wavelengths, which is a problem in determining stellar masses. The Spitzer telescope provides very sensitive photometry at these wavelengths, but its large PSF can cause blending problems. However, robust techniques have been developed to deblend nearby objects and measure the stellar mass of high-z galaxies reliably (Labbé et al. 2006). In addition, we have used the profile fitting technique (assuming Sérsic models) to measure the sizes of these very high redshift galaxies, in a consistent way to the lower redshift analysis. Therefore, we study the stellar mass-size relation of galaxies up to $z \sim 7$.

Chapter 4: The stellar mass-size relation of galaxies in the present day Universe can be used as a baseline for inferring the rate of galaxies size evolution with time. Therefore, in this chapter we study the mass-size relation for a sample of galaxies at $z = 0.01 - 0.02$, dividing the sample based on different common methods of classifications. We also examined different methods of size measurements of galaxies, including single Sérsic fits, two-component Sérsic models and non-parametric method, in order to quantify the systematics associated in each method. Finally, to test the potential systematics of size measurements at high redshift, we further artificially redshifted our sample to z=1 and re-fit the galaxies using single Sérsic profile fitting.

Chapter 5: It has been shown by many studies that the majority of galaxies follow a color-morphology relation up to high redshifts. In the other words, the morphological transformation and cessation of star-formation could be correlated. However, presence

of a population of red or passive spiral galaxies (with a lack of ongoing star-formation) which was first noticed by van den Bergh (1976) and Couch et al. (1998) appears to break this relation. In this chapter we carefully selected face-on disk dominated spiral galaxies (at $z \sim 0$) from the Galaxy Zoo morphological catalogue (visually selected) to construct a sample of truly passive disk galaxies. We attempt to investigate various physical processes that shut down the star-formation of these red passive spiral galaxies while retaining their spiral morphology. We study the dust properties and stellar populations of these galaxies in comparison with blue face-on spiral galaxies. In addition we also examined the environmental properties of these galaxies and looked for AGN activity. We have also tried to compare the fraction of objects with specific morphological features (such as bars) between red and blue face-on spirals.

1.5 Conclusion and Outlook

We provide some constraints on the galaxy formation and evolution models and also the methods of measuring structural properties of galaxies at different redshifts. Our results confirm previous studies of the mass-size relation at high redshift based on photometric redshifts, and we showed that galaxies of similar mass were generally smaller in the past. We also show that the stellar mass-size relation of Lyman-break galaxies persists, at least to $z \sim 5$. We find that the best fitting size evolution for galaxies with stellar masses of $\log(M_*/M_\odot) \sim 10.$ evolves as $(1+z)^{-1.20\pm0.11}$. This evolution is very similar for the galaxies with lower stellar masses of $\log(M_*/M_\odot) \sim 9$. This results is in agreement with simple theoretical galaxy formation models at high redshifts.

We compared the sizes of UV-bright galaxies and Sub-mm galaxies and we found that the median effective radius of the Sub-mm galaxies are consistent with the BM/BX galaxies within the same stellar masses. We also confirmed that the star-forming galaxies (at $z \sim 1-3$) are significantly larger than quiescent galaxies at the same mass and redshift by 0.45 ± 0.09 dex. We also confirmed the tight correlation between color and stellar mass surface density of galaxies at high redshifts using our sample of galaxies with secure redshifts. This demonstrate that galaxies with higher specific star-formation rates have larger effective radii than the ones with lower specific star-formation rates.

A larger sample of galaxies with deeper observations at their rest-frame optical for galaxies at $z \gtrsim 3$ is required to robustly constrain many other properties of these galaxies. It would also be interesting to understand the role of environment and intergalactic medium in shaping the morphologies or structural properties of galaxies. Comparing the stellar mass/star-formation rate profiles of galaxies at different environment can provide more clues on the galaxy evolution scenarios. Using larger spectroscopic samples of galaxies at high redshifts will also help to constrain the galaxies evolution models.

We showed that the stellar-mass size relation of both nearby late-type and early-type galaxies are steeper at high masses ($\sim 3-4 \times 10^{10} M_\odot$) and flatten at low stellar masses. This relation is not sensitive to the precise definition of the sample classification based on color, Sérsic index, morphology and specific star formation rate, with the exception of

blue galaxies which follow a somewhat higher and steeper relation.
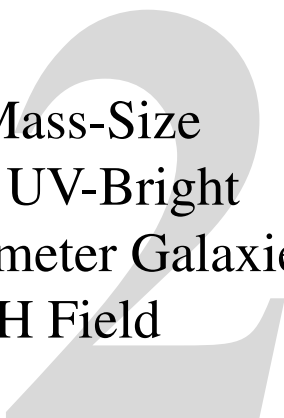
In this thesis we also investigated the systematics of different methods of size measurements for galaxies at low and high redshift. We show that nearby early-type galaxies with stellar masses $> 2 \times 10^{10} M_{\odot}$ are not well fit with single Sérsic profiles. The non-parametric methods and two component fits give less biased measurements for the sizes of these well-resolved galaxies. However, single Sérsic fit provide robust size estimates for galaxies at high redshifts.

The results from studying face-on red spiral galaxies showed that these galaxies indeed have older stellar populations and they do not have large amount of dusts. Although the findings show that these galaxies are common around or just inside the infalling regions of clusters, however, the environment alone cannot turn these galaxies red. Their AGN luminosity is also not enough for the difference between them and blue spirals. The fraction of red spiral galaxies with bar features is larger than blue ones and hence this suggests that the cessation of star-formation is strongly correlated with the bar instabilities in spiral galaxies.

Bibliography

Adelberger, K. L., Steidel, C. C., Shapley, A. E., Hunt, M. P., Erb, D. K., Reddy, N. A., & Pettini, M. 2004, ApJ, 607, 226

Bezanson, R., van Dokkum, P. G., Tal, T., Marchesini, D., Kriek, M., Franx, M., & Coppi, P. 2009, ApJ, 697, 1290

Blanton, M. R., Eisenstein, D., Hogg, D. W., Schlegel, D. J., & Brinkmann, J. 2005, ApJ, 629, 143

Blanton, M. R., & Moustakas, J. 2009, ARA&A, 47, 159

Bouwens, R. J., Illingworth, G. D., Franx, M., & Ford, H. 2007, ApJ, 670, 928

Bouwens, R. J., et al. 2011, ApJ, 737, 90

—. 2012, arXiv:1211.3105

Conselice, C. J., & Arnold, J. 2009, MNRAS, 397, 208

Couch, W. J., Barger, A. J., Smail, I., Ellis, R. S., & Sharples, R. M. 1998, ApJ, 497, 188

Daddi, E., Cimatti, A., Renzini, A., Fontana, A., Mignoli, M., Pozzetti, L., Tozzi, P., & Zamorani, G. 2004, ApJ, 617, 746

Eggen, O. J., Lynden-Bell, D., & Sandage, A. R. 1962, ApJ, 136, 748

Erb, D. K., Steidel, C. C., Shapley, A. E., Pettini, M., Reddy, N. A., & Adelberger, K. L. 2006, ApJ, 646, 107

Faber, S. M., & Jackson, R. E. 1976, ApJ, 204, 668

Fan, L., Lapi, A., De Zotti, G., & Danese, L. 2008, ApJ, 689, L101

Franx, M., et al. 2003, ApJ, 587, L79

Giavalisco, M., Steidel, C. C., & Macchetto, F. D. 1996, ApJ, 470, 189

González, V., Labbé, I., Bouwens, R. J., Illingworth, G., Franx, M., & Kriek, M. 2011, ApJ, 735, L34+

Hernquist, L. 1992, ApJ, 400, 460

Hubble, E. P. 1926, ApJ, 64, 321

Hughes, D. H., et al. 1998, Nature, 394, 241

Kauffmann, G., et al. 2003, MNRAS, 341, 54

Khochfar, S., & Silk, J. 2009, MNRAS, 397, 506

Labbé, I., Bouwens, R., Illingworth, G. D., & Franx, M. 2006, ApJ, 649, L67

Law, D. R., Steidel, C. C., Shapley, A. E., Nagy, S. R., Reddy, N. A., & Erb, D. K. 2012, ApJ, 745, 85

Lilly, S., et al. 1998, ApJ, 500, 75

Mo, H. J., Mao, S., & White, S. D. M. 1998, MNRAS, 295, 319

Naab, T., Johansson, P. H., & Ostriker, J. P. 2009, ApJ, 699, L178

Ouchi, M., et al. 2004, ApJ, 611, 660

Press, W. H., & Schechter, P. 1974, ApJ, 187, 425

Ravindranath, S., et al. 2006, ApJ, 652, 963

Sandage, A., Freeman, K. C., & Stokes, N. R. 1970, ApJ, 160, 831

Shen, S., Mo, H. J., White, S. D. M., Blanton, M. R., Kauffmann, G., Voges, W., Brinkmann, J., &

Csabai, I. 2003, MNRAS, 343, 978

Smail, I., Ivison, R. J., & Blain, A. W. 1997, ApJ, 490, L5

Steidel, C. C., Giavalisco, M., Pettini, M., Dickinson, M., & Adelberger, K. L. 1996, ApJ, 462, L17+

Steidel, C. C., Shapley, A. E., Pettini, M., Adelberger, K. L., Erb, D. K., Reddy, N. A., & Hunt, M. P. 2004, ApJ, 604, 534

Trujillo, I., et al. 2006b, ApJ, 650, 18

Tully, R. B., & Fisher, J. R. 1977, A&A, 54, 661

van den Bergh, S. 1976, ApJ, 206, 883

van Dokkum, P. G., et al. 2008, ApJ, 677, L5

Zirm, A. W., et al. 2007, ApJ, 656, 66

The Evolution of the Mass-Size Relation to $z = 3.5$ for UV-Bright Galaxies and Submillimeter Galaxies in the GOODS-NORTH Field

Moein Mosleh, Rik J. Williams, Marijn Franx, Mariska Kriek

Abstract

We study the evolution of the size-stellar mass relation for a large spectroscopic sample of galaxies in the GOODS North field up to $z \sim 3.5$. The sizes of the galaxies are measured from K_s-band images (corresponding to rest-frame optical/NIR) from the Subaru 8 m telescope. We reproduce earlier results based on photometric redshifts that the sizes of galaxies at a given mass evolve with redshift. Specifically, we compare sizes of UV-bright galaxies at a range of redshifts: Lyman-break galaxies (LBGs) selected through the U-drop technique ($z \sim 2.5$-3.5), BM/BX galaxies at $z \sim 1.5$-2.5, and *GALEX* LBGs at low redshift ($z \sim 0.6$-1.5). The median sizes of these UV-bright galaxies evolve as $(1 + z)^{-1.11 \pm 0.13}$ between $z \sim 0.5$ and 3.5. The UV-bright galaxies are significantly larger than quiescent galaxies at the same mass and redshift by 0.45 ± 0.09 dex. We also verify the correlation between color and stellar mass density of galaxies to high redshifts. The sizes of submillimeter galaxies in the same field are measured and compared with BM/BX galaxies. We find that the median half-light radius of SMGs is 2.90 ± 0.45 kpc, and there is little difference in their size distribution to the UV-bright star-forming galaxies.

2.1 Introduction

Recent studies provide evidence that sizes of galaxies at high redshifts were smaller in comparison with galaxies of similar mass in the local universe (e.g., Daddi et al. 2005, Trujillo et al. 2006a,b, Zirm et al. 2007, Toft et al. 2007, van Dokkum et al. 2008a, Franx et al. 2008, Williams et al. 2010, Toft et al. 2009, Damjanov et al. 2009, Cimatti et al. 2008, Longhetti et al. 2007). These studies pose several questions about the evolution of properties of galaxies and the build-up of galaxy stellar mass with time. Several physical processes are proposed to explain the growth of galaxies with time, such as galaxy (major or minor) mergers (e.g., Khochfar & Silk 2006, 2009, Bell et al. 2006, Naab et al. 2009), gas accretion in outer regions, and star formation (e.g., Dekel et al. 2009, Elmegreen et al. 2008). However, each of these mechanisms will affect differently the growth of mass and size of galaxies. For example, major dry mergers could produce descendants with larger than observed stellar masses for early-type galaxies. Therefore, some authors (e.g., van Dokkum et al. 2010, Bezanson et al. 2009, Naab et al. 2009, Hopkins et al. 2009) suggest minor mergers and envelope growth by satellite accretion to be a more likely mechanism for building up quiescent galaxies. In general, plausible models have to reproduce galaxy sizes and stellar mass densities seen today and bring the high-redshift galaxies to the local stellar mass-size relation. Therefore, exploring the observed evolution of galaxy sizes is essential to constrain these galaxy formation and evolution models.

However, most of the size studies at high redshift were based on photometric redshifts. Although techniques to construct galaxy spectral energy distributions (SEDs) from multiwavelength observations and photometric redshift measurements are improved over the past few years, photometric redshifts still have worse uncertainties for star-forming galaxies due to the lack of a strong 4000Å break. The large uncertainties and possible systematic biases due to the reliance on photometric redshifts can seriously affect the masses and star formation rate measurements and thus the final results. Spectroscopic observations of high-redshift galaxies and making complete magnitude limited samples require large amounts of observing time. Nevertheless, the advent of 8-10m class telescopes with multi-object spectroscopy has brought about much larger high-z spectroscopic samples than were previously available.

Spectroscopic redshifts are relatively easier to obtain for star-forming galaxies (compare to quiescent galaxies) due to emission lines. Previous results on the size evolution of this population (with photometric redshifts) are interesting since some of the usual mechanisms assumed for size growth, e.g., gas-poor ("dry") mergers do not apply to gas-rich starburst galaxies since substantial amounts of gas are required for these galaxies to undergo significant star formation. Therefore, studies of the structure of star-forming galaxies with secure redshifts can provide strong constraints on size evolution models.

The actively star-forming galaxies at high redshift consists of two main populations: relatively unobscured UV-bright galaxies and dusty red starbursts, the most extreme of which are detected as submillimetre galaxies (SMGs). The UV-bright galaxies are selected to have strong rest-frame UV. In the past few years, many simple photometric techniques (e.g., "U-dropout") were designed to select these galaxies at different redshift ranges (e.g., Steidel et al. 2003, Adelberger et al. 2004).

The SMGs are among the most massive, luminous, and vigorously star-forming galaxies at high redshift that are heavily obscured by dust (e.g., Hughes et al. 1998, Smail et al. 2002, Chapman et al. 2003, 2005). The physical process driving these highly luminous galaxies (star formation, active galactic nucleus (AGN), or combination of these two) is still uncertain. The evolution of SMGs and their relation to the local galaxies are also not yet understood: for instance, whether or not SMGs are the progenitors of local elliptical galaxies (e.g., Blain et al. 2004, Swinbank et al. 2006, Tacconi et al. 2008). Their position on the size-mass plane may therefore provide clues about their relation to other galaxy populations.

To verify previous results based on photometric redshifts, here we study the mass and size evolution of a large sample of UV-bright and SMGs in Great Observatories Origin Deep Survey-North (GOODS-North) with secure spectroscopic redshifts. The structure of this paper is as follows. In Section 2.2, we review the data. In Section 2.3 and 2.4, we describe size and mass determinations of galaxies. Our selected subsamples are described in Section 2.5. Finally, in Section 2.6, we present our results and investigate the size evolution and stellar mass-size relation for our samples. We summarize and discuss our results in Section 2.7. The cosmological parameters adopted throughout this paper are $\Omega_m = 0.3$, $\Omega_\Lambda = 0.7$, and $H_0 = 70$ km s^{-1} Mpc^{-1}.

2.2   Description of Data

The sample of galaxies used here is based on the most complete spectroscopic catalog of galaxies in the GOODS-North field (Giavalisco et al. 2004)) by Barger et al. (2008). This catalog gives a compilation of all spectroscopic observations carried out in this field (e.g., Cowie et al. 2004, Reddy et al. 2006, Wirth et al. 2004, Cohen 2001, Cohen et al. 2000), where each galaxy sample was selected in a different way. In addition, Barger et al. (2008) performed spectroscopic observations for certain subsamples. The catalog includes 2907 sources including stars and is restricted to sources with $K_{s,AB} < 24.5$ or $F850LP_{AB} < 26$. There are 2362 sources with $z < 1.6$ and 327 sources between $z = 1.6$ and 3.5. Most redshifts for galaxies with $z > 1.6$ come from Reddy et al. (2006).

This catalog (Barger et al. 2008) comprises optical photometric data in the F435W, F606W, F775W, and F850LP passbands taken from *Hubble Space Telescope (HST)* Advanced Camera for Surveys (ACS; Giavalisco et al. 2004), and the *U*-band magnitude is taken from Capak et al. (2004). The near-infrared K_s-band magnitude measured from WIRCam images from the Canada-France-Hawaii Telescope. Details of near-IR observations, data reduction and generating catalog are described more in Barger et al. (2008). X-ray soft ($0.5 - 2$ KeV) and hard ($2 - 8$ KeV) luminosities are also provided for many sources in the catalog. In Barger et al. (2008) sources with X-ray luminosities above 10^{42} ergs s^{-1} in either soft or hard band defined as AGNs. For a fraction of sources ($\sim 36\%$) near-ultraviolet (NUV) and far-ultraviolet (FUV) magnitudes from the UV imaging survey performed by *GALEX* mission were also provided. Note that sources indicated as stars in the catalog are excluded from our analysis.

2.3 Sizes

2.3.1 Size Measurements

Size determination in the observed near-infrared (rest-frame optical at high z) is more robust in tracing the distribution of stellar mass than the observed optical (rest-frame UV at high z) since the sizes at rest-frame UV can be strongly affected by dust and star formation. Therefore, we use K_s-band images from Subaru MOIRCS Deep Survey (MODS) in the GOODS-North field (Kajisawa et al. 2006, Ouchi et al. 2007). The imaging observations are performed for J and K_s bands over ~ 112 arcmin^2 area of the GOODS-N field with a pixel scale of 0.12 arcsec. We used the images reduced by Bouwens et al. (2008). The resulting FWHM of the K_s images is $\sim 0.5''$. The deepest data cover ~ 28 arcmin^2 reaching a 5σ of 25.4 AB mag in K_s band while the other regions are ~ 1.3 mag shallower. More details of the images and data reduction can be found in Bouwens et al. (2008).

Sizes of galaxies were estimated by using the GALFIT code (Peng et al. 2002) in a similar procedure used by Trujillo et al. (2007) and Williams et al. (2010). For each galaxy, a square postage stamp of 120 pixels (14.4") around each galaxy was made, and we use a mask to exclude neighboring galaxies from the fit. A range of Sérsic (1968) profile models convolved with the point-spread function (PSF) of the image are fitted to the K_s images of galaxies. The convolved models for each object were compared with the galaxy surface brightness distribution and the best-fit model determined using minimized χ^2 of the fit. The PSF used by GALFIT was taken from the median of the unsaturated stars over the entire MOIRCS K_s images. We perform a test to check the PSF of the image by measuring sizes of a number of stars in the field listed in the Barger et al. (2008) catalog. The derived sizes of all the stars are found to be $\ll 0.02$ pixel (effectively zero). Therefore, the PSF is a good approximation of a point source. We note that within our K_s-band images, there is a shallower region with seeing of $0.68''$. We followed a similar procedure with an appropriate PSF (which is made from the median of stars in this region) to measure sizes of galaxies in this region separately. We also verified that the derived sizes of the shallower region are reliable by its appropriate PSF.

We determine the circularized effective radius $r_e = a_e \sqrt{(1 - \epsilon)}$, from the half-light radius along the semimajor axis a_e and ellipticity (ϵ) as output by GALFIT. This removes the effects of ellipticity. We allowed the Sérsic index n (which measures the shape of the surface brightness profile of galaxy) to vary between 0.5 and 5 and the effective radius between 0.01 and 60 pixels (0.0012$''$ and 7.2$''$). Initial guesses for the effective radius r_e, ellipticity, and position angle were taken from the SExtractor catalog, and magnitude was taken from the original (Barger et al. 2008) catalog, and we set the Sérsic index to 2 initially.

Our results show that the median Sérsic index measured for all galaxies is 2.0 where 50% of measurements lies between 4.0 and 1.0. For galaxies with stellar masses between 10^{10} and $10^{11} M_\odot$, the median Sérsic index is 2.4 where 50% lies between 4.6 and 1.2.

Due to possibility of color gradients, it is best to use the same rest-frame band for measuring sizes of galaxies at all redshifts. However, only deep K imaging is available,
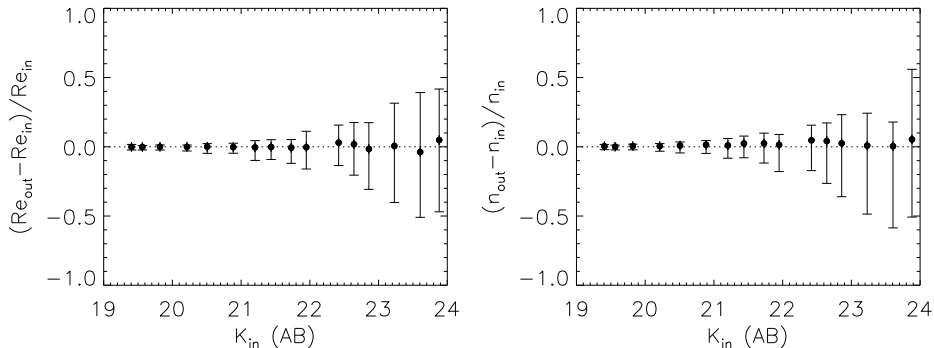
Figure 2.1 – Left panel: the points are the median of the relative difference between the recovered and input sizes vs. magnitude based on our simulations. Right panel: the same comparison, but for the relative difference between output and input Sérsic index. The error bars illustrate the 68% scatter. The random uncertainties of recovered sizes and Sérsic index increase with magnitude.

so there is a possibility of systematic effects with redshift. Franx et al. (2008) show that such systematic effects are small and will not significantly affect the results. As an approximation, we corrected sizes to the rest-frame g band using star-forming galaxies from studies of GOODS-Chandra Deep Field-South (CDF-South; Franx et al. 2008). We derive the best linear fit to the median of the ratio of sizes in K band and rest-frame g band as a function of redshift and apply this fit ($r_{e,k-band}/r_{e,g-band} = 0.15z + 0.64$) to galaxies with $z \lesssim 2$ in our sample.

2.3.2 Simulations

To gauge the accuracy of the measured sizes and reliability of our results, we perform a realistic simulation. About 8500 Sérsic profiles were generated with uniformly distributed random parameters in the ranges of $19 < K_{AB} < 25$, $0.1'' < r_e < 2''$, $0.5 < n < 5$ and $0 < \epsilon < 0.8$. The mock galaxies were then convolved with the PSF of the image. Finally, we added these galaxies to 14.4" blank-sky postage stamps randomly taken from our K_s-band image. The structural parameters of the model galaxies were then measured in a manner identical to that used for the actual images.

The results of these simulations are shown in Figures 2.1 and 2.2. The left panel of Figure 2.1 shows that the scatter in the recovered sizes increases with magnitude. The random uncertainties increase significantly after $K_{AB} = 23$. However, the systematic errors are very small ($< 5\%$) even at the faintest magnitudes. Moreover, the simulation shows that the systematic errors on recovery of the Sérsic index are also very small and random uncertainties increase above $K = 23$ (right panel of Figure 2.1). From this result, we limit the sample studied in this paper to galaxies with $K \leq 23$ mag. We note that this

limit is for the deeper region in our K-band images. Running a separate simulation for the shallower region, we find that the derived sizes of galaxies with $K < 22.7$ mag are reliable. Hence, we restricted the sample in this region to this slightly brighter magnitude limit.

We have also explored how the recovery of size depends on the size itself. As shown in Figure 2.2, the uncertainties in retrieving sizes depend on both magnitude and size. Systematic offsets at all magnitudes appear to be negligible except for $r_e > 1.8$ arcsec (which corresponds to 14.4 kpc at $z \sim 1$) at the faintest magnitudes; however, galaxies this large and faint have not been seen at any redshift.

The random uncertainties increase with size in all magnitude bins. For objects with $K_{AB} \leq 20$ mag (top panel), the random uncertainties in size recovery are $< 5\%$. However, for galaxies with $21 < K_{AB} < 22$ the increasing of random uncertainties with sizes is significant. The increase in random uncertainties at larger sizes could be due to decreasing of surface brightness. However, since we are mainly concerned about the overall sample properties, the lack of systematic errors is more important.

2.4   Stellar Mass estimates

The stellar masses of galaxies were measured with the Fitting and Assessment of Synthetic Templates (FAST) code (Kriek et al. 2009). All fluxes from Barger et al. (2008) including four optical bands from ACS, the K_s infrared and U band were used to find the best-fit galaxy template SED to the broadband photometry using a χ^2 minimization procedure. The Bruzual & Charlot (2003) stellar population evolution models with exponentially declining star formation histories (with τ ranging from 10^{7-10} yr) were used to fit the SEDs. We use the Salpeter (1955) initial mass function (IMF) and solar metallicity and the extinction A_V was allowed to vary between 0 and 3. Redshifts of galaxies were fixed to their spectroscopic redshift provided by Barger et al. (2008) catalog. Masses were then shifted by -0.2 dex for consistency with the $z \sim 0$ Sloan Digital Sky Survey (SDSS) masses (which were calculated using a Kroupa 2001 IMF).

2.5   Subsamples

The ability to identify and study distant galaxies has improved dramatically during the last two decades. Various selection criteria have been designed to select high-redshift galaxies through their observed colors. In this paper, we use such criteria to select samples of UV-bright galaxies in redshift ranges of $0.6 \leq z \leq 1.4$, $1.4 \leq z \leq 2.5$ and $2.7 \leq z \leq 3.5$.

Our sample of Lyman-break galaxies (LBGs; $2.7 \leq z \leq 3.5$) is taken from Reddy et al. (2006). Their LBG candidates were originally preselected by the "C", "D", and "MD" criteria which use regions of $(U_n - G)$ versus $(G - R)$ color space (Steidel et al. 2003). Limiting our sample to $K_{AB} \leq 23$, we were only able to include five LBGs in our analysis.
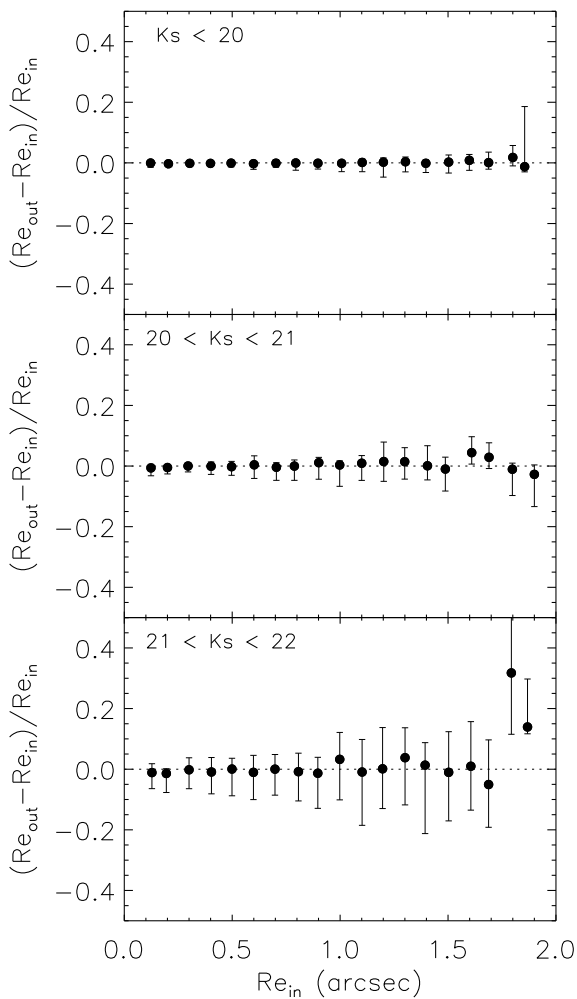
Figure 2.2 – Relative difference between the input and measured sizes of galaxies in our simulations as a function of size for mock galaxies for galaxies with $K_{AB} \leq 20$ mag (top panel), $20 < K_{AB} < 21$ (middle panel), and $21 < K_{AB} < 22$ (lower panel). The relative errors between the input and measured sizes of galaxies as a function of sizes depend on the magnitude.

Table 2.1 – Subsamples

Sample	Redshift	$\log(M_*/M_\odot)$	No. of Sources
BM/BX	$1.4 < z < 2.7$	9.8 - 10.8	41
LBG	$2.7 < z < 3.5$	10.2 - 10.8	5
SMG	$0.5 < z < 3.$	10.0 - 11.7	14
sBzK	$1.4 < z < 3.2$	9.8 - 11.7	70

Notes. Samples of star-forming galaxies studied in this paper.

At $z \sim 2$, BM/BX galaxies also are taken from Reddy et al. (2006). The BM/BX criteria (Adelberger et al. 2004, Steidel et al. 2004) were designed to find actively star-forming galaxies at redshifts $1.4 < z < 2.5$ with similar SEDs to the LBGs. The selection criteria are based on the observed U_nGR colors of galaxies. Reddy et al. (2006) provided spectroscopic observations for candidates brighter than $R_{AB} = 25.5$, photometrically selected from Steidel et al. (2003, 2004). For this paper, 41 BM/BX galaxies to $K_{AB} = 23$ are selected from their sample with spectroscopic redshift $z > 1.4$.

Galaxies analogous to the LBGs at $0.6 \leq z \leq 1.4$ (hereafter *GALEX*/LBGs) are selected with the *GALEX/HST* $(FUV - NUV)_{AB}$ versus $(NUV - F435W)_{AB}$ color-color diagram. Following the selection criteria used in Barger et al. (2008) and requiring $z > 0.6$, we include 105 *GALEX*/LBGs with $K_{AB} \leq 23$.

In addition to the UV-bright galaxies in GOODS-N field, we also study sizes of the SMGs as a population of star-forming galaxies at high redshifts. The subsample of SMGs for our studies is drawn from Chapman et al. (2005) and Pope et al. (2006). The catalog of SMGs provided by Pope et al. (2006) contains 35 candidates from GOODS-N field with 21 secure optical counterparts. Of these, only eight galaxies in our observed images have spectroscopic redshifts. We further include six SMGs from the Chapman et al. (2005) HDF-North study. Therefore, our final SMG sample studied here contains 14 sources spanning $0.5 \leq z \leq 3$.

Besides these two populations, star-forming galaxies at $z > 1.4$ can also be identified using the *BzK* technique (Daddi et al. 2004). This technique is designed to cull galaxies from *K*-selected samples. Star-forming *BzK* galaxies (*sBzK*) tend to be more massive and have higher reddening than UV-selected galaxies. With this method, 70 *sBzK* galaxies at $z > 1.4$ and $K_{AB} \leq 23$ are selected using the criteria $(z - K) - (B - z) > -0.2$. We further use this sample to compare properties of star-forming galaxy populations at high redshifts. The *sBzK* selection criteria can identify $\sim 90\%$ of our BM/BX galaxies. The large overlap is not surprising since both our UV-selected and *sBzK* samples consist of mostly massive galaxies (due to the *K* magnitude limit). Table 2.1 lists samples of star-forming galaxies used in this paper.

2.6 Results

2.6.1 Size Evolution

In Figure 2.3, we show the size distributions for UV-bright galaxies between $10 < \log(M_*/M_\odot) < 11$. The blue histogram shows the measured half-light radii of *GALEX*/LBGs at $z \sim 1$ while the distribution of sizes measured for BM/BX galaxies ($z \sim 2$) is shown as a green histogram. It can be seen from this plot that UV-bright galaxies at $z \sim 2$ are smaller compared to similar galaxies at $z \sim 1$. Specifically, the median half-light radius of BM/BX galaxies in this mass range is 2.68 ± 0.19 kpc significantly smaller than the median effective radii of *GALEX*/LBGs (4.42 ± 0.52 kpc). This means that sizes of UV-bright galaxies evolve by a median factor of 0.60 ± 0.08 between $z \sim 2$ and $z \sim 1$. It is harder to measure the evolution for $z \sim 3$ to $z \sim 2$, as we have four LBGs within mass range of $10 < \log(M_*/M_\odot) < 11$ at $z \sim 3$ in our sample. The median half-light radius of these four massive galaxies is 2.22 ± 0.61 kpc, 0.82 ± 0.23 smaller than $z \sim 2$ BM/BX galaxies. We perform a power-law fit on the size evolution and find $r_e \propto (1 + z)^{-1.11 \pm 0.13}$ over the range $0.6 \lesssim z \lesssim 3.5$.

The size-redshift relation for star-forming galaxies with spectroscopic redshifts in the GOODS-North field is shown in Figure 2.4. Galaxies are split into the four different stellar mass bins shown in the figure. In each panel, the gray small symbols are normal star-forming galaxies with spectroscopic redshifts selected to have specific star formation rates log sSFR > -10. Color symbols represent our samples of UV-bright galaxies and SMGs. LBGs ($2.7 < z < 3.5$) are shown as dark-green triangles, and BM/BX galaxies ($1.4 < z < 2.7$) are plotted as green squares. *GALEX*/LBGs at relatively lower redshifts ($0.6 < z < 1.4$) are plotted in different panels as blue stars. The black symbols at $z \sim 0$ are star-forming galaxies from Guo et al. (2009) from SDSS.

As Figure 2.4 shows, sizes of UV-bright galaxies at a fixed stellar mass increase toward lower redshifts. There is also a trend that the size evolution maybe stronger for the most massive galaxies. For example, UV-bright galaxies with stellar masses $9 < \log(M_*/M_\odot) < 10$ evolve by a median factor of approximately 1.15 ± 0.25 from $z \sim 2$ to $z \sim 0.8$. However, galaxies with masses $10 < \log(M_*/M_\odot) < 10.5$ grow by a median factor of approximately 1.82 ± 0.25. At higher stellar mass bin ($10.5 < \log(M_*/M_\odot) < 11$), this evolution is even stronger: a factor of 2.05 ± 1.26 over the same redshift range. However, selection effects may influence this trend (especially in the low-mass bin) and more complete samples are needed.

SMGs are also shown as pink diamonds in Figure 2.4; they are discussed further in Section 2.6.4. Galaxies which have X-ray luminosities $> 10^{42}$ ergs s^{-1} (i.e., potential AGN hosts) are marked with open circles. These galaxies have sizes similar to the others. Since AGN is point-like, one would expect galaxies with AGN emission to have smaller half-light radii. Their "normal" rest-frame optical sizes are thus perhaps not strongly influenced. Nonetheless, due to possible effects on the size and mass estimates, X-ray-detected galaxies should be considered low-confidence points.
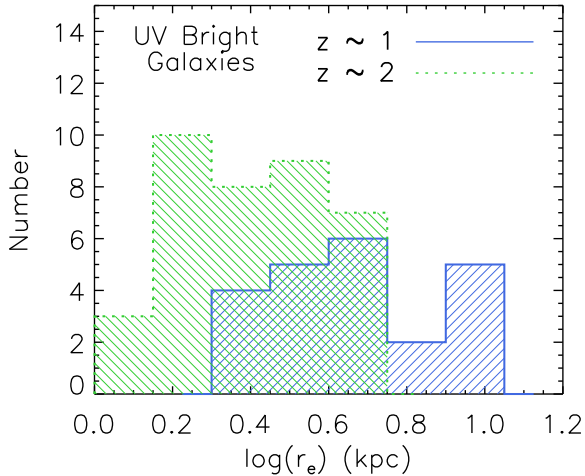
Figure 2.3 – Size distribution of UV-bright galaxies with stellar mass $10 < \log(M_*/M_\odot) < 11$ at $z \sim 1$ (blue histogram) and $z \sim 2$ (green histogram). The half-light radii of UV-bright galaxies (*GALEX*(LBGs)) at $z \sim 1$ are larger than BM/BX galaxies at $z \sim 2$.

2.6.2   Stellar Mass-Size Relation

We now investigate how mass-size distribution of the UV-bright galaxies compares to other galaxy populations. We further check if the relation between stellar mass and size of these galaxies exists to high redshift.

The stellar mass-size distributions of our samples are shown in Figure 2.5. We have divided our sample into three redshift bins: $0.5 < z < 1.5$, $1.5 < z < 2.5$, and $2.5 < z < 3.5$. UV-bright galaxies are color coded in the same way as in Figure 2.4. Solid and dotted lines in each panel show the mass-size relation from Shen et al. (2003) for star-forming galaxies and early-type galaxies at $z \sim 0$, respectively. The gray symbols are the K-selected sample of galaxies in CDF-South with stellar masses $> 10^{9.8} M_\odot$ (Franx et al. 2008). Comparing our results with the galaxies from CDF-S allows us to see where our galaxies lie relative to a purely mass-selected sample. Brown solid lines in the middle of each panel show the median effective radii in narrow mass bins for all galaxies in CDF-S. As can be seen, at $z \sim 1$ and $z \sim 2$, UV-bright galaxies have larger effective radii compared to all galaxies at a given stellar mass. For galaxies between 10^{10} and $10^{11} M_\odot$, the median sizes differ by a factor of 1.89 ± 0.23 and 1.12 ± 0.09 at $z \sim 1$ and 2, respectively. As the spectroscopic sample contains only four UV-bright galaxies in this mass range at $z \sim 3$, the difference with CDF-S is not well constrained at this redshift (1.27 ± 0.36).

We further investigate how the size-mass distribution of GOODS-N UV-bright galaxies compares to that of UV-bright galaxies in CDF-S. This would help to verify if the
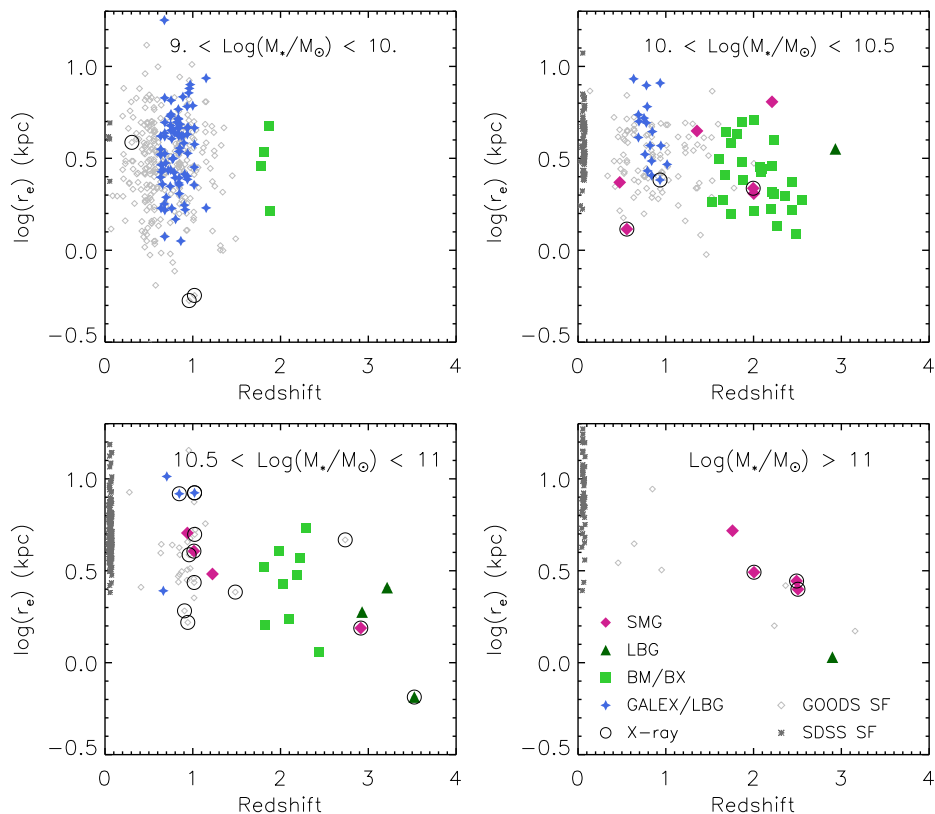
Figure 2.4 – Evolution of sizes of galaxies as a function of redshift. Each panel shows the size evolution for a narrow stellar mass bin. The gray symbols are star-forming galaxies with spectroscopic redshifts in GOODS-N field. Blue stars are GALEX/LBGs (*z* ∼ 1) while the green squares and green triangles represent BM/BX galaxies (*z* ∼ 2) and LBGs (*z* ∼ 3), respectively. SMGs are also shown as pink diamonds. Galaxies with X-ray luminosities more than 10^{42} ergs s^{-1} are marked by open circles. Black symbols at *z* ∼ 0 are SDSS star-forming galaxies from Guo et al. (2009). As this plot illustrates, the half light radii of UV-bright galaxies evolve with redshift and this evolution is faster for high-mass galaxies.

previously reported size-mass relation for a large photometric sample (Franx et al. 2008) is consistent with our spectroscopic sample. We define analogs of the $z \sim 1, 2$, and 3 LBGs in CDF-S by their optical colors and magnitudes. Specifically, we selected the analogs of the $z \sim 1$ *GALEX*/LBGs by requiring $(B - V) < 0.6$ and $R \leq 23.8$. This selection is based on the locus of the GOODS-N *GALEX*/LBGs in this color-magnitude plane. The analogs of BM/BX galaxies in CDF-S are similarly selected with $R < 25.1$ and $(B - V) < 0.8$ and $z_{phot} = 1.5 - 2.5$. We note that the R-band magnitude in both surveys is estimated by the average values of V- and I-band magnitudes. We verified that the spectroscopic samples are effectively selected by these criteria. In order to identify analogs of UV-bright objects in CDF-S at $z \sim 2.5 - 3.5$, we find the location of LBGs in GOODS-N on the color-color $(B - V)$ versus $(V - I)$ diagram and apply the following criteria to the CDF-S galaxies: (1) $0.5 < (B - V) < 1.2$ for $(V - I) < 0.35$; (2) $(B - V) > 3 \times (V - I) + 0.5$ and $(B - V) < 1.2$ for $0.35 < (V - I) < 0.5$. We note that these selection criteria do not impose a "U-drop out" criteria, but do select galaxies with similar brightness and UV slope as the usual LBG methods.

The comparison of size-mass distributions for UV-bright galaxies from both fields is shown in Figure 2.6. In each panel, the color symbols are the median log effective radii of UV-bright galaxies in narrow mass bins, with the blue and green symbols representing UV-bright galaxies in GOODS-N and the brown symbols are the ones in CDF-S. The error bars show the 1σ dispersion. UV-bright samples from both fields follow consistent size-mass relation, further confirming that UV-bright galaxies are on average larger than overall galaxies at a fixed stellar mass. We note that at high redshift ($z \sim 2.5 - 3.5$) the comparison is weak because of the limited number LBGs in GOODS-N.

The UV-bright galaxies show a weak stellar mass-size relation at $z = 1$ and $z = 2$ in Figure 2.5. To quantify this relation, we fitted a power-law function of the form $r_e \propto M^\alpha$ to the individual UV-bright galaxies in each redshift bin. The fitting results are plotted as color dashed-dotted lines in Figure 2.6. At $z \sim 1$, the size of *GALEX*/LBGs in GOODS-N scales with stellar mass as $r_e \propto M^{0.19 \pm 0.05}$ and the BM/BX galaxies at $z \sim 2$ have $r_e \propto M^{0.30 \pm 0.06}$. The uncertainties were estimated using bootstrap resampling. The results are comparable to the relation for late-type galaxies at $z \sim 0$ from Shen et al. (2003). They found $r_e \propto M^{0.15}$ for low-mass ($\log(M) < 10.6$) late-type galaxies and steeper relation for high-mass late-type galaxies ($r_e \propto M^{0.4}$). In the highest redshift bin ($z \sim 3$), we use UV-bright galaxies from CDF-S to find the best fit ($\alpha = 0.32 \pm 0.06$). Table 2.2 lists the best-fit power-law parameter to the mass-size relation of UV-bright galaxies. The slopes of the mass-size relation at different redshift bins are consistent and there is no significant evolution. Our results confirm the persistence of the size-mass relation for star-forming galaxies up to high redshift.

It is worth checking whether or not other star-forming populations at high redshift have the same size-mass relation. Therefore, we compare star-forming *BzK* galaxies (*sBzK*) with BM/BX galaxies. The size distribution as a function of stellar mass is shown in Figure 2.7 with the *sBzK* galaxies plotted as gray filled circles. The medians of log effective radii of *sBzK* galaxies are overplotted as red squares. BM/BX galaxies and SMGs are marked with the green and pink circles, respectively, and the green dashed-dotted line shows the mass-size relation for BM/BX galaxies. As one can see, the mass-size relation
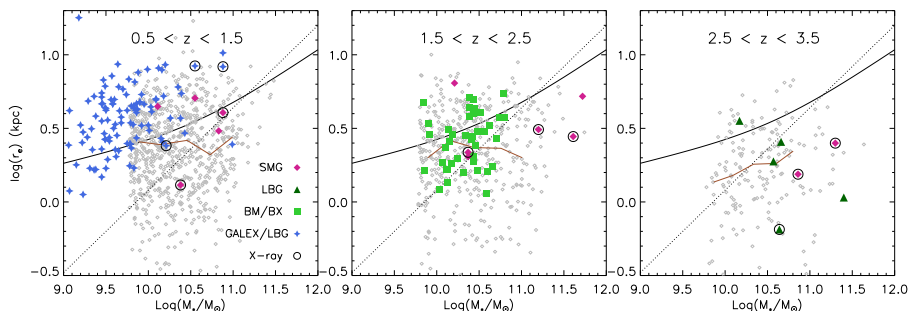
Figure 2.5 – Stellar mass-size distribution for UV-bright galaxies in different redshift bins compared to the galaxies from CDF-South (Franx et al. 2008) (gray dots). The color symbols represented here are the same as Figure 2.4. The solid and dotted black lines are the size-mass relations for star-forming and quiescent galaxies, respectively, at $z \sim 0$ from Shen et al. (2003). The solid brown lines show the median sizes in narrow mass bins for all galaxies from CDF-S. The UV bright galaxies are in general larger than normal field galaxies at the same mass.
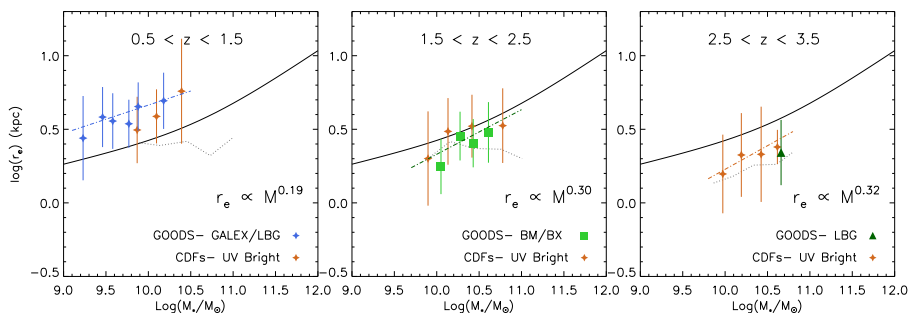
Figure 2.6 – Comparison of the stellar mass-size relation for the UV-bright galaxies from GOODS-N field and CDF-South in three redshift bins. The black solid lines are the size-mass relation for star-forming galaxies at $z \sim 0$ from Shen et al. (2003). The color symbols are median of UV-bright galaxies in narrow mass bins and the error bars show 1σ (68%) dispersion. The dashed-dotted lines are the best power-law fits using $r_e \propto M^\alpha$ to the individual UV-bright galaxies. The dotted lines are the median sizes in narrow mass bins for all galaxies from CDF-S (Same as Figure 2.5). This plot shows that the derived half-light radii of UV-bright galaxies from both fields are in place and agreement with each other up to $z \sim 3$.

Table 2.2 – Best Fits Power-law Parameter for the Stellar
Mass-Size Relation

Sample	Redshift	α
GALEX/LBG	$0.6 < z < 1.4$	0.19 ± 0.05
BM/BX	$1.4 < z < 2.7$	0.30 ± 0.06
CDFs-UV Bright	$2.5 < z < 3.5$	0.32 ± 0.06
sBzK	$1.4 < z < 3.2$	0.31 ± 0.09

Notes. Power-law parameter α is defined as $r_e \propto M^\alpha$.
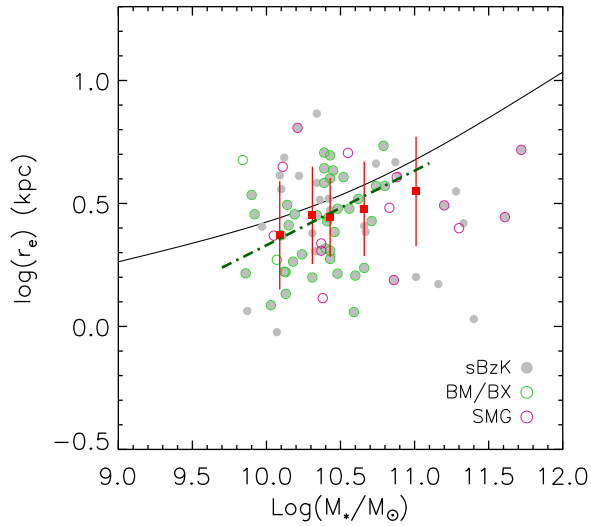
Figure 2.7 – Stellar mass-size relation for star-forming *sBzK* galaxies (gray circles). The BM/BX galaxies and SMGs are marked with green and pink circles, respectively. The red squares are the median for the mass-size relation of *sBzK* sample with 1σ dispersion. The green dashed-dotted line is the best fit to the BM/BX galaxies. The *sBzK* galaxies have a similar size-mass relation to the BM/BX galaxies. The solid line shows the mass-size relation for star-forming galaxies at $z \sim 0$ from Shen et al. (2003).

Figure 2.8 – Left panel: the correlation between color ($V_{606} - z_{850}$) and surface density for galaxies in the redshift range of $0.5 < z < 1.5$ and stellar masses $10^{10} < M/M_\odot < 10^{11}$ in GOODS-N field. The blue stars are *GALEX*(LBGs) from GOODS-N and the brown circles are 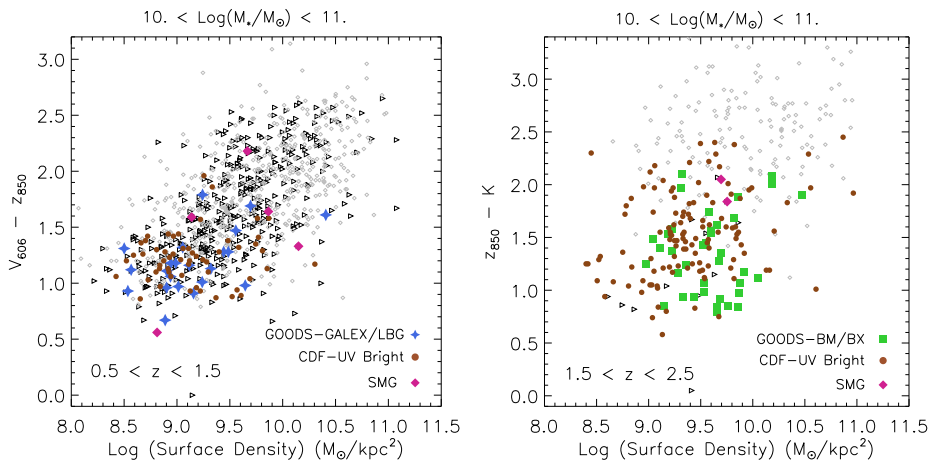from CDF-S. The gray symbols are all galaxies from CDFS and the black triangles are galaxies from GOODS-N. Right panel: the color ($z_{850} - K$) vs. surface density for galaxies at $1.5 < z < 2.5$, as the green squares are the BM/BX galaxies from GOODS-N and the brown circles are pseudo-BM/BX from CDF-S. The plots indicate that blue galaxies having lower surface density.

for *sBzK* galaxies is comparable to the one for BM/BX galaxies. The average offset of median half-light radii of *sBzK* galaxies to the BM/BX mass-size relation is 0.037 dex. The effective radii of *sBzK* galaxies scale with stellar mass as $r_e \propto M^{0.31\pm0.09}$ close to the size-mass relation for UV-bright galaxies. This similarity could be due to the significant overlap between the UV-selected galaxies and *sBzK* galaxies (e.g., Reddy et al. 2005). We note that stellar masses can have significant uncertainties depending on the methods used to calculate them. We verify that by using the stellar mass estimates from Reddy et al. (2006) for UV-bright galaxies, the size-mass distribution of these galaxies covers the same region in the size-mass plane (see, e.g., the middle panel of Figure 2.5). Hence, this shows that our results are robust against using different estimates of stellar masses.

2.6.3 Color-Surface Density

One of the surprising results of Franx et al. (2008) was the tight correlation between stellar mass surface density (M_*/r_e^2) and color of galaxies to $z \sim 3$. They showed that bluer galaxies have lower surface densities than red quiescent ones. They indicated that the color of galaxies correlates more fundamentally with the stellar mass surface density than the mass.

We show the tight relation between color and stellar mass surface density for both star-forming and quiescent galaxies with $M_\odot \sim 10^{10} - 10^{11}$ in Figure 2.8. In the left panel, the
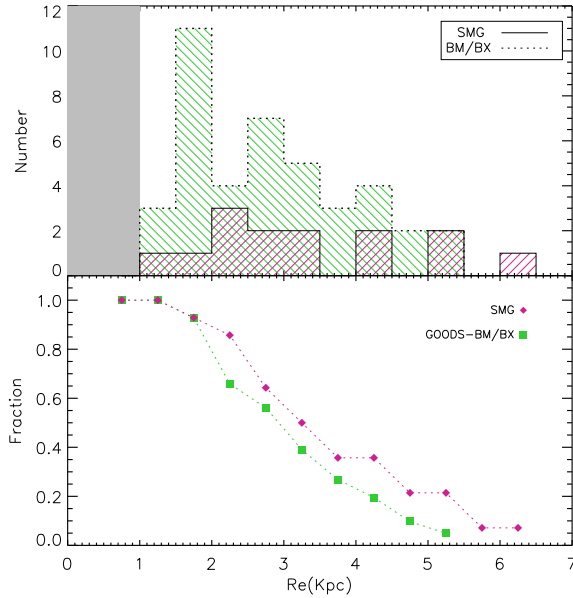
Figure 2.9 – Top panel: histograms show the distribution of sizes of SMGs (solid line) and BM/BX galaxies (dotted lines). The gray region indicates apparent effective radii below 0.1"($\sim$ 1 kpc at $z \sim 2$) which size measurements have large uncertainties. Lower panel: cumulative distribution function for SMGs (pink diamonds) and BM/BX galaxies (green squares). As the plot shows, the distributions of half-light radii of these two populations are comparable with SMGs being slightly larger.

observed color ($V_{606} - z_{850}$) is plotted versus the stellar mass surface density for galaxies at redshift $\sim$ 1. The black and gray symbols are galaxies from GOODS-N and CDF-S fields, respectively. The blue stars and brown circles indicate the *GALEX* (LBGs) and their analogs from CDF-S, respectively. In the right panel, the relation between observed (z_{850}-K) and surface density for galaxies at higher redshift $\sim$ 2 is illustrated , with BM/BX galaxies in GOODS-N shown by green squares and their analogs in CDF-S as brown circles. As can be seen in this figure, the blue star-forming galaxies have lower surface density than red galaxies at both $z \sim 1$ and $z \sim 2$, though the correlation between color and surface density is more tight at $z \sim 1$ than $z \sim 2$. In general, using sample of galaxies with spectroscopic redshifts confirms that the color of galaxies tightly correlates with surface density and this relation holds out to high redshifts.

2.6.4 Sizes of Submillimeter Galaxies

Since GOODS-N includes 14 SMGs with redshifts, we compare their masses and sizes to the UV-selected galaxies at $z \sim 2$. As Figure 2.4 illustrates, the optical rest-frame sizes of the SMGs (pink diamonds) and UV-selected galaxies of similar mass are comparable. The median half-light radius of all SMGs is 2.90 ± 0.45 kpc which is in good agreement with the median optical rest-frame sizes of the BM/BX galaxies over the whole mass range (2.68 ± 0.25 kpc). The median effective radius of SMGs with stellar masses of 10^{10}-10^{11} is 2.65 ± 0.56 which is similar to the BM/BX of at the same mass range (2.68 ± 0.19). The errors are computed using bootstrap resampling.

We further compare the size distributions of SMGs and BM/BX galaxies in Figure 2.9. In the top panel, the histograms show the size distribution of BM/BX galaxies and SMGs. In the bottom panel, the normalized cumulative distribution functions are shown for both samples. As this plot shows, the size distributions of SMGs are comparable with $z \sim 2$ UV-bright galaxies and the SMGs follow the same size distribution as BM/BX galaxies in the optical rest-frame with SMGs being slightly larger. According to a K-S test, the probability that two distributions being the same is 72%, suggesting no significant difference between the rest-frame optical sizes of the SMGs and UV-bright galaxies.

2.7 Discussion

2.7.1 The growth of star-forming galaxies

We study the size evolution of galaxies with spectroscopic redshifts between $z \sim 0.5$ and 3.5. Our results are summarized in Figure 2.10. As this plot illustrates, at each epoch, the median sizes of UV-bright galaxies (color squares) with stellar masses $10 < \log(M_*/M_\odot) < 11$ are larger (by a median factor of 0.45 ± 0.09) than quiescent galaxies in a similar mass range selected from CDF-S (red circles). The red triangle is the median sizes of quiescent galaxies studied in (van Dokkum et al. 2008, VD08 hearafter) with a median stellar mass of $1.7 \times 10^{11} M_\odot$ and median redshift of 2.3. Table 2.3 lists the median half-light radii for UV-bright and quiescent galaxies seen in Figure 2.10. The growth of UV-bright galaxies with time is also illustrated in this figure. The dashed line shows that UV-bright galaxies scaled up their sizes toward lower redshifts as $(1 + z)^{-1.11 \pm 0.13}$.

Previous studies (Franx et al. 2008, Kauffmann et al. 2003) have reported that there is a correlation between color and stellar mass surface density of galaxies at both low and high redshifts. However, the results based on photometric redshifts can be uncertain especially for star-forming galaxies. By means of our large sample of galaxies with secure redshifts, we have confirmed that the tight correlation between color and stellar mass surface density of galaxies that holds out to high redshifts; as the stellar mass densities of blue star-forming galaxies are smaller than those of red quiescent ones. This verifies that the galaxies with higher specific star formation rate are larger than the ones with lower specific star formation rates.

We have also explored the stellar mass-size distribution for galaxies in our sample. We have confirmed that there is a relation between stellar mass and size for UV-bright galaxies
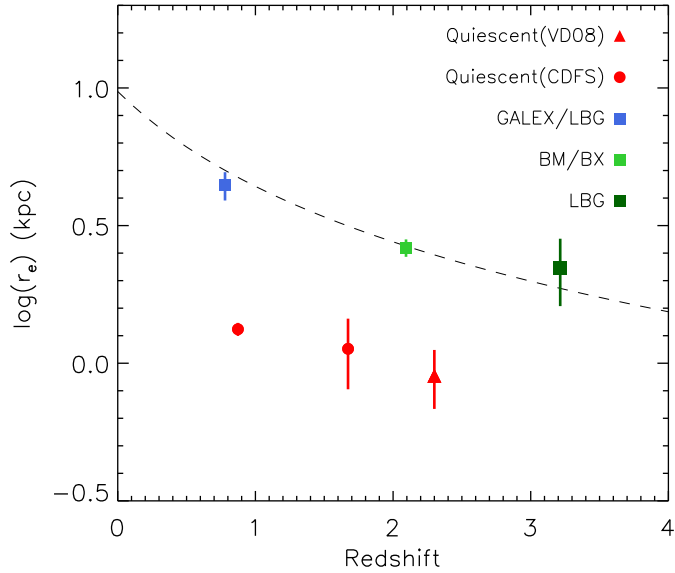
Figure 2.10 – Median sizes of UV-bright galaxies (squares) as a function of redshifts for galaxies with stellar masses $10^{10} < M/M_{\odot} < 10^{11}$ in GOODS-N field. The red filled circles are quiescent galaxies from CDF-S study with similar mass range and the red triangle is the quiescent sample from van Dokkum et al. (2008) with median stellar masses of $1.7 \times 10^{11} M_{\odot}$. The dashed line shows the best-fitting size evolution to the UV-bright galaxies ($r_e \propto (1 + z)^{-1.11\pm0.13}$). The plot indicates that the UV-selected galaxies are larger than quiescent galaxies and their sizes evolve with redshift.

at $0.5 < z < 3.5$. The relations are consistent for both spectroscopic and photometric redshift samples. Our results verify that there is no significant evolution of the slope of the size-mass relation to redshift ~ 3.5. The evolution of the relation from $z = 1$ to $z = 0$ is not well established, as it is not straight forward to select LBGs at $z \sim 0$. Some authors find evolution (e.g., Franx et al. 2008, Williams et al. 2010) in the stellar mass-size relation; however, Barden et al. (2005) have reported that the stellar mass-size relation for disk galaxies remains constant from $z \sim 1$ to the present. Selection effects likely play a role. Comparing to the theoretical work, the size evolution predicted by Somerville et al. (2008) is somewhat stronger than the evolution we measured here.

Star-forming galaxies at high redshifts can be identified by means of different methods of sample selection and can be assigned as different populations of galaxies (e.g., submillimeter or *sBzK*) and therefore studied separately. However, many of these galaxy populations may overlap, hence it is worth checking out if they have comparable properties. We, therefore, compare sizes of UV-bright galaxies to other types of star-forming galaxy populations at high redshift, i.e., *sBzK* galaxies and SMGs. We show that these two populations have comparable sizes to the UV-bright galaxies. This suggests that, in general, star-forming galaxies have larger sizes than quiescent ones without regard to their type. However, sample selection might alter the results. We return to this possibility later, in Section 2.7.3.

2.7.2 Comparison to previous work

The strong growth of both star-forming and quiescent galaxies has been shown by several authors (Trujillo et al. 2006b, Franx et al. 2008, Williams et al. 2010, Toft et al. 2007). The size growth of star-forming galaxies studied here going as $(1+z)^\alpha$, where $\alpha = -1.11 \pm 0.13$, agrees well compared to previous studies where the size evolves with $\alpha \sim -1$. For example, Bouwens et al. (2006) found $\alpha = -1.1 \pm 0.3$ for a sample of luminosity-selected dropout galaxies between $z \sim 6$ and $z \sim 2.5$, while Dahlen et al. (2007) found $\alpha = -1.10 \pm 0.07$ for luminosity-selected disk galaxies over the range $z \sim 1.1$-2.2. Williams et al. (2010) also found a similar slope for star-forming galaxies in UDS at $z \sim 0.5$-2.

The similarity between sizes of UV-bright galaxies and star-forming *BzK* galaxies is also shown in our study. The two populations are also compared by Overzier et al. (2010). They showed that rest-frame optical sizes of *sBzK* galaxies are somewhat larger than UV-selected galaxies. Since *BzK* galaxies are K-selected and thus tend to represent massive galaxies, it is not surprising that they appear larger. Hence, the sizes must be corrected for differing stellar masses for an accurate comparison to be made.

Our results also show that the SMGs have a median half-light radius of 2.90 ± 0.45 kpc comparable to the rest-frame optical sizes of the BM/BX galaxies. The result is in agreement with a recent study by Swinbank et al. (2010) where they use deep *HST I* and *H*-band imaging and show that the rest-frame optical sizes of the SMGs and UV-bright galaxies in GOODS-N are comparable. The typical half-light radius of the SMGs in the *H*-band (rest-frame optical) measured by Swinbank et al. (2010) is 2.8 ± 0.4 which is consistent with our measurements (see also Targett et al. 2010 for more comparison.). Almaini et al. (2005) also compared sizes of SMGs with LBGs at rest-frame optical and

Table 2.3 – Median Sizes of Different Samples

Sample	Redshift	Median Size (kpc)	Median($\log(M_*/M_\odot)$)
GALEX/LBG	$0.6 < z < 1.4$	4.42 ± 0.52	10.2 ± 0.3
BM/BX	$1.4 < z < 2.7$	2.68 ± 0.19	10.4 ± 0.2
LBG	$2.7 < z < 3.5$	2.22 ± 0.61	10.6 ± 0.2
CDFS	$0.5 < z < 1.5$	2.33 ± 0.1	10.4 ± 0.3
CDFS	$1.5 < z < 2.5$	2.40 ± 0.13	10.4 ± 0.3
CDFS	$2.5 < z < 3.5$	1.73 ± 0.18	10.4 ± 0.3
Quiescent(CDFS)	$0.5 < z < 1.5$	1.32 ± 0.07	10.5 ± 0.3
Quiescent(CDFS)	$1.5 < z < 2$	1.12 ± 0.32	10.7 ± 0.2
Quiescent(VD08)	$2 < z < 2.5$	0.9 ± 0.21	11.23
SMG	$0.5 < z < 3.$	2.90 ± 0.45	10.8 ± 0.5

Notes. The median sizes are for galaxies with stellar masses between 10^{10} and $10^{11} M_\odot$. This mass limit is not applied to the quiescent (van Dokkum et al. 2008, , VD08) and SMG galaxies. The CDFS samples contain both star-forming and quiescent galaxies at the same mass range in CDF-S.

found no clear difference between sizes of the SMGs and LBGs. It is worth noting that SMGs have larger median stellar masses compared to BM/BX galaxies (also mentioned in Swinbank et al. 2010). This suggests higher stellar mass densities for SMGs compared to UV bright galaxies. However, the similarity in sizes between these two galaxy populations at high z does not by itself allow conclusive connections to be drawn between the two populations. The SMGs that are faint or lacking emission lines could be missing from our spectroscopic sample and they may have dramatically different mass or size properties. Therefore, selection effect could bias these results. Spectroscopic observation in near-IR might help to solve this problem; e.g., Kriek et al. (2009a) find a median size of 2.8 kpc for a small sample of near-IR spectroscopically confirmed star-forming galaxies at $z \sim 2.3$. Indeed, our measured size evolution is consistent with their spectroscopic sample; however, near-IR spectroscopy over a large redshift range is needed to definitively quantify the size evolution.

2.7.3 Caveats

With this large spectroscopic sample of high-redshift galaxies, we have removed an important source of uncertainty in the stellar mass-size relation and verified the results from larger samples based on photometric redshifts. However, the spectroscopic catalog we used in this study consists of many different spectroscopic surveys which made it inhomogeneous. Galaxies in this catalog are mostly relatively unobscured star-forming galaxies with emission lines, comparing these to quiescent galaxies can still be a problem because spectroscopy of high-redshift red galaxies is difficult. Therefore, using a larger and homogeneous sample of high-redshift galaxies with secure redshift will allow greatly

improved constraints on their evolution. New ground and space-based IR multi-object spectrographs (WFC3 grism, MMIRS, MOSFIRE) will allow investigations of more complete samples of galaxies and study the correlation between galaxy properties at higher redshifts. Dust-obscured starbursts are also likely to be missed in our UV-bright sample, hence NIR spectroscopy will also permit studies of this important population.

2.8   Summary

We have performed the first size evolution study of UV-bright galaxies with secure redshifts in the GOODS-North field. We derive half-light radii of galaxies at a wide range of redshifts (up to $z \sim 3.5$). Using sample of galaxies with secure redshifts, we have quantified the size evolution of galaxies without the potential uncertainty of photometric redshifts and confirm the previous studies that galaxies of similar mass were generally smaller at past and their sizes evolve with redshift. Specifically, we find that:

- UV-bright galaxies evolve strongly as $(1 + z)^{-1.11 \pm 0.13}$ confirming previous studies based on photometric redshifts (e.g., Trujillo et al. 2006b, 2007, Franx et al. 2008, Williams et al. 2010).

- UV-bright galaxies are significantly larger than quiescent galaxies. At the same mass, the median difference is 0.45 ± 0.09 dex.

- The LBG, BM/BX, and *GALEX*/LBG samples show smooth evolution with redshift, indicating that these techniques indeed select similar UV-bright galaxies at different redshifts.

- The SMGs have half-light radii similar to UV-bright galaxies of the same mass.

2.9   Acknowledgments

Bibliography

Adelberger, K. L., Steidel, C. C., Shapley, A. E., Hunt, M. P., Erb, D. K., Reddy, N. A., & Pettini, M. 2004, ApJ, 607, 226

Almaini, O., Dunlop, J. S., Conselice, C. J., Targett, T. A., & Mclure, R. J. 2005, arXiv:astro-ph/0511009v1

Barden, M., et al. 2005, ApJ, 635, 959

Barger, A. J., Cowie, L. L., & Wang, W. 2008, ApJ, 689, 687

Bell, E. F., et al. 2006, ApJ, 640, 241

Bezanson, R., van Dokkum, P. G., Tal, T., Marchesini, D., Kriek, M., Franx, M., & Coppi, P. 2009, ApJ, 697, 1290

Blain, A. W., Chapman, S. C., Smail, I., & Ivison, R. 2004, ApJ, 611, 725

Bouwens, R. J., Illingworth, G. D., Blakeslee, J. P., & Franx, M. 2006, ApJ, 653, 53

Bouwens, R. J., Illingworth, G. D., Franx, M., & Ford, H. 2008, ApJ, 686, 230

Bruzual, G., & Charlot, S. 2003, MNRAS, 344, 1000

Capak, P., et al. 2004, AJ, 127, 180

Chapman, S. C., Blain, A. W., Ivison, R. J., & Smail, I. R. 2003, Nature, 422, 695

Chapman, S. C., Blain, A. W., Smail, I., & Ivison, R. J. 2005, ApJ, 622, 772

Cimatti, A., et al. 2008, A&A, 482, 21

Cohen, J. G. 2001, AJ, 121, 2895

Cohen, J. G., Hogg, D. W., Blandford, R., Cowie, L. L., Hu, E., Songaila, A., Shopbell, P., & Richberg, K. 2000, ApJ, 538, 29

Cowie, L. L., Barger, A. J., Hu, E. M., Capak, P., & Songaila, A. 2004, AJ, 127, 3137

Daddi, E., Cimatti, A., Renzini, A., Fontana, A., Mignoli, M., Pozzetti, L., Tozzi, P., & Zamorani, G. 2004, ApJ, 617, 746

Daddi, E., et al. 2005, ApJ, 626, 680

Dahlen, T., Mobasher, B., Dickinson, M., Ferguson, H. C., Giavalisco, M., Kretchmer, C., & Ravindranath, S. 2007, ApJ, 654, 172

Damjanov, I., et al. 2009, ApJ, 695, 101

Dekel, A., Sari, R., & Ceverino, D. 2009, ApJ, 703, 785

Elmegreen, B. G., Bournaud, F., & Elmegreen, D. M. 2008, ApJ, 688, 67

Franx, M., van Dokkum, P. G., Schreiber, N. M. F., Wuyts, S., Labbé, I., & Toft, S. 2008, ApJ, 688, 770

Giavalisco, M., et al. 2004, ApJ, 600, L93

Guo, Y., et al. 2009, MNRAS, 398, 1129

Hopkins, P. F., Bundy, K., Murray, N., Quataert, E., Lauer, T. R., & Ma, C. 2009, MNRAS, 398, 898

Hughes, D. H., et al. 1998, Nature, 394, 241

Kajisawa, M., et al. 2006, PASJ, 58, 951

Kauffmann, G., et al. 2003, MNRAS, 341, 54

Khochfar, S., & Silk, J. 2006, ApJ, 648, L21

—. 2009, MNRAS, 397, 506

Kriek, M., van Dokkum, P. G., Franx, M., Illingworth, G. D., & Magee, D. K. 2009a, ApJ, 705, L71

Kriek, M., van Dokkum, P. G., Labbé, I., Franx, M., Illingworth, G. D., Marchesini, D., & Quadri, R. F. 2009b, ApJ, 700, 221

Kroupa, P. 2001, MNRAS, 322, 231

Longhetti, M., et al. 2007, MNRAS, 374, 614

Naab, T., Johansson, P. H., & Ostriker, J. P. 2009, ApJ, 699, L178

Ouchi, M., Tokoku, C., Shimasaku, K., & Ichikawa, T. 2007, in Astronomical Society of the Pacific Conference Series, Vol. 379, Cosmic Frontiers, ed. N. Metcalfe & T. Shanks, 47–+

Overzier, R. A., Heckman, T. M., Schiminovich, D., Basu-Zych, A., Gonçalves, T., Martin, D. C., & Rich, R. M. 2010, ApJ, 710, 979

Peng, C. Y., Ho, L. C., Impey, C. D., & Rix, H. 2002, AJ, 124, 266

Pope, A., et al. 2006, MNRAS, 370, 1185

Reddy, N. A., Erb, D. K., Steidel, C. C., Shapley, A. E., Adelberger, K. L., & Pettini, M. 2005, ApJ, 633, 748

Reddy, N. A., Steidel, C. C., Erb, D. K., Shapley, A. E., & Pettini, M. 2006, ApJ, 653, 1004

Salpeter, E. E. 1955, ApJ, 121, 161

Shen, S., Mo, H. J., White, S. D. M., Blanton, M. R., Kauffmann, G., Voges, W., Brinkmann, J., & Csabai, I. 2003, MNRAS, 343, 978

Smail, I., Ivison, R. J., Blain, A. W., & Kneib, J. 2002, MNRAS, 331, 495

Somerville, R. S., et al. 2008, ApJ, 672, 776

Steidel, C. C., Adelberger, K. L., Shapley, A. E., Pettini, M., Dickinson, M., & Giavalisco, M. 2003, ApJ, 592, 728

Steidel, C. C., Shapley, A. E., Pettini, M., Adelberger, K. L., Erb, D. K., Reddy, N. A., & Hunt, M. P. 2004, ApJ, 604, 534

Swinbank, A. M., Chapman, S. C., Smail, I., Lindner, C., Borys, C., Blain, A. W., Ivison, R. J., & Lewis, G. F. 2006, MNRAS, 371, 465

Swinbank, A. M., et al. 2010, MNRAS, 405, 234

Tacconi, L. J., et al. 2008, ApJ, 680, 246

Targett, T. A., Dunlop, J. S., McLure, R. J., et al. 2010, arXiv:1005.5176

Toft, S., Franx, M., van Dokkum, P., Förster Schreiber, N. M., Labbe, I., Wuyts, S., & Marchesini, D. 2009, ApJ, 705, 255

Toft, S., et al. 2007, ApJ, 671, 285

Trujillo, I., Conselice, C. J., Bundy, K., Cooper, M. C., Eisenhardt, P., & Ellis, R. S. 2007, MNRAS, 382, 109

Trujillo, I., et al. 2006a, MNRAS, 373, L36

—. 2006b, ApJ, 650, 18

van Dokkum, P. G., et al. 2008a, ApJ, 677, L5

—. 2008b, ApJ, 677, L5

—. 2010, ApJ, 709, 1018

Williams, R. J., Quadri, R. F., Franx, M., van Dokkum, P., Toft, S., Kriek, M., & Labbé, I. 2010, ApJ, 713, 738

Wirth, G. D., et al. 2004, AJ, 127, 3121

Zirm, A. W., et al. 2007, ApJ, 656, 66

The Evolution of Mass-Size Relation for Lyman Break Galaxies From $z = 1$ to $z = 7$

Moein Mosleh, Rik J. Williams, Marijn Franx, Valentino Gonzalez, Rychard J. Bouwens, Pascal Oesch, Ivo Labbe, Garth D. Illingworth, and Michele Trenti

Abstract

For the first time, we study the evolution of the stellar mass-size relation for star-forming galaxies from $z \sim 4$ to $z \sim 7$ from Hubble-WFC3/IR camera observations of the HUDF and Early Release Science field. The sizes are measured by determining the best-fit model to galaxy images in the rest-frame 2100 Å with the stellar masses estimated from spectral energy distribution fitting to rest-frame optical (from *Spitzer*/IRAC) and UV fluxes. We show that the stellar mass-size relation of Lyman break galaxies (LBGs) persists, at least to $z \sim 5$, and the median size of LBGs at a given stellar mass increases toward lower redshifts. For galaxies with stellar masses of $9.5 < \log(M_*/M_\odot) < 10.4$ sizes evolve as $(1 + z)^{-1.20\pm0.11}$. This evolution is very similar for galaxies with lower stellar masses of $8.6 < \log(M_*/M_\odot) < 9.5$ which is $r_e \propto (1 + z)^{-1.18\pm0.10}$, in agreement with simple theoretical galaxy formation models at high z. Our results are consistent with previous measurements of the LBGs mass-size relation at lower redshifts ($z \sim 1 - 3$).

3.1   Introduction

The size of a galaxy is a fundamental and important parameter to measure. Over the past decade, observations have revealed that sizes of galaxies at a given stellar mass were smaller at higher redshifts and change significantly with redshift. It has been shown that the sizes of galaxies correlate with their stellar masses and that this correlation exists at least up to $z \sim 3$ (e.g., Franx et al. 2008, Williams et al. 2010, Mosleh et al. 2011, Law et al. 2012).

There are many proposed scenarios to explain the physical processes of galaxy assembly that plausibly reproduce the observable stellar mass and size of galaxies at different redshifts (e.g., galaxy minor or major mergers; Khochfar & Silk 2006, 2009, Bell et al. 2006, Naab et al. 2009) or gas accretion in outer regions and star formation (Dekel et al. 2009, Elmegreen et al. 2008). Accurate measurements of both *stellar masses* and *sizes* of galaxies over a wide redshift range are fundamentally important to constrain these galaxy formation models.

To extend the mass-size relation of galaxies to the highest redshifts, we exploit the Lyman break galaxies (LBGs) which are star-forming galaxies with strong rest-frame UV emission and could be selected by photometric dropout techniques (e.g., Steidel et al. 2003, Adelberger et al. 2004). These galaxies can be identified out to very high redshifts (e.g., $z \sim 8$; Oesch et al. 2012, Yan et al. 2011) and thus provide insight into the early evolution of the mass-size relation.

Morphological studies of LBGs ($z \sim 2 - 6$) in rest-frame UV have shown that these galaxies are mostly compact sources however, multiple core LBGs have also been found (e.g., Ravindranath et al. 2006, Law et al. 2007, Conselice & Arnold 2009). Analyzing their size and structure could help to interpret the dominant mechanism for galaxy growth. The new Wide Field Camera 3 (WFC3) onboard the *Hubble Space Telescope* (*HST*) can provide sizes of high-z galaxies in longer rest-frame wavelengths than Advanced Camera for Survey (ACS).

Size studies of galaxies at redshifts $z > 4$ using profile fitting techniques are rare (Oesch et al. 2010). Here for the first time, we investigate the mass-size relation of dropout galaxies up to the very early stages of galaxy formation, using the advantages of wide-area *HST* surveys and high spatial resolution of WFC3. We measure the sizes of LBGs at approximately the same rest-frame wavelength at different redshifts, minimizing the effects of morphological K-correction. We utilize observations of both Hubble Ultra Deep Field (HUDF) and the deep wide-area Early Release Science (ERS) field to study the mass-size relation of the largest sample of LBGs at $z \sim 4 - 7$ so far. The cosmological parameters adopted throughout this Letter are $\Omega_m = 0.3$, $\Omega_\Lambda = 0.7$, and $H_0 = 70 \ km \ s^{-1} \ Mpc^{-1}$.

3.2 Description of Data

The sample of dropout sources at $z \sim 4 - 7$ used here is based on recent *HST*-WFC3/IR observations over the HUDF and ERS field (see Bouwens et al. 2011, Oesch et al. 2010b, González et al. 2010). Our sample of dropout galaxies is taken from Bouwens et al. (2011) and González et al. (2011). Their candidates are selected by utilizing color criteria (Lyman break technique) for selecting *B*-, *V*-, *i*- and *z*- dropouts similar to those used in Oesch et al. (2010b) and Bouwens et al. (2007, 2011). Their sample consists of 679 objects at $z \sim 4 - 6$ in ERS field and 345 dropouts at $z \sim 4 - 7$ in HUDF.

For all candidate galaxies in this Letter we use the stellar masses measured by González et al. (2011). These authors used FAST (Kriek et al. 2009) to fit template galaxy spectral energy distributions to photometry in ACS, WFC3/IR, and IRAC [3.6] and [4.5] filters. They used Bruzual & Charlot (2003) stellar population evolution models with constant star formation histories and assumed a Salpeter (1955) initial mass function (IMF; $0.1 - 100 M_\odot$) and $0.2\ Z_\odot$ solar metallicity. Reliable deblended IRAC fluxes and photometry in different bands (with different point-spread functions, PSFs) were obtained by using a source-fitting algorithm described in Labbé et al. (2006) (see also González et al. 2010).

The photometric deblending for the IRAC imaging does not properly work for objects in crowded regions due to the large PSF of IRAC bands; due to this, the number of sources with reliable mass estimates is reduced to 60% (see also González et al. 2011). The stellar masses are corrected to a Kroupa (2001) IMF by a reduction of 0.2 dex (see Marchesini et al. 2009). These are consistent with the Sloan Digital Sky Survey (SDSS) masses.

The near-IR images used in this study are taken from the full two-year WFC3/IR HUDF (Y_{105}, J_{125}, H_{160};(Bouwens et al. 2011, Oesch et al. 2010b)) and ERS (Y_{098}, J_{125}, H_{160}; (Bouwens et al. 2011)) data. The data set covers ~ 4.7 arcmin^2 in the HUDF and ~ 40 arcmin^2 in the ERS (in GOODS-South) field with a pixel scale of 0.06″ and a PSF FWHM of ~ 0.17″ in the *H*-band. We also use very deep images of the HUDF field obtained with the ACS (Beckwith et al. 2006) and deep GOODS ACS/WFC data over the GOODS field (Giavalisco et al. 2004) with a pixel scale of 0.03″ and a PSF FWHM of ~ 0.10″. The reduction of these data is described in Bouwens et al. (2011), and references there in.

As explained in the next section, we use sizes of objects in the band closest to the rest-frame 2100Å. Therefore, in addition to reliable stellar mass cut, we restrict our size measurements to objects with sufficient signal-to-noise ratio (S/N) in their size measurement band. Hence, we use $H_{160} < 28.5$ in HUDF and $H_{160} < 26.2$ AB mag in ERS field (corresponding to 10σ in 0.5″ apertures) for *i*-dropouts and *z*-dropouts, $J_{125} < 28.5$ in HUDF and $J_{125} < 26.5$ AB mag in ERS for *V*-dropouts and $Y_{105} < 28.3$ in HUDF and $Y_{098} < 26.4$ AB mag in ERS for *B*-dropouts. Our simulations (see Section 3.3) show that systematic uncertainties on size estimates are small up to these magnitudes. Moreover, objects with poor S/N ($< 5\sigma$) are not included in our analysis. Thus, the final sample consists of 156 *B*-dropouts ($z \sim 4$), 45 *V*-dropouts ($z \sim 5$), 13 *i*-dropouts ($z \sim 6$), and 4 *z*-dropouts ($z \sim 7$).
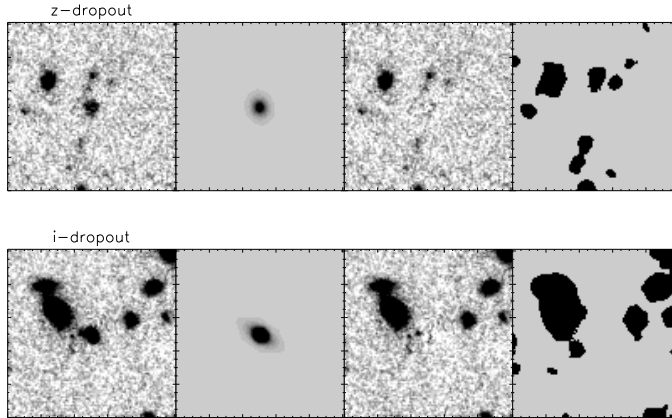
Figure 3.1 – From left to right, *H*-band postage stamps (6″ × 6″), best-fit models from GALFIT, residual images and mask maps are shown for a *z*-dropout candidate (top row), and an *i*-dropout candidate (bottom row). The quality of the fits can be seen from the residual images.

3.3 Sizes

Our size measurements are performed in a similar way as in Mosleh et al. (2011). PSF-convolved Sérsic models are fit to all galaxies using the GALFIT version 3 package (Peng et al. 2010). We measure sizes in filters described in the previous section.

GALFIT requires an accurate PSF of the image to convolve the Sérsic profile models in order to find the best (χ^2 minimized) fit. For the HUDF WFC3/IR images we use a PSF created using TinyTim (Krist 1995). Although, we prefer using empirically determined PSFs (from stars), in the HUDF there are not enough stars to create a sufficiently low-noise PSF for deconvolution. We note that our test shows that sizes measured using non-saturated star as a PSF give results which are consistent with those based on TinyTim created PSFs. For the ACS images in the HUDF we use non-saturated stars in the field to make a median-stacked PSF. In the ERS field, we use a median-stacked PSF using non-saturated stars in the field for all optical and near-IR bands (ACS and WFC3/IR).

GALFIT measures the half-light radius along the semimajor axis, a, and the axis ratio, b/a, of each galaxy. We determine the circularized effective radius of the galaxies ($r_e = a \sqrt{b/a}$) to remove the effects of ellipticity. We fix the Sérsic index to 2.5 where GALFIT fails to return reliable measurements; i.e., for objects with large uncertainties in their output parameters. Size determination for all objects while fixing the Sérsic index to 2.5 reveals that this will not introduce systematics in our size study. Fixing Sérsic index to 1.5 or 3 gives similar size estimates as for $n = 2.5$. In Figure 3.1 we show from left to right, postage stamps in the *H* band, best-fit models from GALFIT, residual images, and mask maps for a *z*-dropout (top row) and an *i*-dropout (bottom row) in the HUDF.
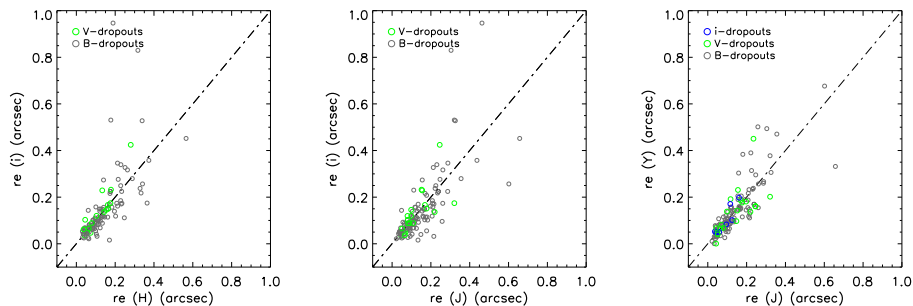
Figure 3.2 – Comparison of sizes of dropout candidates measured in different filters with S/N> 10 in both the HUDF and ERS. Each color represents a different sample of dropout candidates. The correlation between estimated sizes in different bands is an indication of the reliability of our size measurements. The small offsets between sizes in different bands maybe due to color gradients in the galaxies. The objects with large offsets from the one-to-one relation have generally a clumpy structure or multiple cores.

The low-level residuals shows that our best-fit models closely match the observed galaxy images.

We first test the accuracy of our measurements by comparing the effective radii, r_e, measured at different wavelengths. A comparison of the sizes of our dropout candidates is shown in Figure 3.2. Each dropout sample is represented by a different color: *B*-dropouts are black, *V*-dropouts are green, and *i*-dropouts are blue. We note that ACS has a much smaller PSF and finer pixel scale, and it is known to produce highly reliable size measurements from previous studies. The correlation between estimated sizes in different bands, is an indicator of the size measurements reliability. Since color gradients and clumpy star formation may introduce additional r_e scatter between bands, these comparisons essentially show an "upper limit" to the intrinsic uncertainties.

In addition, we have performed realistic simulations on both the HUDF and ERS fields analogous to Mosleh et al. (2011), by adding model galaxies to the images and measuring their parameters in the same way as for real objects. From the simulations, the relative difference between the recovered and input sizes versus magnitude shows that the systematic uncertainties on the recovered sizes are very small (< 10%) down to S/N ratio of 10 (corresponding to $H_{160} < 28.5$ in the HUDF and $H_{160} < 26.2$ in the ERS).

Finally, in order to minimize the effects of morphological *K*-correction, we use sizes of each object in the WFC3/IR or ACS band that is closest to the rest-frame 2100Å. Therefore in this study the Y_{105}-band images are used for *B*-dropouts, J_{125} images are used for *V*-dropouts and H_{160}-band images for *i* and *z*-dropouts.

3.4 Results

3.4.1 Size-Mass Evolution

The size and stellar mass estimates of our dropout candidates allow us to investigate the mass-size relation and its evolution. Figure 3.3 shows the mass-size relation for four redshift bin from $z = 4$ to $z = 7$. There is a clear relation out to $z \sim 5$ and a hint at $z \sim 6$ for galaxies with $\log(M_*/M_\odot) > 8.6$. In each panel, color points represent the distributions of candidates in the mass-size plane. Objects with S/N $< 2\sigma$ in the IRAC [3.6] channel, are indicated by open symbols, and those with higher S/N (i.e., more reliable stellar mass) are shown as filled circles. The pink stars indicate the median sizes of galaxies in different stellar mass bins down to our estimated stellar mass limit. The dot-dashed line in each panel represents the mass-size relation for late-type galaxies (i.e., $n < 2.5$) in the local universe from Shen et al. (2003) and the dashed line represents the best-fit stellar mass-size relation for UV-bright galaxies at $z \sim 2$ from Mosleh et al. (2011). According to our simulations, sizes below the dotted lines (corresponding to apparent radii of 0.05″) have large uncertainties and can be conservatively thought of as upper limits.

The stellar mass-size relation for $z \sim 4$ and $z \sim 5$ is characterized by $r_e \propto M^\alpha$ with $\alpha = 0.14 \pm 0.06$ and 0.17 ± 0.07, respectively. These are significantly different from zero. We note that the correlation coefficients are 0.22 at $z \sim 4$ and 0.37 at $z \sim 5$. At $z \sim 6$, there might be a hint of a mass-size relation, but there are too few galaxies in our sample at this redshift to either confirm or rule out a relation. We note that the size and stellar mass of these galaxies need not to be correlated as the sizes are measured in the rest-frame UV and the stellar masses in optical rest-frame. Nonetheless, the results show the persistence of the mass-size relation for star-forming galaxies up to very high redshifts. We also note that the fraction of contaminants in our dropout samples is relatively small ($< 11\%$)(see Bouwens et al. (2011, 2007) for more details) and hence unlikely biased the relations.

The black diamond in the lower left panel of Figure 3.3 shows the position in the mass-size relation of an i-dropout galaxy ($SBM03\#1$ in HUDF) from Eyles et al. (2005). This object has a robust spectroscopic redshift ($z = 5.83$) and a stellar mass of a few times $10^{10} M_\odot$. The size estimate for this object is consistent with the median size estimate of i-dropouts in our higher mass bin.

3.4.2 Size Evolution at Fixed Mass

Comparing the median sizes of LBGs for a given stellar mass at different epochs, illustrates the evolution of galaxies effective radii at fixed stellar masses with redshift. This size evolution is shown in Figure 3.4. Galaxies are split into two stellar mass bins: $9.5 < \log(M_*/M_\odot) < 10.4$ (shown in the left panels) and $8.6 < \log(M_*/M_\odot) < 9.5$ (shown in the right panels). For the objects in the lower redshift range (i.e., $z \sim 1 - 3$), we used sizes measured for UV-bright galaxies in the same stellar mass range from our previous studies by Mosleh et al. (2011). In order to measure the size evolution consistently we use similar technique described in Newman et al. (2012) to normalize sizes of galaxies with $r_e \propto M^{0.30}$ to stellar mass of $10^{9.7} M_\odot$ (left panels) and $10^9 M_\odot$ (right panels). In the bottom
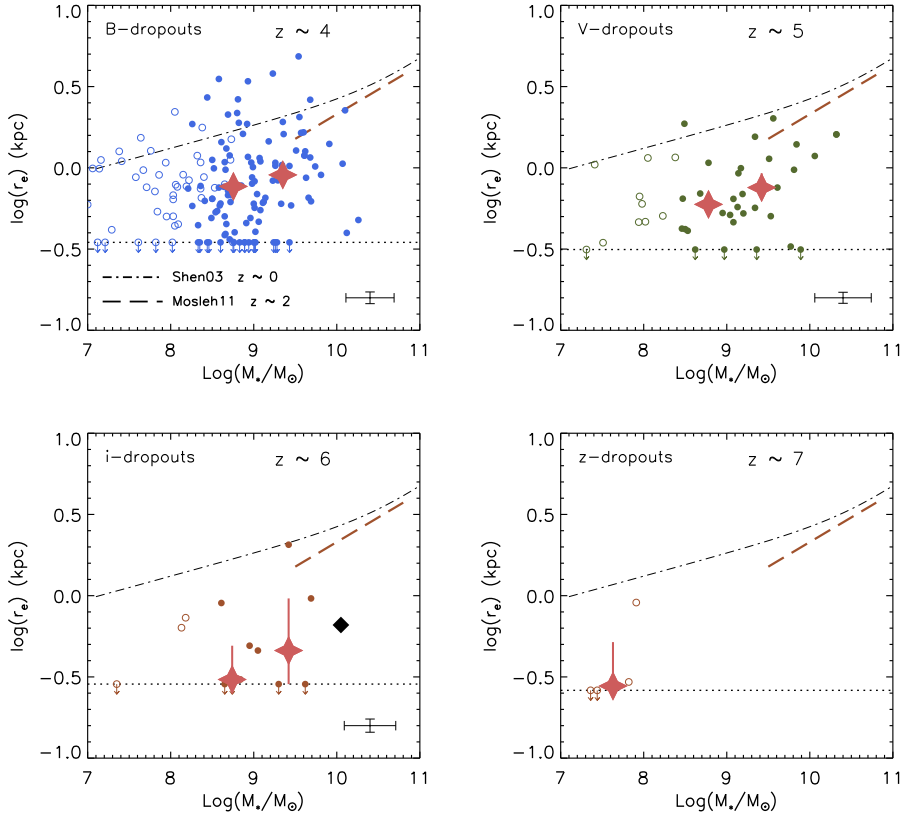
45

Figure 3.3 – Mass-size relation for dropout galaxies in different redshift bins. The filled circles indicate sizes for galaxies with reliable stellar masses ($> 2\sigma$ detection in IRAC[3.6]). The pink large stars are the median of sizes from GALFIT in different stellar mass bins with the errors calculated by bootstraping. The black diamond in the lower left panel is an *i*-dropout galaxy at $z \sim 6$ with a stellar mass of a few times $10^{10} M_\odot$ from Eyles et al. (2005). The dashed and dot-dashed lines show the mass-size relation for UV-bright galaxies at $z \sim 2$ from Mosleh et al. (2011) and for late-type galaxies at $z \sim 0$ from Shen et al. (2003), respectively. The dotted lines correspond to our size measurement limits. Typical errors of the points are shown in the lower right of each panel. This plot shows that mass-size relation holds out to $z \sim 5$, and possibly beyond for galaxies with $\log(M_*/M_\odot) > 8.6$. Sizes decrease toward higher redshift.
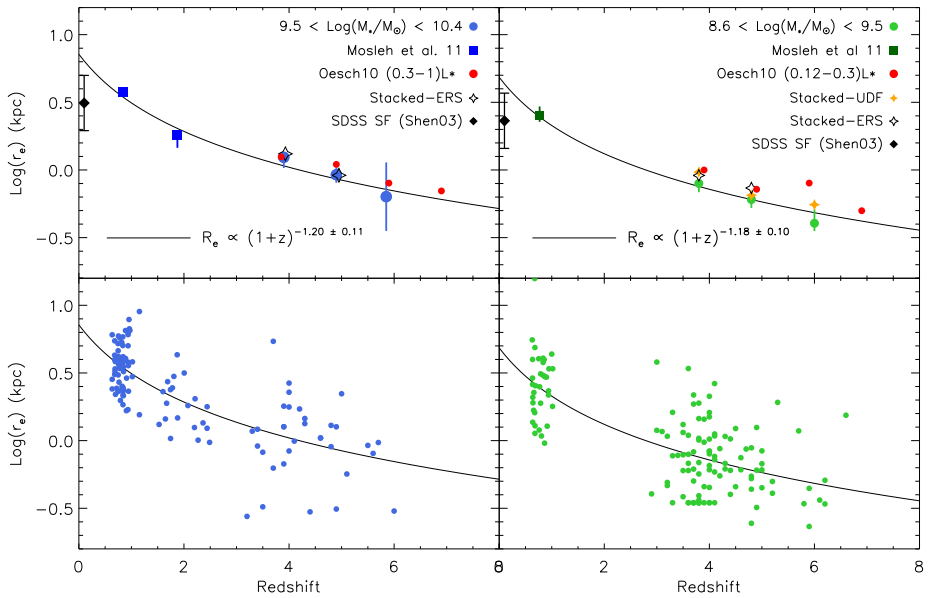
Figure 3.4 – Redshift evolution of the sizes of dropout galaxies in two stellar mass ranges: $\log(M_*/M_\odot) \sim 9.5 - 10.4$ (left panels) and $\log(M_*/M_\odot) \sim 8.6 - 9.5$ (right panels). The lower panels show the distribution of sizes for all sources in our analysis and the sizes of UV-bright galaxies at $z \sim 1 - 3$ within the same mass range from Mosleh et al. (2011). The best power-law fits to these data points are shown as solid lines. The red points are from Oesch et al. (2010) for a luminosity-selected sample. The black and yellow stars are the sizes derived by stacking galaxies in the same stellar mass range. The black diamonds in the top panels indicate median size of local late-type galaxies from Shen et al. (2003).

panels, blue and green points represent normalized half-light radii of dropout objects as a function of redshift.

We fit a simple power law of the form $(1 + z)^{-m}$ to the observed points (bottom panels of Figure 3.4); the best fits are shown as solid lines. In the high stellar mass bin, galaxy sizes are found to evolve as $(1 + z)^{-1.20 \pm 0.11}$, and for galaxies with lower stellar masses the size evolves as $(1 + z)^{-1.18 \pm 0.10}$.

In the top panels of Figure 3.4, blue and green solid circles represent the median effective radii of dropouts from this study, and the solid squares are median sizes in lower redshift bins. The red points are the mean galaxy sizes from Oesch et al. (2010) for two different luminosity ranges: $(0.3 - 1)L_{* \; z=3}$ in the left panel and $(0.12 - 0.3)L_{* \; z=3}$ in the right panel.

The filled yellow and open black stars in the top panels are sizes based on stacking galaxies from fixed stellar mass ranges for our two fields. For stacking, we used the central positions of objects determined by GALFIT and replaced contaminated pixels from neighboring sources with sky background values. We then used GALFIT to measure the half-light radii of our final stacked images. As shown by, e.g., Hathi et al. (2008a) and Oesch et al. (2010), stacking can reproduce reliable average surface brightness profiles. Thus, the agreement between the median points and results of stacking suggests that we are not systematically missing light in the extended wings of galaxies and that on average our size estimates are robust.

3.5 Summary And Discussion

For the first time, we have studied the stellar mass-size relation of LBGs out to $z \sim 7$ using ultradeep WFC3/IR observations in the HUDF and ERS fields. We have shown that the mass-size relation of star-forming galaxies persists to very high redshifts, and that at fixed stellar mass, the sizes of galaxies increase significantly toward later cosmic time. The observed size growth of LBGs studied here $- r_e \propto (1 + z)^{-1.20 \pm 0.11}$ for galaxies with stellar mass of $10^{9.5}$-$10^{10.4} M_\odot$ – is in agreement with previous stellar mass-size studies at $z \lesssim 3$ (e.g., Dahlen et al. 2007, Mosleh et al. 2011, Nagy et al. 2011, Law et al. 2012). It is also consistent with the size evolution estimated by other studies based on luminosity-selected samples (e.g., Ferguson et al. 2004, Bouwens et al. 2004, 2006, Hathi et al. 2008b, Oesch et al. 2010).

The redshift dependence of the size evolutions is very similar for both high and low stellar masses. Therefore, the galaxy size evolution might be written as a separable function of mass and redshift and this would be in agreement with simple models of galaxy formation developed for high-redshift systems (see Wyithe & Loeb 2011). However, our sample is not stellar mass complete; hence using deeper samples in future is needed for further investigations.

In Figure 3.5, we compare our estimated size-redshift relation for LBGs with those in Law et al. (2012) (blue triangles) and Dahlen et al. (2007) (open squares). The sizes are normalized to a stellar mass of $10^{10} M_\odot$. The size estimates from different studies are
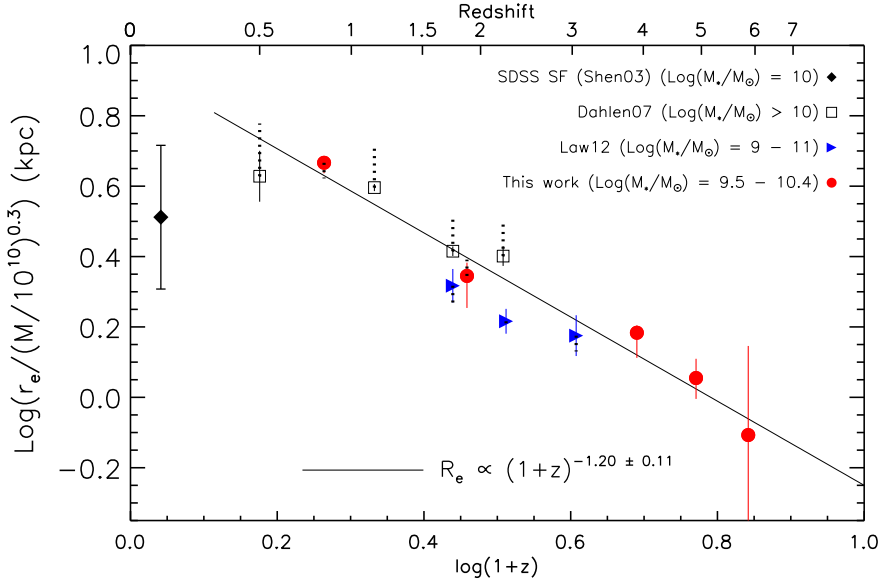
Figure 3.5 – Comparison of sizes of UV-bright galaxies measured by different authors. In order to have a consistent comparison, sizes are normalized using $r_e \propto M^{0.30}$ for a stellar mass of $10^{10} M_\odot$. The solid line is the best fit from our analysis ($r_e \propto (1 + z)^{-1.20\pm0.11}$). The dotted lines represent the original (not normalized) size measurement. The black solid diamond is the median size of late-type galaxies at $z \sim 0$ for stellar masses around $10^{10} M_\odot$ from Shen et al. (2003), with the measured dispersion shown as error bar. The sizes of UV-bright galaxies at fixed stellar mass increases rapidly toward later cosmic time. However, the sizes measured for local late-type galaxies are smaller than the sizes of UV-bright galaxies at $z \sim 1$. These samples most likely comprise intrinsically different galaxies.

consistent with the best fit found in this study ($m = 1.20 \pm 0.11$, solid line). This suggests that LBGs may evolve into UV-bright galaxies at $z \sim 1$. At $z \sim 6$ these galaxies are extremely compact: $r_e \sim 0.8$ kpc, at stellar mass of $10^{10} M_\odot$. However, they grow by a factor of about 6 to $z \sim 0.85$. The $z \sim 6$ galaxies have a mass size relation close to those of the compact quiescent galaxies at $z \sim 2$; for example, the normalized size ($r_e/(M/10^{10})^{0.3}$) of a sample of quiescent galaxies at $z \sim 2$ studied by Szomoru et al. (2012) is ~ 0.6 kpc.
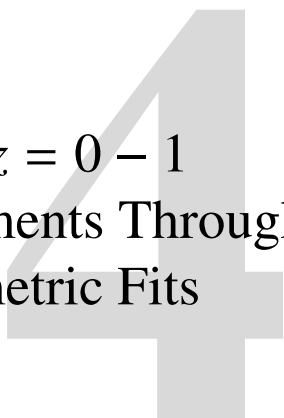
The scarcity of observed LBGs between $z \sim 0$ and $z \lesssim 1$, complicates the interpretation of the evolution of their stellar mass-size relation to the present time. The median size measured for local late-type (i.e., $n < 2.5$) SDSS galaxies by Shen et al. (2003) at the same stellar mass (black solid diamond in Figures 3.4 and 3.5, corrected to the rest-frame UV using the analysis by Gil de Paz et al. (2007), Azzollini et al. (2009), and D. Szomoru 2012, private communication) is smaller than the size of $z \sim 1$ UV-bright galaxies. We note that the SDSS late-type sample is most likely a different galaxy population than the UV-bright sources we study at $z \gtrsim 1$ and is therefore not relevant for direct comparison. Overzier et al. (2010) studied 30 local Lyman break analogs ($z < 0.3$), however this sample was selected to have a surface brightness limit and is therefore not characteristic of star-forming galaxies in the nearby universe. In addition, there is some evidence that the evolution of the stellar mass-size relation for star-forming galaxies is slower between $z = 1$ and $z = 0$ (e.g., Barden et al. 2005). This needs further investigation using homogeneously selected sample in future.

Bibliography

Adelberger, K. L., Steidel, C. C., Shapley, A. E., Hunt, M. P., Erb, D. K., Reddy, N. A., & Pettini, M. 2004, ApJ, 607, 226

Azzollini, R., Beckman, J. E., & Trujillo, I. 2009, A&A, 501, 119

Barden, M., et al. 2005, ApJ, 635, 959

Beckwith, S. V. W., et al. 2006, AJ, 132, 1729

Bell, E. F., et al. 2006, ApJ, 640, 241

Bouwens, R. J., Illingworth, G. D., Blakeslee, J. P., Broadhurst, T. J., & Franx, M. 2004, ApJ, 611, L1

Bouwens, R. J., Illingworth, G. D., Blakeslee, J. P., & Franx, M. 2006, ApJ, 653, 53

Bouwens, R. J., Illingworth, G. D., Franx, M., & Ford, H. 2007, ApJ, 670, 928

Bouwens, R. J., et al. 2011, ApJ, 737, 90

Bruzual, G., & Charlot, S. 2003, MNRAS, 344, 1000

Conselice, C. J., & Arnold, J. 2009, MNRAS, 397, 208

Dahlen, T., Mobasher, B., Dickinson, M., Ferguson, H. C., Giavalisco, M., Kretchmer, C., & Ravindranath, S. 2007, ApJ, 654, 172

Dekel, A., Sari, R., & Ceverino, D. 2009, ApJ, 703, 785

Elmegreen, B. G., Bournaud, F., & Elmegreen, D. M. 2008, ApJ, 688, 67

Eyles, L. P., Bunker, A. J., Stanway, E. R., Lacy, M., Ellis, R. S., & Doherty, M. 2005, MNRAS, 364, 443

Ferguson, H. C., et al. 2004, ApJ, 600, L107

Franx, M., van Dokkum, P. G., Schreiber, N. M. F., Wuyts, S., Labbé, I., & Toft, S. 2008, ApJ, 688, 770

Giavalisco, M., et al. 2004, ApJ, 600, L93

Gil de Paz, A., et al. 2007, ApJS, 173, 185

González, V., Labbé, I., Bouwens, R. J., Illingworth, G., Franx, M., & Kriek, M. 2011, ApJ, 735, L34+

González, V., Labbé, I., Bouwens, R. J., Illingworth, G., Franx, M., Kriek, M., & Brammer, G. B. 2010, ApJ, 713, 115

Hathi, N. P., Jansen, R. A., Windhorst, R. A., Cohen, S. H., Keel, W. C., Corbin, M. R., & Ryan, Jr., R. E. 2008a, AJ, 135, 156

Hathi, N. P., Malhotra, S., & Rhoads, J. E. 2008b, ApJ, 673, 686

Khochfar, S., & Silk, J. 2006, ApJ, 648, L21

—. 2009, MNRAS, 397, 506

Kriek, M., van Dokkum, P. G., Labbé, I., Franx, M., Illingworth, G. D., Marchesini, D., & Quadri, R. F. 2009, ApJ, 700, 221

Krist, J. 1995, in Astronomical Society of the Pacific Conference Series, Vol. 77, Astronomical Data Analysis Software and Systems IV, ed. R. A. Shaw, H. E. Payne, & J. J. E. Hayes, 349–+

Kroupa, P. 2001, MNRAS, 322, 231

Labbé, I., Bouwens, R., Illingworth, G. D., & Franx, M. 2006, ApJ, 649, L67

Law, D. R., Steidel, C. C., Erb, D. K., Pettini, M., Reddy, N. A., Shapley, A. E., Adelberger, K. L., & Simenc, D. J. 2007, ApJ, 656, 1

Law, D. R., Steidel, C. C., Shapley, A. E., Nagy, S. R., Reddy, N. A., & Erb, D. K. 2012, ApJ, 745, 85

Marchesini, D., van Dokkum, P. G., Förster Schreiber, N. M., Franx, M., Labbé, I., & Wuyts, S. 2009, ApJ, 701, 1765

Mosleh, M., Williams, R. J., Franx, M., & Kriek, M. 2011, ApJ, 727, 5

Naab, T., Johansson, P. H., & Ostriker, J. P. 2009, ApJ, 699, L178

Nagy, S. R., Law, D. R., Shapley, A. E., & Steidel, C. C. 2011, ApJ, 735, L19

Newman, A. B., Ellis, R. S., Bundy, K., & Treu, T. 2012, ApJ, 746, 162

Oesch, P. A., et al. 2010a, ApJ, 709, L21

—. 2010b, ApJ, 709, L16

—. 2012, arXiv:1201.0755

Overzier, R. A., Heckman, T. M., Schiminovich, D., Basu-Zych, A., Gonçalves, T., Martin, D. C., & Rich, R. M. 2010, ApJ, 710, 979

Peng, C. Y., Ho, L. C., Impey, C. D., & Rix, H.-W. 2010, AJ, 139, 2097

Ravindranath, S., et al. 2006, ApJ, 652, 963

Salpeter, E. E. 1955, ApJ, 121, 161

Shen, S., Mo, H. J., White, S. D. M., Blanton, M. R., Kauffmann, G., Voges, W., Brinkmann, J., & Csabai, I. 2003, MNRAS, 343, 978

Steidel, C. C., Adelberger, K. L., Shapley, A. E., Pettini, M., Dickinson, M., & Giavalisco, M. 2003, ApJ, 592, 728

Szomoru, D., Franx, M., & van Dokkum, P. G. 2012, ApJ, 749, 121

Williams, R. J., Quadri, R. F., Franx, M., van Dokkum, P., Toft, S., Kriek, M., & Labbé, I. 2010, ApJ, 713, 738

Wyithe, J. S. B., & Loeb, A. 2011, MNRAS, 413, L38

Yan, H., et al. 2011, arXiv:1112.6406

On the Robustness of $z = 0 - 1$ Galaxy Size Measurements Through Model and Non-Parametric Fits

Moein Mosleh, Rik J. Williams, Marijn Franx
Submitted to The Astrophysical Journal, 2013

Abstract

We present the size-stellar mass relations of nearby ($z = 0.01 - 0.02$) SDSS galaxies, for samples selected by color, morphology, Sérsic index n, and specific star formation rate. Several commonly-employed size measurement techniques are used, including single Sérsic fits, two-component Sérsic models and a non-parametric method. Through simple simulations we show that the non-parametric and two-component Sérsic methods provide the most robust effective radius measurements, while those based on single Sérsic profiles are often overestimates, especially for massive red/early-type galaxies. Using our robust sizes, we show that for all sub-samples, the mass-size relations are shallow at low stellar masses and steepen above $\sim 3 - 4 \times 10^{10} M_\odot$. The mass-size relations for galaxies classified as late-type, low-n, and star-forming are consistent with each other, while blue galaxies follow a somewhat steeper relation. The mass-size relations of early-type, high-n, red, and quiescent galaxies all agree with each other but are somewhat steeper at the high-mass end than previous results. To test potential systematics at high redshift, we artificially redshifted our sample (including surface brightness dimming and degraded resolution) to $z = 1$ and re-fit the galaxies using single Sérsic profiles. The sizes of these galaxies before and after redshifting are consistent, and we conclude that systematic effects in sizes and the size-mass relation at $z \sim 1$ are negligible. Interestingly, since the poorer physical resolution at high redshift washes out bright galaxy substructures, single-Sérsic fitting appears to provide more reliable and unbiased effective radius measurements at high z than for nearby, well-resolved galaxies.

4.1   Introduction

Correlations among galaxy physical parameters such as stellar mass, luminosity, size, velocity dispersion, and their evolution with cosmic time are crucial for understanding the formation and evolution of galaxies and imposing constraints on theoretical models of their structural assembly. Morphological scaling relations such as the relation between size and surface brightness, the correlation between size and luminosity (Kormendy 1985), and the relation between the effective radius and stellar mass (Shen et al. 2003, hereafter S03), vary for different types of galaxies. The differences between surface brightness profiles and sizes of galaxies are the products of the different physical processes governing their formation and evolution. Precise measurements of these galaxy properties at low and high redshifts thus provide strong constraints on models of galaxy formation and evolution.

Among these relations is the observed correlation between half-light radius (size) and stellar mass, which is shown for the local Universe (S03) and persists up to very high redshifts (e.g., Daddi et al. 2005, Trujillo et al. 2006b, Franx et al. 2008, Buitrago et al. 2008, Cimatti et al. 2008, van der Wel et al. 2008, Williams et al. 2010, Dutton et al. 2011, Law et al. 2012, Mosleh et al. 2011, 2012). These authors also pointed out that sizes of galaxies at fixed stellar mass decrease as the redshift increases, i.e., galaxies were smaller in the past. For instance, massive quiescent galaxies at $z \sim 2$ are about a factor of ~ 6 smaller than their counterparts at $z \sim 0$ (e.g., Daddi et al. 2005, van Dokkum et al. 2008). Understanding the mechanism of the size evolution and how galaxies reach the mass-size relation at $z = 0$ requires measuring these properties, especially sizes, very robustly in different redshift ranges.

One of the main concerns is the accuracy of galaxy size determination at high redshifts. Galaxies at higher redshifts are at larger distances and therefore are dimmer and have smaller apparent angular sizes. The low surface brightness envelopes of galaxies could fade away due to cosmological dimming and could have lower signal to noise ratios (S/N), hence, may potentially bring systematics on their real size measurements. For example, the outer parts of early-type galaxies normally fade away gradually into the background sky noise, and it is very hard to define precise edges for these types of galaxies. Underestimating the sizes of these galaxies at high redshifts could have an effect on the inferred rate of size evolution (Mancini et al. 2010).

There are several possible approaches to test the smallness of galaxies at high redshifts. Recently, Szomoru et al. (2010) used deep observations with the Wide Field Camera 3 (WFC3) instrument on board the Hubble Space Telescope (HST) to measure the size of a massive quiescent galaxy at $z \sim 2$ based on a new approach (correcting the best-fit Sérsic profile of the galaxy with the residual of the fit) to confirm the compactness of this massive galaxy at this redshift.

The other method in order to check the effects of cosmological redshift on the size/shape measurements is to artificially transform nearby galaxies to higher redshifts. Comparing derived parameters before and after redshifting provides a test for biases that may be introduced by degraded resolution and cosmological surface brightness dimming. This technique has been used in the past for different purposes, for instance assessing mor-

phologies at higher redshifts (e.g., Petty et al. 2009, Conselice et al. 2011, van den Bergh et al. 2002, Lisker et al. 2006, Giavalisco et al. 1996). Recently, Barden et al. (2008) used a set of ~ 100 local galaxies to study the cosmological redshifting effect on size and shape of galaxies at $0.1 < z < 1.1$. They created new images from the best-fit single Sérsic models of their input images, and then redshifted them to show that there is not any systematics on the size and morphological parameters. However, nearby galaxies have signs of different sub-structures and low surface brightness features. Generating simulated galaxies with a comparable range of properties of galaxies and adding them into the blank sky background images is a practical test. However, these mock objects are simple cases compare to real objects and could be assumed as a lower limit on the systematics (e.g., Trujillo et al. 2006b).

It is also a common practice to measure the surface brightness profile of galaxies at high-z single component Sérsic profile fitting. Therefore, it is assumed that for a consistent comparison of sizes at low and high-z, the profiles of nearby galaxies also should be measured with the same method. However, as mentioned earlier, galaxies often consist of multiple components (e.g., bars, bulges, compact cores, spiral arms, etc,). In the local Universe, these sub-components are well-resolved and distinguishable in the photometric analysis of their structures. Therefore their surface brightness profiles may deviate from a single component model. It has been shown that using extra components in fitting surface brightness profiles of nearby galaxies better describes the underlying stellar distributions than using canonical single Sérsic profile fitting (e.g., for Elliptical galaxies: Ferrarese et al. 1994, Lauer et al. 1995, Graham et al. 2003, Huang et al. 2012, also see references therein). Some authors have also shown that using single component Sérsic profile fitting for nearby galaxies with more than one component might systematically bias sizes and morphological parameters (e.g., Meert et al. 2012, Bernardi et al. 2012).

Therefore, in this paper, we first investigate the biases associated with estimating sizes of nearby galaxies using single Sérsic profile fitting and its effect in their comparison to galaxies at high redshifts. These effects will also be tested against various types of galaxies (e.g., classifications according to their morphology, color, star-formation rate). We will explore the possible dependence of the systematics of sizes on the galaxies classifications and test alternate (two-component and nonparametric) methods.

We also artificially redshift real images of nearby galaxies ($z \sim 0$) to $z = 1$ in order to investigate the uncertainties of parameter measurements. We will use the resolution of HST WFC3 instrument, since images from this instrument are now being widely used for studying galaxy structures at high redshifts (Oesch et al. 2010, Szomoru et al. 2012, Patel et al. 2012, Newman et al. 2012, Mosleh et al. 2012, van de Sande et al. 2012, etc.). Moreover, for the sake of better statistics, we use a large sample of nearby galaxies (~ 1000 objects).

Finally, we will use our robust size measurements to study the correlation of size and stellar masses of our nearby galaxies. Galaxies can be selected or classified by means of different methods or criteria, such as morphology, color and star-formation rate. We investigate the mass-size relation for different types of nearby galaxies at a wide range of stellar masses and test whether the selection criteria could affect the mass-size relations. These relations provide a baseline for further studies at high redshifts. We will also

compare the mass-size relations of galaxies after artificially redshifting them to $z = 1$ and examine if the robustness of galaxies mass-size relations at high redshifts.

We explain our sample used in this study in section 4.2. The size determination methods and their systematic offsets at $z \sim 0$ are explored in section 4.3. The stellar mass-size relations of nearby galaxies are studied in section 4.4. We describe the artificially redshifting procedure of galaxies to $z = 1$ and their sizes compare to $z = 0$ in section 4.5. We discuss our results in section 4.6. The cosmological parameters adopted throughout this paper are $\Omega_m = 0.3$, $\Omega_\Lambda = 0.7$ and $H_0 = 70 \ km \ s^{-1} \ Mpc^{-1}$.

4.2 Data

The sample of galaxies we use for this study is selected from the MPA-JHU SDSS DR7 (Kauffmann et al. 2003, Salim et al. 2007) which have spectroscopic redshifts for SDSS DR7 galaxies (Abazajian et al. 2009) galaxies. The surface brightness limit for our sample is $\mu_{50} \leq 23$ mag arcsec^2 with magnitude limit of $r \leq 17.77$. We initially select galaxies to have spectroscopic redshifts within $0.01 < z < 0.02$ and stellar masses of $\log(M_*/M_\odot) \geq 9$. As we intend further to artificially redshift galaxies to $z = 1$, the imposed redshift limits are to avoid selecting galaxies where the SDSS PSF is broader than the WFC3 PSF at $z = 1$ (and providing sufficient sampling at high-z, see Barden et al. 2008, for more details), and also to avoid objects with very large apparent sizes. To reduce processing time, we further select about 1000 galaxies randomly from this sub-sample (about one-third of galaxies in this mass and redshift range). We use SDSS r-band images for measuring their sizes at this low-z.

We classify our sample into different sub-samples based on their color, morphology and specific star-formation rate (sSFR). The left panel of Figure 4.1 shows the distributions of all galaxies on color-magnitude diagram. The color and absolute magnitude are based on the New York University Value-Added Galaxy Catalog (NYU-VAGC Blanton et al. 2005). Parallel to the red sequence distribution, we define the following line to separate galaxies into red and blue ones:

$$(g - r) = 0.68 - 0.032(M_r + 20) \tag{4.1}$$

In order to classify galaxies based on their morphology, we used the Galaxy Zoo catalog (GZ1) (Lintott et al. 2011) which is a morphological catalog of visually classified SDSS galaxies. We classify galaxies into early-types and late-types based on debiasing fraction of the votes for each galaxy being dominant (see Lintott et al. (2011) for more details). We note that the classification are only available for $\sim 94\%$ of our sample. The color magnitude distributions of these early-types and late-types are shown in middle panel of Figure 4.1. Early-type galaxies are indicated as red symbols and late-type ones as blue.

Galaxies can also be selected by means of their specific star-formation rate (sSFR) (Brinchmann et al. 2004). In the right panel of Figure 4.1, the distributions of sSFRs and stellar masses of galaxies are shown. We define the $Log(sSFR) = -11$ as a separating
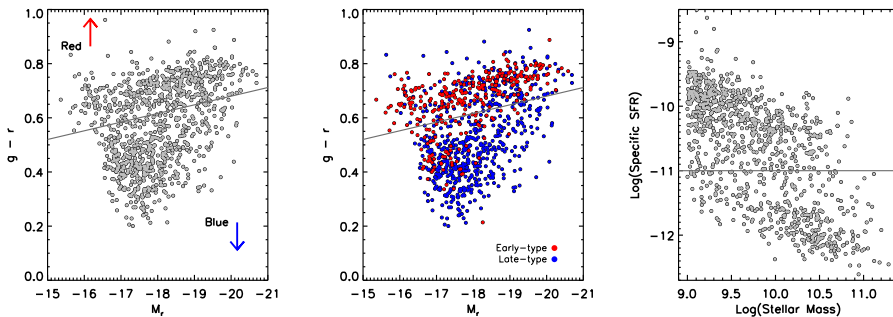
Figure 4.1 – *Left*: The color-magnitude diagram of our sample. The solid line shows the separating cut to define red and blue galaxies. *Middle*: The same as left panel but galaxies are color-coded according to their morphological classifications, i.e. Early-type galaxies as red points and Late-type galaxies as blue points. The morphological classification is based on the Galaxy Zoo Catalog (GZ1). *Right*: Distribution of galaxies specific star-formation rate (SSFR) as a function of their stellar mass; the solid line represents the separation cut at $\log(sSFR) = -11$.

cut to split our sample into star-forming and non star-forming ones. In summary, we divide our galaxies by four criteria: (1) Morphology based on Galaxy Zoo visual galaxy classifications (2) Color (3) Specific star formation rate (sSFR) (4) Sérsic indices (based on smoothed profiles of galaxies at low-z, see Appendix B).

We also need to take into account the effects of sample selections on the completeness. We follow S03 to apply volume corrections to our sample (V_{max} method). We give each galaxy a weight which is proportional to the inverse of the maximum volume out to which it can be observed. However, as our sample is limited to redshift ranges of $z = 0.01 - 0.02$, all galaxies have equal weights and hence our sample is not biased by stellar mass incompleteness down to $10^9 M_\odot$. It is worth noting that the fraction of galaxies which were not morphologically classified by Galaxy Zoo is ∼ 6% on average and hence the effects are negligible.

4.3 Sizes at $z = 0$

As mentioned earlier, the well-resolved profiles of some of nearby galaxies could exhibit non-Sérsic structures. Consequently, this raises questions about the effects of these structures on measurements of nearby galaxy sizes (i.e., half-light radii) with single-component, analytical models. In the following, we employ several methods to measure sizes of our $z = 0.01 - 0.02$ galaxies. These methods can be separated into two main categories: 'parametric' i.e., measuring the half-light radius of galaxies using best-fit two-dimensional analytical models and 'non-parametric' from their observed one-dimensional light profiles and measuring their total fluxes as described below.

4.3.1 Parametric Methods

To quantify the structural properties of galaxies with parametric methods, we use the GALFIT v3 modeling software (Peng et al. 2010). GALFIT measures the shape and size of each galaxy by finding a best-fit parametric model of its two-dimensional surface brightness profile. It generates a range of profile models which are convolved with the PSF of the galaxy image and determines the best-fit model by comparing models to galaxy light profile and minimizing the χ^2 of the fit. GALFIT can fit one or more analytical functions such as Sérsic (Sérsic 1963, Sersic 1968), de Vaucouleurs (de Vaucouleurs 1948), etc., to a galaxy light profile.

In the following we outline the procedure for using GALFIT and measuring galaxies structural parameters from Sérsic models. We first created a postage stamp for each galaxy from SDSS (*r-band*) imaging frames (2048×1448 pixels and pixel scale of 0.396″). The postage stamp should be large enough to contains enough background sky pixels. We initially set our postage stamps to have widths of at least 1800 pixels. However, as our galaxies have large apparent angular sizes and they might be located on different positions on SDSS frames, the postage stamp sizes varies a bit for each galaxy. Nevertheless, our defined box-size value creates a postage stamp for each galaxy $\gtrsim 10$ times larger than apparent galaxy sizes. These are sufficient for leaving the sky background as a free parameter during fitting procedure.

In order to detect and mask neighboring objects, we use SExtractor (Bertin & Arnouts 1996). For SDSS *r*-band images, we use the following SExtractor configuration parameters for detecting sources: $DETECT\_MINAREA = 10$, $DETECT\_THRESH = 1.5$ and $ANALYSIS\_THRESH = 1.5$ and $DEBLEND\_MINCONT = 0.095$. In addition, we further smoothed out the mask map created by SExtractor to reduce plausible bias of sky background estimations by contribution from undetected low flux regions around nearby sources. We also provide the initial parameters for GALFIT, such as half-light radius, magnitude, position angle and axis ratio derived from SExtractor and initially set the Sérsic index to value of 2.

The SDSS photo pipeline generates a synthesized PSF image at the central position of each galaxy using a published tool of Read Atlas Images [1]. We use this code and extracted PSF images in *r*-band SDSS for each galaxy, separately. The PSF images required by GALFIT to convolve model images during fitting procedure.

4.3.1.1 Single Component Sérsic Profiles

Our first adopted parametric model for describing the galaxies surface brightness is the one component Sérsic model. Single component Sérsic profiles are widely used for determining galaxy structures and properties, especially for high redshifts galaxies. The Sérsic function describes the surface brightness of a galaxy at radius r as

$$\Sigma(r) = \Sigma_e e^{-b_n[(r/r_e)^{1/n}-1]} \tag{4.2}$$

---

[1] `http://www.sdss.org/dr7/products/images/read_psf.html`

where r_e is the half-light radius and Σ_e is the surface brightness at r_e. The shape of the galaxy profile is determined by the Sérsic index n, and the value of b_n is coupled to n (see for more details in Graham & Driver 2005).

4.3.1.2 Two-Component Sérsic Profiles

Although the single Sérsic profile describes the surface brightness of galaxies over a large dynamic range remarkably well (e.g., Kormendy et al. 2009), the departure from the simple models can be used for diagnosing the formation of the galaxies. Specifically, nearby elliptical galaxies tend to show either 'extra light' or 'missing-light' in their central regions, depending on their luminosity and different empirical functions (e.g., "core-Sérsic" or "Nuker" law) have been used and suggested to parametrize these distinct components (Ferrarese et al. 1994, Lauer et al. 2007, 1995, Graham et al. 2003, Côté et al. 2006, Hopkins et al. 2009b). However, as our sample consists of wide ranges of luminosities and morphologies, we use double Sérsic profiles which allow a variety of possible inner and outer profiles for each object (see Turner et al. 2012). Our adopted multi-component model is described as:

$$\Sigma(r) = \Sigma_{e1} e^{-b_{n1}[(r/r_{e1})^{1/n1} - 1]} + \Sigma_{e2} e^{-b_{n2}[(r/r_{e2})^{1/n2} - 1]} \tag{4.3}$$

To compute effective radii, we first analytically reconstructed the sum of the deconvolved circularized surface brightness profiles of two components from the best-fit parameters and then computed their total fluxes and consequently their half-light radii.

4.3.2 Non-Parametric Method

We test the results from these analytical models against an independent non-parametric method. The non-parametric technique do not rely on the previous assumptions about the structure of galaxies. It benefits from the galaxy observed curve of growth. In brief, the observed intensity profile of a typical galaxy is measured through elliptical isophotal fitting and from that, the growth curve of galaxy fluxes is determined. This provides the radius at which the flux reaches to half of the total value.

In details, in order to measure the half-light radius of galaxies from this method, we need to integrate the fluxes of galaxies at different radii and find the radius at which the flux reaches half their values. For this purpose, we first extract the observed surface brightness profile of galaxies using the IRAF task ELLIPSE (Jedrzejewski 1987). This procedure measures fluxes in isophotal ellipses over the galaxy image and therefore can make it possible to generate one-dimensional surface brightness profile of a galaxy.

The accuracy of this method depends on the precise measurements of galaxies total fluxes. Therefore we measure the fluxes out to ~ 400 arcsec from the galaxies center. However, the surface brightness of galaxies is low at the outer parts and hence it is very difficult to define the exact edges of galaxies. Therefore, for measuring the fluxes in the outer parts, we extrapolate the total light of galaxies beyond their *petroR*90 radius (i.e., a radius containing 90% of the *petrosian* flux derived from SDSS DR7). This is done

by fitting one-dimensional Sérsic profiles to these outer regions. By integrating the light profiles estimated from our best-fit models to infinity, the total fluxes in the outer regions are estimated. Moreover, in this way, we also estimate the sky background for each galaxy as sky value is left as a free parameter during the fitting procedure. Then for each galaxy, we integrate fluxes at different radii up to radius smaller than *petroR*90 from the fluxes measured by ellipse fitting and add them to the fluxes estimated in the outer region. This gives the total fluxes of galaxies and hence leading to extract the radii at which contains half of the total fluxes, i.e., their non-parametric half-light radii. We note that for about less than 7% of the galaxies, the one dimensional fitting to the outer parts using *petroR*90 are not converged. Hence we used *petroR*50 which is radius contains 50% of the flux within *petrosian* magnitude. In order to check if the results depend on the choice of radius for the rest of the sample, we repeated the procedure by fitting the outer parts of galaxies starting at smaller radii of i.e., *petroR*50. The results were perfectly consistent for all galaxies. We note that we fixed the ellipticity (*E*) and the position angle (*P.A.*) of the ellipse isophotes to the values obtained from the best-fit of single Sérsic parametric method.

The sizes derived from non-parametric method are also needed to be corrected for point spread function (PSF) broadening and therefore we use the following relation according: $R = \sqrt{(r_{1/2})^2 - (r_{PSF})^2}$, where $r_{1/2}$ and r_{PSF} are the derived non-parametric half-light and PSF size, respectively. This correction is only important for very small galaxies ($\lesssim 1$ kpc). It is also worth noting that that all sizes derived in this paper are circularized, using $\sqrt{ab}$, in which *a* is the semimajor axis and *b/a* is the axis ratio. This removes the effects of ellipticity (e.g., Trujillo et al. 2006b, Franx et al. 2008, Williams et al. 2010).

4.3.3   Simulations *(I) & (II)*

We perform simulations for testing our methods and procedures as follows. The first one is designed to test the reliability of the single component Sérsic method and the non-parametric method for galaxies at *z* = 0. For that, we first generated single Sérsic mock galaxies with random properties (magnitude, re, b/a) in similar range of values for real galaxies. We then add them into the empty regions of the *r*-band SDSS images and perform our fits, using single Sérsic profiles and the non-parametric method. The results are shown in Figure 4.2. In the left panel, the comparison between input and output sizes are shown using parametric method and the Sérsic indices are compared in the middle panel. The output sizes derived by using the non-parametric method are also compared to their original sizes in the right panel of Figure 4.2. The sizes of galaxies can be recovered without any systematics with median differences less than 2% for both methods. There are also no systematic errors in the recovery of Sérsic indices. This shows that for mock galaxies with single Sérsic profiles, our procedure are robust in recovery of their properties from SDSS images.

As shown in Appendix A (Figure 4.10), sizes of galaxies derived using single Sérsic profile fitting can be biased, especially for massive early-type galaxies. This may be caused by the existence of additional component(s) or non-Sérsic light profiles. We
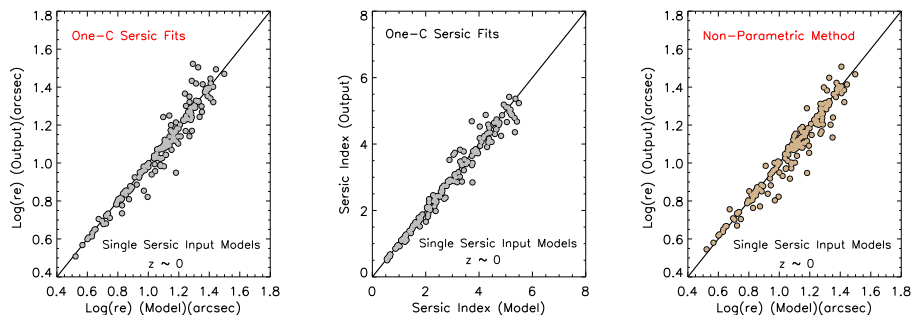
Figure 4.2 – *Simulation (I)*: The comparison between sizes of simulated galaxies (models with 'single' Sérsic profiles) and their recovered sizes (using single Sérsic component fittings in left panel and using Non-parametric method in right panel) and Sérsic indices (middle panel) after adding them into empty regions of SDSS *r*-band images. As plots show, there is no systematics in recovery of parameters of single Sérsic model galaxies for both methods.

have also shown that sizes derived with double Sérsic component, are smaller that sizes from one component models. We test an idealized case using simulated two-component objects. For that, we first created a sample of 300 two-component Sérsic galaxies such that each model galaxy has a central component with median half-light radius of ∼ 1 kpc and the outer component with median size of ∼ 3 kpc. We also assumed that the central components have larger median Sérsic indices than the outer-part components. For all galaxies, the central components are ∼ 0.6 magnitude fainter than the other one. These numbers are derived from the average results of the two-component fits to our real galaxies at $z = 0.01 - 0.02$. To ensure that we are testing only the effects of multi component galaxies, only the sky background levels are added to the images of these model galaxies without any additional noise or neighbouring objects. We then measure sizes of these two-component model objects using single Sérsic profile fitting and the non-parametric method. The results are shown in Figure 4.3. As seen in the left panel, the sizes are recovered robustly with the non-parametric method. However, as shown in the right panel of Figure 4.3, sizes from single Sérsic fitting are biased (larger) compared to their input half-light radii, especially for large objects. This simplified test shows that sizes from single Sérsic profile fitting can be biased for true two-component galaxies. Meert et al. (2012) use different assumptions for simulated SDSS galaxies and show the existence of bias in recovered parameters by fitting a single Sérsic profile to real two-component systems. Although our sample are quite nearby (∼ 45 − 85 Mpc), Bernardi et al. (2012) show the same effect for the main SDSS sample at $z \sim 0.1$. Hence, using single Sérsic sizes for local galaxies can introduce systematics in size analyses.

Nevertheless, fitting correct models to nearby galaxies is complicated. Different authors use different models to fit multi-component galaxies, e.g., traditional deVaucouleurs plus Exponential disk, Sérsic +Exponential (Meert et al. 2012), double Sérsic or even using multiple (3-4) Sérsic profiles (Huang et al. 2012). It is also the case that not all of
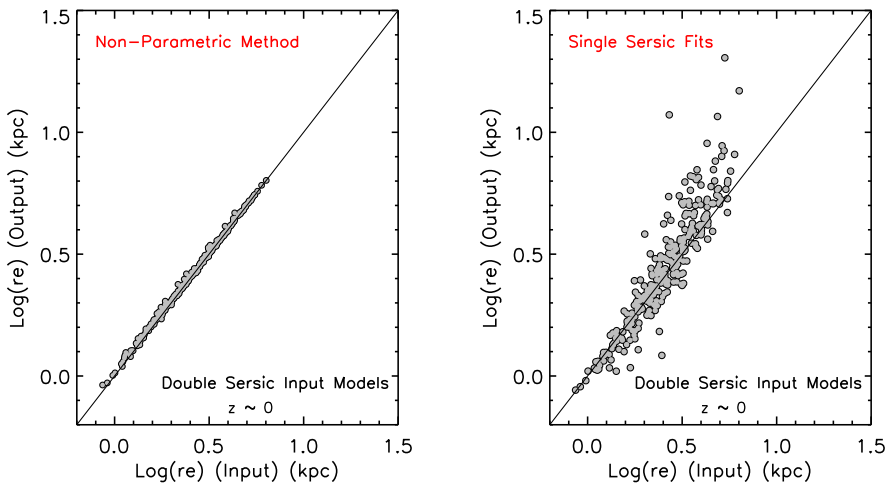
Figure 4.3 – *Simulation (II)*: The comparison between sizes (i.e., half-light radii) of simulated galaxies (models with 'double' Sérsic profiles) and their recovered sizes using single Sérsic component fittings (right panel) and non-parametric method (left panel). This shows that sizes derived from single Sérsic profile fitting are biased for true nearby two-component Sérsic profile objects. We note that this simulation does not include noise, in order isolate the biases caused by intrinsically complex structures.

the galaxies (at wide ranges of stellar masses) need to be measured by multi-component models ($\sim$ 77% are robustly fit with two-component models in this work). Therefore, for the rest of this study, we use our non-parametric sizes for these $z \sim 0$ galaxies. Our simulations (*I & II*) demonstrate the robustness of our non-parametric method. In addition, due to the large angular sizes of our galaxies, the effects of the PSF on sizes from this method are negligible.

It is worth nothing that fluxes used for estimating the stellar masses of SDSS galaxies are model dependent and hence these fluxes can be different from fluxes measured through the non-parametric method for each individual galaxy. Therefore, it is essential to correct the stellar masses according to the new flux measurements. We rescale the stellar mass of each galaxy by measuring the ratio between its non-parametric flux and the one used for estimating its stellar mass from the MPA catalog.

4.4 Stellar Mass-Size Relation At $z = 0$

The stellar mass-size relation for the SDSS galaxies has been studied by S03. They investigated this relation for objects which are defined as early and late types according to their Sérsic and concentration indices, and their relations have been widely used in literature. However, it is argued that the half-light sizes used in S03, which are from the NYU-VAGC catalog and based on one-dimensional (1D) single Sérsic fitting, could have been underestimated (e.g., Guo et al. 2009, Simard et al. 2011). We have also shown that using single Sérsic fitting could bias the sizes of galaxies with high stellar masses. As the mass-size relation could depend on the fitting model employed (specifically at high-mass ends), our independent non-parametric method for $z = 0$ galaxies, should remove uncertainties due to model assumptions. Our sample consists of galaxies over a wide range of stellar mass ($\gtrsim 10^9 M_\odot$) and is suitable for investigating this relation.

We first study the mass-size relation of our sub-samples based on morphological Galaxy Zoo classifications. The distribution of sizes versus stellar masses of late-type and early-type galaxies are illustrated in the top row of Figure 4.4. The median sizes in small bins of stellar masses for each sample are measured (blue and red circles), and it can be seen that sizes of both late-types and early-types show little or weak correlation with to mass up to $\sim 3 - 4 \times 10^{10} M_\odot$; however the relation steepens beyond this stellar mass and is stronger for the early-type galaxies. For both types of galaxies, the relations seem to begin above specific stellar masses.

To further quantify the correlations, we use the functional form employed for late-type galaxies in S03 (equation 18) for both our late-type and early-type samples:

$$R_{kpc} = \gamma (M_*/M_\odot)^\alpha (1 + M_*/M_0)^{\beta - \alpha} \qquad (4.4)$$

Where, α, β, γ and M_0 are free fitting parameters. This basically allows the relation to have two different slopes depending on the stellar mass range. The α and β represent the slopes of the relation and the characteristic mass, M_0 determine the stellar mass at which the slope of the relation changes. However, this relation is not very sensitive to the
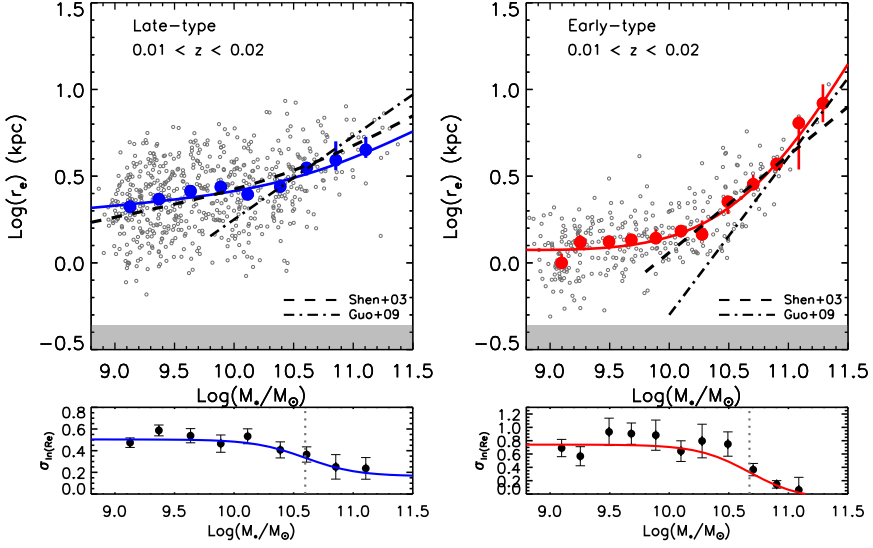
Figure 4.4 – *Top row*: The stellar mass-size relation of late-type galaxies (left panel), and early-type galaxies (right panel). The individual galaxies are shown as small open gray circles and the blue and red filled circles are the median of the sizes in stellar mass bins. The solid blue and red lines are the best fits to the data. The mass-size relation from studies of Shen et al. (2003) and Guo et al. (2009) are also illustrated by dashed and dot-dashed lines, respectively. The best-fit relations are consistent with Shen et al. (2003), however, for early-type galaxies the relation flattens below $M \lesssim \sim 4 \times 10^{10} M_\odot$. The shaded gray regions show the physical sizes of PSFs in SDSS r-band images. *Bottom row*: The size dispersions as a function of stellar masses and their best-fits. The characteristic stellar masses, where the dispersions change significantly, are shown as vertical dotted lines.

characteristic mass, M_0, therefore, this can be defined from the size dispersion relation as follows (equation 19 in S03):

$$\sigma_{lnR} = \sigma_2 + \frac{(\sigma_1 - \sigma_2)}{1 + (M_*/M_0)^2} \tag{4.5}$$

where σ_1 and σ_2 are also free fitting parameters (representing size dispersions at low and high masses) and M_0 is the characteristic stellar mass at which σ_{lnR} significantly changes. Size dispersions as a function of stellar mass for late-type and early-type galaxies are shown in bottom panels of Figure 4.4 (left and right panels, respectively). The best fits to the data points are shown as solid blue and red lines and the best-fit parameters are presented in Table 4.1.

For late-type galaxies, the median size dispersions decrease at stellar mass greater than $\sim 4 \times 10^{10} M_\odot$ consistent with S03. The mass-size relation for these galaxies are also con-
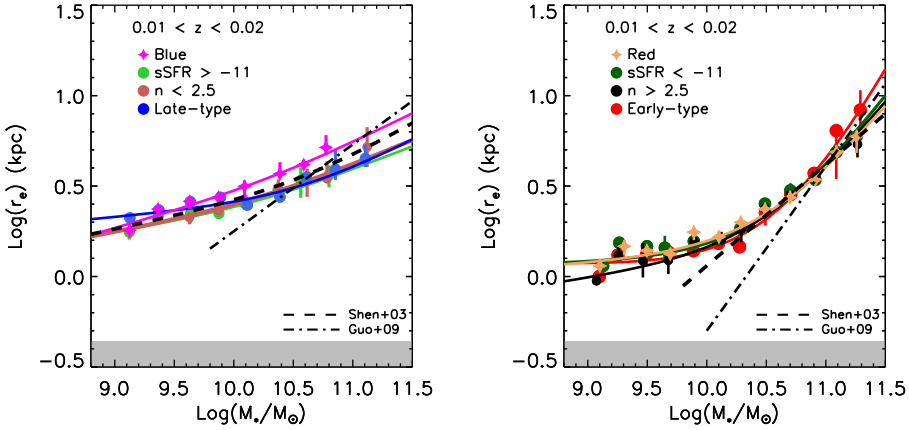
Figure 4.5 – The stellar mass-size relation of galaxies classified by means of different criteria. In the right panel, blue, late-type (visually classified), star-forming galaxies, and low-Sérsic index ($n < 2.5$) are compared and in the left panel red, early-type (visually classified), non star-forming, and $n > 2.5$ are compared. The stellar mass-size relation from studies of Shen et al. (2003) and Guo et al. (2009) are also illustrated by dashed and dot-dashed lines respectively. The points are the median size dispersions as a function of stellar mass and the lines represent the best-fits to these points. As this plot shows, the relation based on different methods of classification of galaxies are largely consistent, though blue galaxies lie above the other relations.

sistent with S03 (dashed line). The size dispersions for early-types also behave similarly and decrease for massive galaxies above a characteristic mass around $4 \times 10^{10} M_{\odot}$. However, due to low number of objects at these high mass bins, it is not clear how significant this effect is.

The median sizes of early-type galaxies at a stellar mass range of $\log(M_*/M_{\odot}) \sim 10 - 11$ are consistent with the S03 relation. However, at lower stellar masses ($\lesssim 2 \times 10^{10} M_{\odot}$), sizes are almost constant. Therefore, in this mass range, there is little or weak correlation between stellar mass and size. For late-type galaxies the relation runs parallel at these masses but with larger sizes. The mass-size relations for galaxies with higher stellar masses (i.e., $\gtrsim 2 \times 10^{10} M_{\odot}$) are steep for both late and early types. However, each sample exhibit different slopes and early-types have a steeper mass-size relation (see Table 4.1).

We also present the mass-size relations of galaxies based on different sample definitions such as color, Sérsic indices and sSFR in Figure 4.5 in order to test the effects of these selections on the mass-size relation and defining baselines for future studies based on different sample classifications. Interestingly, the mass-size relations based on these classifications are consistent to the analogous relations in Figure 4.4. In the left panel of Figure 4.5, late-type galaxies are compared to the star-forming, blue and low Sérsic index galaxies. They are almost consistent, though the blue galaxies have larger sizes

at stellar masses $\gtrsim 10^{10} M_\odot$ compared to the others. This could be caused by excluding edge-on galaxies using the color criterion. We should note that the Sérsic indices are measured from the degraded and smoothed SDSS images of galaxies (See Appendix B, Figure 4.15), hence removing biases from sub-structure. Nevertheless, it is interesting that the mass-size relation obtained for objects with Sérsic indices of $n < 2.5$ are consistent with S03. The best fits to the mass-size relation are summarized in Table 4.1.

The right panel of Figure 4.5 illustrates the comparison between the mass-size relation of early-type galaxies and those with red colors, low sSFR and high Sérsic indices. The relations are also consistent with each other. For all samples, the relations are curved with a weak relation for galaxies below $4 \times 10^{10} M_\odot$. The slopes of the mass-size relations at high mass ends (β) for these red/quiescent/$n > 2.5$ galaxies are on average around ~ 0.85, close to the slope of early-type central galaxies in Guo et al. (2009). However, this slope is slightly larger for early-type galaxies.

In general, we show that the stellar mass-size relations for both late and early type galaxies are curved with a steeper slope at higher stellar masses. The size dispersions bellow the characteristic masses are high but decrease above M_0. This is the case for all our studied samples. The stellar mass-size relations based on different definitions, such as color, sSFR, morphology are consistent with the scaling relations of late and early type galaxies.

4.5 Redshifting Galaxies to $z = 1$

In order to check whether cosmological effects and observational uncertainties could affect size (and structural parameter) measurements of galaxies at high redshifts, we perform redshifting simulations of the low-z object. We use our sample of galaxies from SDSS at $z \sim 0$ to create artificially redshifted samples of galaxies resembling the same galaxies at $z = 1$ in HST WFC3 images. Our redshifting procedure is similar to the method described by Barden et al. (2008) (FERENGI code) and we briefly describe it bellow. However, in order to take into account the effects of bandpass shifting, we only use SDSS r-band images as input and using WFC3- J_{125} images from CANDELS DEEP DATA (Bouwens et al. 2012) as output images instead of using the k-correction method described in Barden et al. (2008). WFC3 is the new near-IR instrument on board of HST and covering rest-frame optical wavelengths at $z \sim 1 - 3$. Hence it is suitable for this purpose.

4.5.1 Method

The first step in the redshifting procedure is to rebin the low-z images with pixel scale p_i and redshift z_i to output images at redshift of z_o (= 1 in this work) and pixel scale of p_o by a factor of β as:

$$\beta = (\frac{D_i}{D_o})(\frac{p_i}{p_o}) \tag{4.6}$$

Table 4.1 – The fitting results of the parameters in the Size-Mass relations.

Sample	α	β	$\log(\gamma)$	M_0	σ_1	σ_2
Early-type	-0.02 ± 0.07	1.25 ± 0.21	0.24 ± 0.73	10.67 ± 0.20	0.74 ± 0.07	-0.08 ± 0.24
Red	0.04 ± 0.05	0.80 ± 0.12	-0.31 ± 0.47	10.53 ± 0.13	0.75 ± 0.09	0.13 ± 0.07
$Log(SSFR) < -11$	0.01 ± 0.06	0.91 ± 0.16	-0.05 ± 0.65	10.55 ± 0.10	0.86 ± 0.11	0.13 ± 0.08
Sérsic > 2.5	0.09 ± 0.09	0.83 ± 0.21	-0.86 ± 0.90	10.53 ± 0.16	0.75 ± 0.15	0.14 ± 0.09
Late-type	0.06 ± 0.06	0.35 ± 0.18	-0.20 ± 0.55	10.60 ± 0.23	0.50 ± 0.04	0.16 ± 0.10
Blue	0.18 ± 0.08	0.33 ± 0.16	-1.40 ± 0.75	10.32 ± 0.30	0.57 ± 0.05	0.05 ± 0.12
$log(SSFR) > -11$	0.10 ± 0.09	0.26 ± 0.19	-0.74 ± 0.83	10.20 ± 0.21	0.66 ± 0.05	0.23 ± 0.10
Sérsic < 2.5	0.12 ± 0.08	0.27 ± 0.16	-0.87 ± 0.75	10.22 ± 0.23	0.67 ± 0.05	0.24 ± 0.09

Note. The best-fit parameters for the stellar mass-size relation for different types of galaxies at $z \sim 0$ (equation 4.4 and 4.5).

where D is the angular diameter distance, expressed as $D = \frac{d}{(1+z)^2}$, and d is the luminosity distance.

The next step is to apply cosmological surface brightness dimming at the rate of $(1 + z)^{-4}$ in each rebinned pixel. By considering the fact that the absolute magnitude of galaxies must be conserved, the total fluxes f of the input and output images must scale as:

$$\left(\frac{f_o}{f_i}\right) = \left(\frac{d_i}{d_o}\right)^2 \tag{4.7}$$

We note that it has been shown by several studies (e.g., Barden et al. 2005, Labbé et al. 2003) that the intrinsic surface brightness of galaxies increases with redshift. Therefore, during our procedure of artificially redshifting our galaxies, we incorporate the surface brightness evolution and making the galaxies one magnitude brighter at $z = 1$ following this equation $M_{evo} = xz + M$ and setting $x = -1$ (Barden et al. 2008).

It is important to reach the same resolution of the real data at high-z. Therefore, the next step is to correct the images to the appropriate PSF. This can be done by finding suitable kernels for convolving low-z images to reach the same PSF properties/shape at high-z. To do this, for each galaxy we require two PSFs, i.e., its low-z and high-z PSFs. We use low-z PSFs from SDSS (the ones we used for measuring sizes at $z \sim 0$) and for high-z, the median-stacked PSF which made from non-saturated stars in the J_{125} WFC3 images. Then, by transformation of PSFs into Fourier space, finding their ratio and transforming the results back into spatial domain, we can find the convolution kernels required to reach the WFC3's J_{125} band PSF. Note that we calculate separately a transformation function for each galaxy as the kernel depends on the input and output redshifts.

After transforming images to the high-z resolution an pixel scale, the last step is to add background noise to the images. For this, we put galaxy images into random empty regions of the J_{125} band CANDELS DEEP images and then measure their structural parameters as described below. We note that, in order to check the effects of sky variations on galaxy property measurements, we repeated this step by inserting each redshifted galaxy into multiple empty regions. The final measured size/parameter for each object is the median of these seven realizations.

The procedure to measure the structural properties of artificially redshifted galaxies (i.e., size and Sérsic index) is similar to that used in Mosleh et al. (2012). In brief, we used GALFIT to find the best-fit single Sérsic model for each galaxy. Neighbouring objects are detected by running SExtractor and masked during profile fitting. Initial parameter guesses, such as magnitude, half-light radius and axis ratio are provided from the SExtractor output. We used the median-stacked PSF from stars in the field. In Figure 4.6, we show the SDSS postage stamp images of the galaxies (late-types in the left set of panels and early-types in the right set of panels) at low-z (the left columns) and after redshifting to $z = 1$ (middle columns). The best-fit single Sérsic models of these artificially redshifted galaxies at high-z are shown in the right columns.

We perform two sets of simulations to test the size measurement accuracy in the J_{125} WFC3 images, and to check the procedure for artificially redshifting the galaxies. These
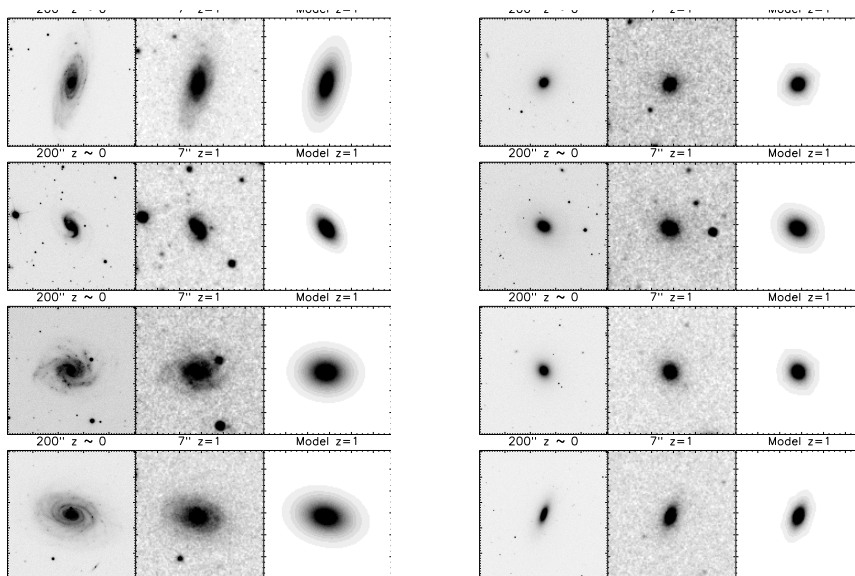
Figure 4.6 – Example images of four spiral galaxies (left set of panels) and four elliptical galaxies (right set of panels). In each set, the left panels show the SDSS (*r-band*) postage stamp images ($200'' \times 200''$) of galaxies at $0.01 < z < 0.015$ and in the middle columns, we show their artificially redshifted (to $z = 1$) postage stamp ($7'' \times 7''$) images after adding to WFC3-J_{125} images and in the right columns represent the best fit single Sérsic models of these redshifted galaxies.

tests are described in Appendix B. We show that our redshifting method and size measurements at high-z are robust and can recover sizes and structural parameters of model galaxies without any systematics.

However, as mentioned earlier, using single Sérsic profile fitting for more complex galaxies in the nearby Universe potentially biases size estimates. This fact raises concerns about the sizes of galaxies at high redshifts derived from single Sérsic fitting. Therefore, it is also worth checking whether single Sérsic profile fitting biases sizes of two-component objects at high redshifts. For that, we use the same simulated two-component model galaxies in section 4.3.3 (simulation (II), Figure 4.3) and redshift them to $z = 1$. We measured their sizes after redshifting with single Sérsic models. The results are shown in Figure 4.7. This shows that single Sérsic profile fits of two-component galaxies at $z = 1$ provide reliable sizes, likely due to the smaller structures being washed out at high redshift. Therefore, traditional single Sérsic surface brightness fitting robustly recovers sizes of our redshifted galaxies.
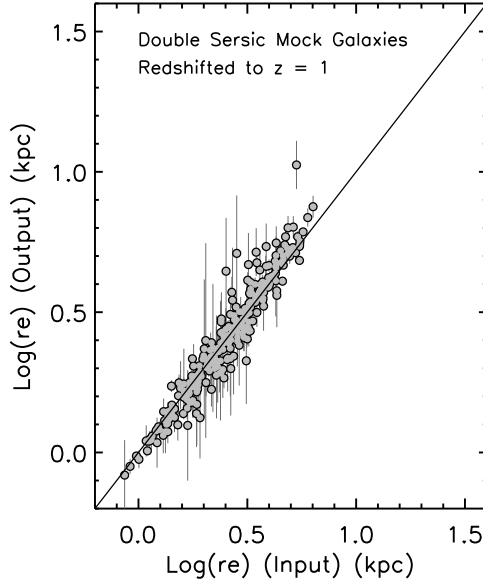
Figure 4.7 – Sizes of simulated two-component $z \sim 0$ galaxies which have been "redshifted" to $z = 1$ and remeasured with single-component Sérsic profile fitting. The input and output sizes are consistent, indicating that sizes of multi-component galaxies can be reliably derived with single-component Sérsic models at higher redshifts.

4.5.2 Comparing to Sizes at $z = 0$

In previous sections, we described how the sizes of our sample are measured reliably at both $z \sim 0$ and $z = 1$. In this section, we compare sizes of galaxies before and after redshifting to $z = 1$. The comparison between low-z and high-z sizes for all galaxies are shown in left upper panel of Figure 4.8 and their median relative differences in small bins of sizes are shown in the left bottom panel. As can be seen, sizes before and after redshifting agree well and there are no systematics.

There are also no biases if we split the sample into blue and red galaxies. Although the random scatter increases with size for red objects, there are no systematics, and on average sizes of these galaxies can be reliably recovered at high redshift. As mentioned in section 4.5.1, to check the effects of the sky background on properties of galaxies at $z = 1$, we perform different realizations by inserting the galaxies into different random blank sky regions and remeasure their properties. The galaxy parameters at $z = 1$ are the median values of these repeated measurements and the error bars illustrate the 1σ scatter. Galaxies are also color-coded according to their stellar masses.

The results are the same using different galaxy classifications. For instance, in Figure
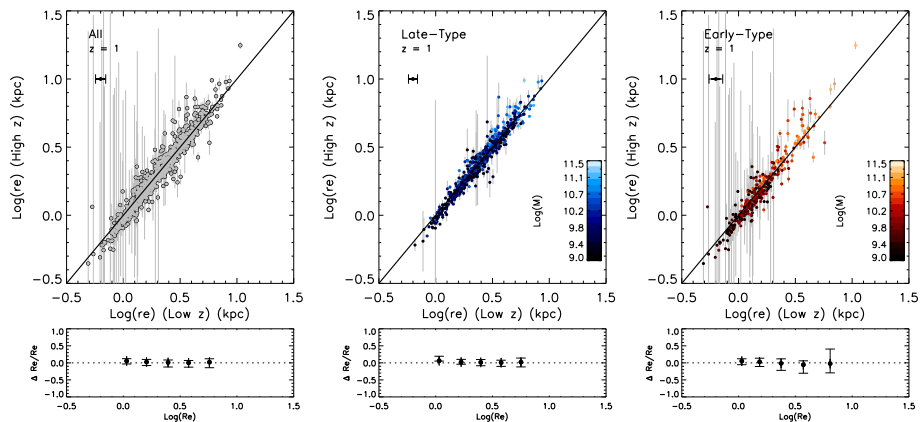
Figure 4.8 – A comparison between sizes of galaxies at low redshift to their sizes measured after artificially redshifting to $z = 1$ for all galaxies (left panel), late-type galaxies (middle panel), and early-type galaxies (right panel). The errors are the standard deviation of their sizes measured at different positions (different realizations). Sizes of galaxies are recovered after redshifting without any systematics.

4.8, the size comparison is shown for late-type (middle panel) and early-type galaxies (right panel). Although the scatter increases for large and massive early-type galaxies, there is not any systematic differences in their sizes.

It is worth noting that for sizes at $z = 0$, we used non-parametric method and for galaxies at $z = 1$ single Sérsic profile fitting is used. Using single Sérsic profile fitting at $z \sim 0$ brings systematics when comparing sizes before and after redshifting (e.g, Weinzirl et al. 2011). This is also the case for comparing Sérsic indices, which tend to be overestimated at $z \sim 0$ using single Sérsic profile fitting.

The fact that sizes of multi-component galaxies at $z = 1$ can be recovered robustly using single Sérsic fitting can be explained by the resolution limit of images at high redshifts. The differences are mostly noticeable for massive early-type galaxies. The bright centers of elliptical galaxies have typical sizes of $\lesssim 1$ kpc (e.g., Huang et al. 2012, Hopkins et al. 2009b,a) which is about the typical size of PSF FWHM of WFC3 images (~ 1.2kpc) at $z = 1$. As a result, the inner components are smeared out and the galaxy profiles are dominated by the outer components. Therefore, using single Sérsic fitting at this redshift and resolution robustly recovers the true parameters (See Appendix B for additional tests which illustrate how degrading the resolution affects measured structural parameters of local galaxies).

We have also checked whether the results after redshifting are sensitive to the signal-to-noise (S/N) of images. This has been tested by changing the S/N, either by adding noise to the SDSS r-band images before redshifting them or arbitrarily increasing the S/N of redshifted objects. These tests did not show any systematic changes in the size of red-
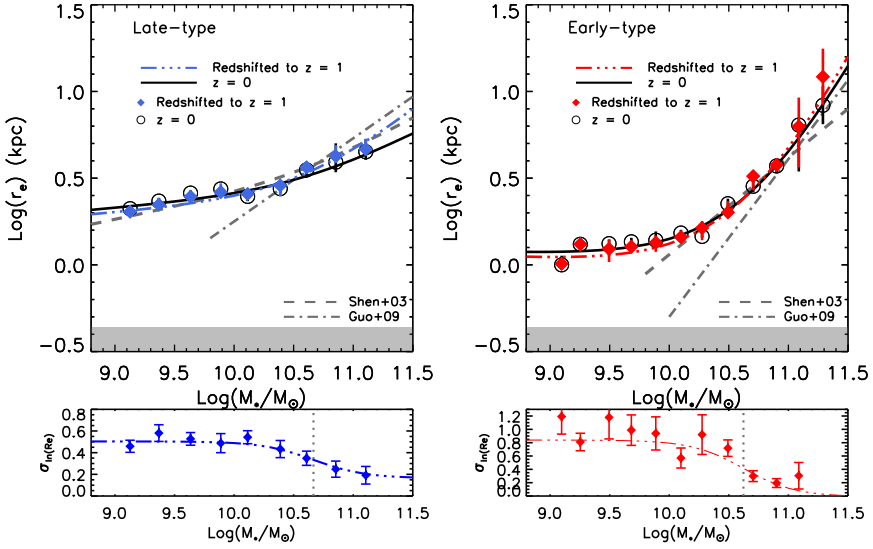
Figure 4.9 – The stellar mass-size relations and size dispersions of late-type (left panels) and early-type (right panels) galaxies are compared before and after artificially redshifting to $z = 1$. The blue and red points are the the median sizes of galaxies in mass bins and the dashed-three dotted lines are their best fits. The mass-size relations are consistent with the relations at $z = 0$ (open circles and solid lines). This further demonstrates that size-mass relations of galaxies are reliable at $z = 1$ using single Sérsic profile fitting.

shifted objects. Therefore, in general, sizes of galaxies at high redshift can be measured robustly using canonical single Sérsic profile fitting as long as the physical resolution is not better than ~ 1 kpc.

4.5.3 Stellar Mass-Size Relation after Redshifting

It would now be interesting to examine how the stellar mass-size relations look like after redshifting to $z = 1$. In Figure 4.9, comparison of the mass-size relations before and after redshifting to $z = 1$ are illustrated. The relations for late-type galaxies are shown in the left panel, where the solid blue diamonds are the median sizes after redshifting in small mass bins and the dashed-three-dotted line is the best-fit to the data. The open circles are the median sizes at $z = 0$ along with the solid black line as a best-fit (same as in Figure 4.4). The size dispersions after redshifting also shown in the bottom left panel. The relations for early-type galaxies are shown in the right panel. As can be seen, the mass-size relations are consistent to their $z = 0$ after redshifting. The poor constraints at the high stellar mass end are due to small number statistics; however, the results are consistent

within uncertainties. This Figure shows that the stellar mass-size relations based on the single Sérsic profile fitting at high redshifts are robust. Using different definitions for separating galaxies would result the same after redshifting. In Figure 4.9, we only present the relations for morphologically selected sample.

4.6 Discussion

In this paper, we use a sample of about 1000 galaxies at $0.01 < z < 0.02$ from SDSS DR7 to study their sizes and stellar mass-size relations. We first investigate the robustness of size measurement methods for these nearby galaxies, using two main procedures for determining sizes and structures: parametric methods (single and double component Sérsic profile fittings) and a non-parametric method. In agreement with recent works (e.g., Allen et al. 2006, Bernardi et al. 2012, Meert et al. 2012, Huang et al. 2012), the majority of galaxies in the nearby Universe are well fit with two component profiles. Comparing the sizes from the non-parametric method (and from double Sérsic fits) to those from single Sérsic fits shows the systematic overestimation of sizes from the single Sérsic method. In particular, sizes and Sérsic indices of early-type galaxies at the high stellar mass end tend to be overestimated using the single Sérsic fitting approach. Non-Sérsic profiles or substructures in nearby galaxies may to be the cause of this bias. We tested this by simulating two-component model galaxies and measuring their sizes using single Sérsic fitting and reached the same conclusion. Using single Sérsic profile fitting also overestimates the Sérsic indices of these galaxies. Therefore, we caution that relying on single Sérsic fits can introduce biases for nearby, well-resolved galaxies.

Stellar mass-size relations of $z = 0$ galaxies from surveys like SDSS are often used as baselines for quantifying the evolution of higher-redshift galaxy sizes. Using the non-parametric method and classifying our sample thorough a number of frequently-employed criteria (size, color, morphology, and Sérsic index), we have explored the stellar mass-size relation of galaxies in the nearby universe down to a stellar mass of $10^9 M_\odot$. We show that the slope of the relation varies with mass for both late-type and early-type galaxies. The relations flatten for galaxies below about $3 - 4 \times 10^{10} M_\odot$ (see also Figure 11 in Turner et al. 2012). Moreover, at these low stellar masses, the relations for both late-types and early-types run parallel but with smaller sizes for early-type objects. Above a characteristic stellar mass of $\sim 3 - 4 \times 10^{10} M_\odot$, the mass-size scaling relations get steeper with less scatter for both late- and early-types. However, the early-types have a significantly steeper relation than late-types.

In S03, the mass-size relation for early-types is reported down to stellar a mass of $\sim 10^{10} M_\odot$. They indicated that faint ellipticals were missed in the analysis due to their type classifications based on concentrations and Sérsic indices. However, they report tentative evidence that the size-luminosity relation for faint red galaxies flattens at low masses. Graham & Worley (2008) showed that the size-luminosity relation of elliptical galaxies has a varying slope. Janz & Lisker (2008) also showed a different size luminosity relation for dwarf and giant early-type galaxies in the Virgo Cluster and illustrated that the relation has little to no dependence on luminosity on the faint end. Bernardi et al.

(2012) also pointed out the flattening of the early-type mass-size relation, in agreement with what we see in the right panel of Figure 4.4. With our low-z sample reaching $10^9 M_\odot$, the flattening of the relation at low masses is clearly seen.

At the high stellar mass end ($\gtrsim 10^{11} M_\odot$), we find that the sizes of the early-type galaxies tend to be slightly larger than the S03 relation. Guo et al. (2009) also found a similar trend for early-type central galaxies (dashed-dotted lines in Figure 4.4). We note that the early-types in our sample are morphologically selected and differ from the early-types in S03 (defined as $n > 2.5$). In addition, as mentioned earlier, sizes of high Sérsic index galaxies maybe underestimated in NYU-VAGC. The number of our early-type galaxies in this stellar mass bin is low and provides only weak constraints. However, Bernardi et al. (2012) also show similar behaviour at this high-mass end. They note that the increase in the steepness of the mass-size relation for high-mass early-types could be due to BCGs (see also Bernardi 2009, Bernardi et al. 2007). They also pointed out that the steepness of the relation for early-types changes at these high stellar masses.

However, it is still not clear how the massive early-type galaxies are connected to low mass ones (i.e., $\lesssim 10^{10} M_\odot$) and how the curvature of the mass-size relation arises for these galaxies. Graham & Worley (2008) argued that the curved size-luminosity relation for elliptical galaxies is expected from the assumption of varying profile shapes of these galaxies with luminosity and they are not distinct types. However, Janz & Lisker (2008) find evidence for the different behaviour of faint and bright early-types (see also Toloba et al. 2012). Bernardi et al. (2012) also pointed out that the curvature of the early-type scaling relations might arise from the presence of other components (e.g., a disk) with the bulges of these galaxies. On the other hand, the characteristic stellar masses mentioned above are predicted by semi-analytical simulations for spheroids in Shankar et al. (2013). They show that the physical processes behind the evolution of spheroid sizes are different below and above these masses, which might naturally explain the differing relations.

For late-type galaxies, we find that the stellar mass-size relation is mostly consistent among our samples regardless of the exact definition. These relations are also consistent with the mass-size relation for late-types in S03. However, the mass-size relation for blue galaxies is somewhat offset to larger sizes and steeper than that derived for other "late-type" classifications. This is likely a consequence of the strong color-size relation pointed out by Franx et al. (2008), as well as the exclusion of red, edge-on spirals from the blue sample. The size-mass relationship among the "early-type" samples appears to be consistent regardless of the exact classification method used (elliptical, red, $n > 2.5$ and/or quiescent).

Finally, we artificially redshifted our sample to resemble $z = 1$ galaxies in WFC3 J_{125} band images and test the robustness of size and structural measurements at high redshifts. We remeasure sizes of galaxies with single Sérsic profile fitting, a common method in the literature for high redshift galaxies. Our results show that using single Sérsic profile fitting recovers the sizes of these redshifted galaxies without any systematics. Interestingly, this demonstrates that size measurements at high-z are robust, despite the single-Sérsic models failing for nearby massive early-types. We further verified this with simulations, finding that once the small components of nearby two-component galaxies are smeared out at high z, single Sérsic component fitting can adequately measure structural param-

eters. Image resolution is thus an important criterion for deciding whether to use single Sérsic profiles. At a physical resolution $\lesssim$ 1 kpc, where central bright components are well-resolved, overly simple models like single Sérsic profiles can introduce biases, and a multi-component or non-parametric method should be used.

4.7 Summary

We present the mass-size relation of a sample of nearby galaxies at $z = 0.01 - 0.02$, dividing the sample based on several common classifications. We examined different methods of size measurements in order to quantify the systematics associated in each method. We also artificially redshifted these galaxies to $z = 1$ to test potential systematic effects on their size measurements at high redshifts. From our results we find that:

- Nearby early-type galaxies with masses $\gtrsim 2 \times 10^{10} M_\odot$ are not well fit with single Sérsic profiles. Two component fits and non-parametric methods appear to provide less-biased measurements. These methods give effective radii which are smaller than those measured with single Sérsic fits.

- The stellar mass-size relation of both late-type and early-type galaxies are steep at high masses ($\sim 3 - 4 \times 10^{10} M_\odot$) and flatten at low masses.

- Although single-Sérsic profile fits can be biased for nearby, well-resolved galaxies, they provide robust sizes at high redshifts.

- The stellar mass-size relations of "spiral" and "elliptical" galaxies are not particularly sensitive to the precise definition of these categories (color, Sérsic index, morphology, sSFR), with the exception of blue galaxies which follow a somewhat higher and steeper relation.

4.8 Acknowledgments

Western Reserve University, University of Chicago, Drexel University, Fermilab, the Institute for Advanced Study, the Japan Participation Group, Johns Hopkins University, the Joint Institute for Nuclear Astrophysics, the Kavli Institute for Particle Astrophysics and Cosmology, the Korean Scientist Group, the Chinese Academy of Sciences (LAMOST), Los Alamos National Laboratory, the Max-Planck-Institute for Astronomy (MPIA), the Max-Planck-Institute for Astrophysics (MPA), New Mexico State University, Ohio State University, University of Pittsburgh, University of Portsmouth, Princeton University, the United States Naval Observatory, and the University of Washington.

4.9   Appendix A

4.9.1   Failure of Single Sérsic Fitting at $z = 0$

Surface brightness profiles of galaxies in the local Universe rarely conform to simple analytic models (e.g., Allen et al. 2006, Simard et al. 2011). However, single Sérsic profile fitting is widely used for measuring their structural parameters. In order to test whether or not using single Sérsic fitting can bias the sizes of local galaxies with well-resolved profiles, we compare the half-light radii of our sample determined through different methods described in the text. In Figure 4.10, sizes of galaxies measured by using single Sérsic profile fitting are compared to their sizes derived from the non-parametric method. In the left top panel, the comparison is shown for all galaxies and in the left bottom panel, the relative median differences of sizes as a function of single Sérsic sizes are illustrated. As can be seen, for small galaxies, the median differences are small, however for large galaxies, the systematic differences reach to $\sim 25\%$, i.e., sizes from single Sérsic profile fitting are systematically larger than sizes from the non-parametric method for these galaxies. To diagnose the systematics, we show the comparison for blue and red galaxies separately in the middle and right panel of Figure 4.10, respectively. This shows that for blue ones the systematics are less than $\sim 10\%$, except for the large size end ($\sim 20\%$). However, for the red galaxies the systematic trend is significant and increases towards larger and massive objects (right bottom panel).

We also compare half-light radii from one-component Sérsic profile fitting and two-component Sérsic profile fitting in Figure 4.11. As it shows, sizes from single Sérsic fitting are on average larger for large and massive ones than sizes from two-component models. Specifically, for the red galaxies (right panels of Figure 4.11), there is a systematic bias toward larger sizes.

The fact that sizes from single Sérsic fitting are larger than sizes from the non-parametric method and two-component models, raises the question of how the half-light radii from one-component Sérsic profile fitting could have been overestimated? As an example, a typical profile of an early-type galaxy is shown in Figure 4.12. In the left panel, the observed profile is shown as black circles and the non-parametric fit overplotted as a blue line. The red line is the best single Sérsic fit to the galaxy. The single Sérsic profile to the whole observed profile does not match completely. This can be seen from the extra-light in central regions of the residual profile which is illustrated in the lower left panel (green
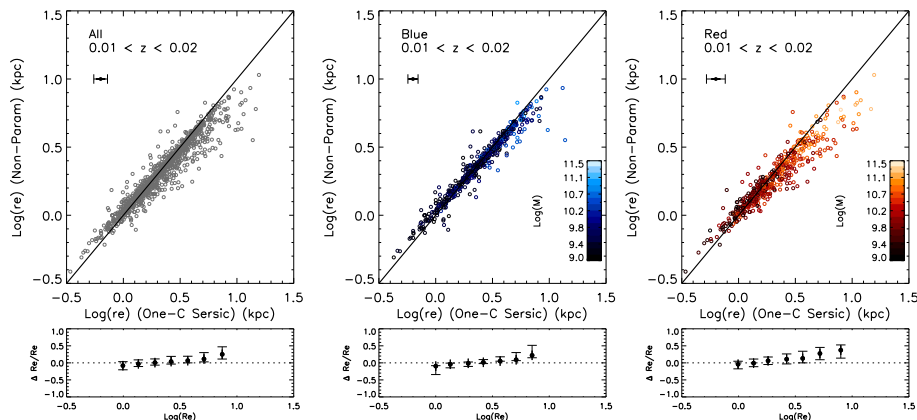
Figure 4.10 – Top rows: The comparison between sizes of galaxies at $0.01 < z < 0.02$ measured in two different ways, i.e., using single component Sérsic profiles and non-parametric method, for all galaxies (left panel), blue galaxies (middle panel) and red ones (right panel). Bottom panels, show the relative differences between sizes of galaxies as a function of their one component Sérsic sizes. The systematic differences between sizes of red galaxies increases up to about 40% and sizes based on single Sérsic profiles are larger that non-parametric sizes.

line). The half-light size from single Sérsic fitting is illustrated by black diamond and is larger than the one derived from non-parametric method (black triangle). The sizes derived using the residual-corrected method (Szomoru et al. 2010) is also shown as a black star and as can be seen, this method also gives smaller size than the single Sérsic profile fitting.

The light profile of this galaxy can be described better by adopting two-components Sérsic profiles. In the right upper panel of Figure 4.12, the two-component models and the total model are shown in dashed-dotted and solid red lines, respectively. The residual profile in the bottom right panel shows that this approach recovers most of the true profile of the galaxy. The half-light size derived from this method for this galaxy is consistent with the non-parametric size and hence smaller than single Sérsic profile fitting. It is worth testing whether the choice of PSF could introduce uncertainties. For that, we remeasure sizes of this galaxy using a nearby non-saturated star as a PSF. This gives us the same results as before. Therefore, we conclude that the SDSS synthetic PSFs do not significantly affect.

This basically shows that if massive galaxies are well-resolved or contain multiple components, structural measurements using a single analytical model could potentially be biased. We also used simulations to show this (see section 4.3.3).
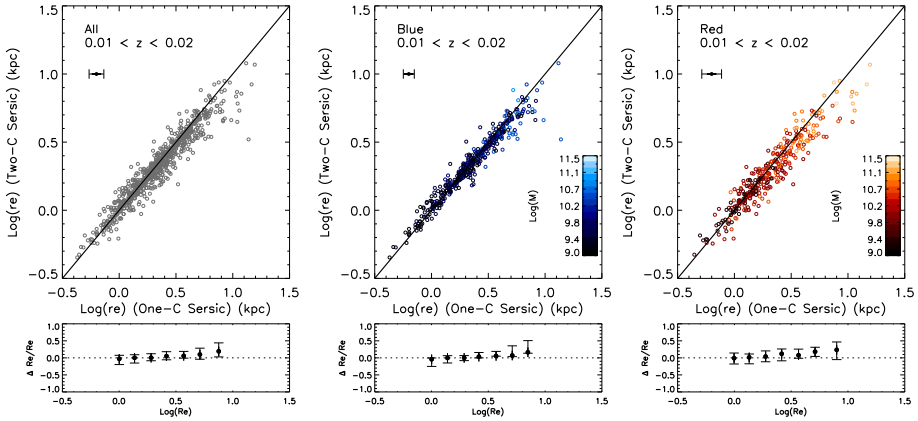
Figure 4.11 – The comparison between sizes of galaxies measured using one-component Sérsic profile fitting and two-component Sérsic surface brightness profiles (for ∼ 77% of total sample). As it can be seen, galaxies which their profiles could be estimated by two-component Sérsic profiles , have smaller two-component Sérsic sizes compare to one-component Sérsic sizes.

4.10 Appendix B

4.10.1 High Redshift Simulations

In order to check how well we can recover galaxy properties in J_{125} WFC3 images, we perform simulations by generating ∼ 2300 synthetic simulated galaxies (assuming single Sérsic surface brightness profile) with random properties within the following ranges: $20 < J_{125} < 26.5$, $0.5 < n < 6.5$ and $0 < r_e < 15$ kpc$_{z=1}$, convolving with the J_{125}-band PSF. We further add sky background by inserting the simulated galaxy images into the empty regions of the real J_{125}-band images, and then remeasuring their structural properties with the same procedure that we use for real galaxies.

The results of the simulations are shown in Figure 4.13. Synthetic simulated galaxies are split into late-type ($n < 2.5$; left panel) and early-type ($n > 2.5$; right panel) according to their input Sérsic indices. Then they are split into small bins over the size-magnitude plane. The relative differences between input and output sizes (i.e, $\Delta(r_e)/re_{in}$) in each small bin of size-magnitude distribution are measured and shaded accordingly. Then we overplot the distribution of artificially redshifted SDSS late-type and early-type galaxies on this size-magnitude plane, shown as blue and red points, respectively. Therefore, systematics in size measurements for each redshifted object can be estimated from this plot.

As it can be seen in Figure 4.13, for late-type galaxies the systematic differences over the range of artificially redshifted SDSS galaxies are less than few percent. The systematic differences for early-type galaxies are also very small and only increase at the very
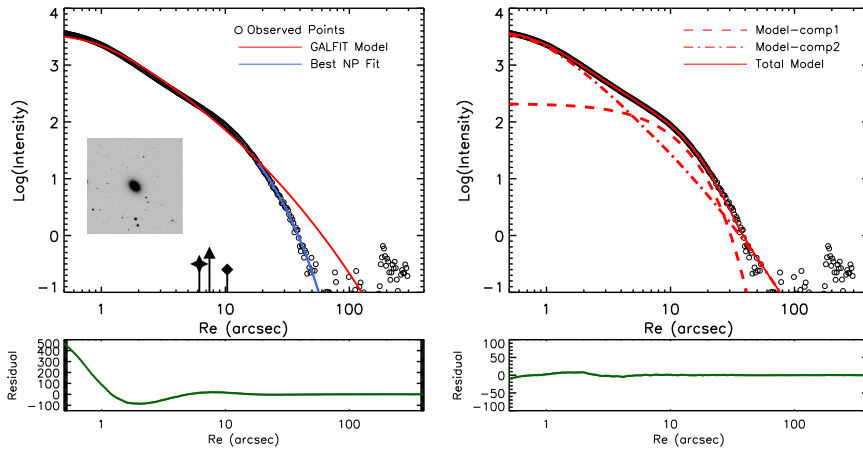
Figure 4.12 – The observed profile (black open circles) of a typical early-type galaxy. In the left panel, the red line represents the best-fit one component Sérsic profile and the blue line shows the best-fit one-dimensional Sérsic fit to the outer part of the galaxy ($> r_p etro_9 0$ for measuring non-parametric size). In the right panel, the solid red line represent the total best fit model from two-component models. The green lines in the bottom panels show the residuals from best-fits of one component Sérsic profile. The size that derived using residual-corrected method (Szomoru et al. 2010) is shown by a filled star and non-parametric size is shown by filled triangle. The filled diamond shows the size of this galaxy using single component Sérsic profile. This plot shows that profiles of galaxies at these very low redshift might be better explained by two components profiles.

faint magnitude end (i.e.$J_{125} > 25$). In general, comparing the distribution of artificially redshifted SDSS galaxies to the uncertainties in each bin shows that the systematics are expected to be very small ($< 10\%$ at most) for most of our sample. Therefore, we expect that our size measurement procedure at high-z recovers the properties of galaxies without introducing significant systematic biases.

The next set of simulations is designed to check our redshifting procedure. For this purpose, we also create two-dimensional single Sérsic model galaxies with a similar range of properties to the nearby SDSS galaxies. We assign them similar redshifts as our SDSS galaxy sample. Then we use our code to artificially redshift these mock galaxies to $z = 1$, insert them into J_{125} WFC3 images, and remeasure their properties using the method described in section 4.5.1. The results are illustrated in Figure 4.14. In the left panel, input sizes before redshifting and output sizes after redshifting are compared; in the right panel, the comparison of input and output Sérsic indices is shown. The error bars come from the dispersion between different realizations (i.e., using different empty regions). This plot shows that the properties of these single Sérsic model galaxies can be recovered after redshifting to $z = 1$ without any systematics and hence, our redshifting procedure works robustly.

It is also discussed in the text that using single Sérsic profile fitting likely measures the true structural parameters of galaxies at high redshifts. We verify this by simulating double-component galaxies and redshifting them to $z = 1$ (simulation (II) & Figure 4.7). In addition to these results, in order to test whether using low resolution images washes out the sub-components and changes the galaxies measured structural parameters, we remeasure galaxy sizes at $z = 0$ using single Sérsic profile fitting from their degraded images; i.e., images which are binned (by a factor of 4) and Gaussian smoothed. Figure 4.15 shows the sizes (top row panels) and Sérsic indices (bottom row panels) of these galaxies after smearing. It can be seen that sizes and Sérsic indices are smaller, especially for red galaxies after degrading. The results simply illustrate that the bright central parts of galaxies can bias the measurements of the structural properties of the galaxies in the nearby universe,when a single Sérsic model is used. Also, it shows that resolution should be taken into account for structural parameter measurements.
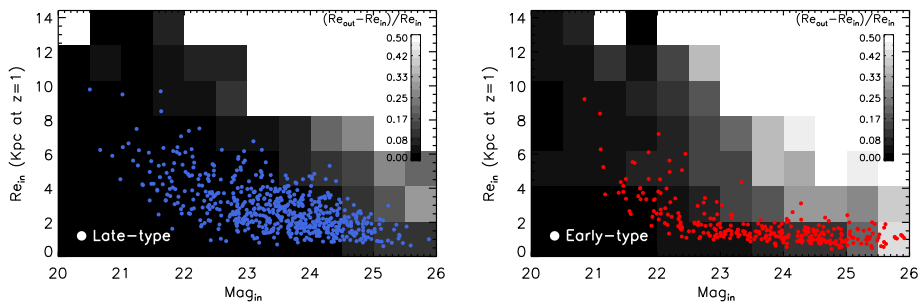
Figure 4.13 – The relative differences between input and output sizes of synthetic simulated galaxies (simulation III) are measured in small bins over the (input) size-magnitude plane (left panel: $n < 2.5$ and right panel: $n > 2.5$). In each bin, the colors correspond to the median relative differences between recovered and input sizes of simulated galaxies. The red and blue points represent the artificially redshifted SDSS galaxies (*Left panel*: Late-type galaxies and *Right panel*: Early-type galaxies) on the size-magnitude plane. This shows that the systematics on size measurements of our galaxies are very small over their size-magnitude distributions.
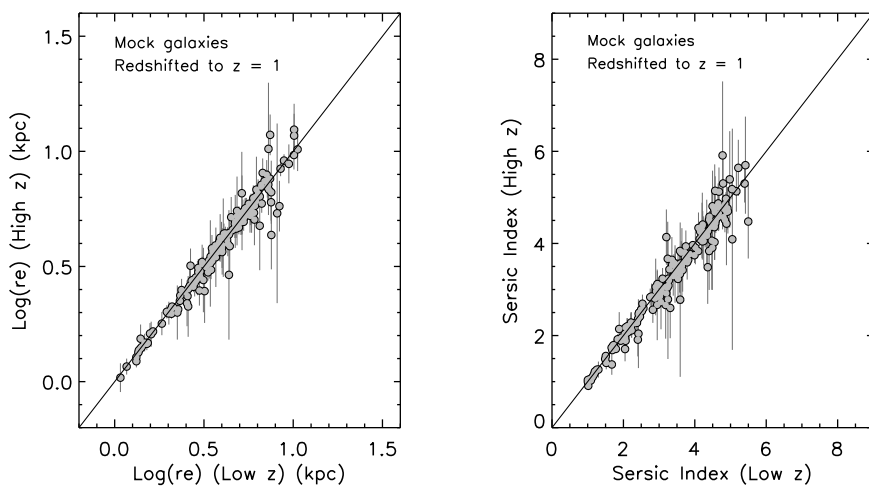

Figure 4.14 – Artificial single Sérsic model SDSS galaxies are created and then redshifted to $z = 1$ using our procedure. The left panel shows the comparison between their input sizes (at $z \sim 0$) to their sizes after artificially redshifted. The right panel illustrates the comparison between the input and output Sérsic indices. The results indicate that our procedure recovers the parameters of Sérsic model galaxies and there are no systematics on the measured sizes and Sérsic indices after redshifting these mock galaxies.
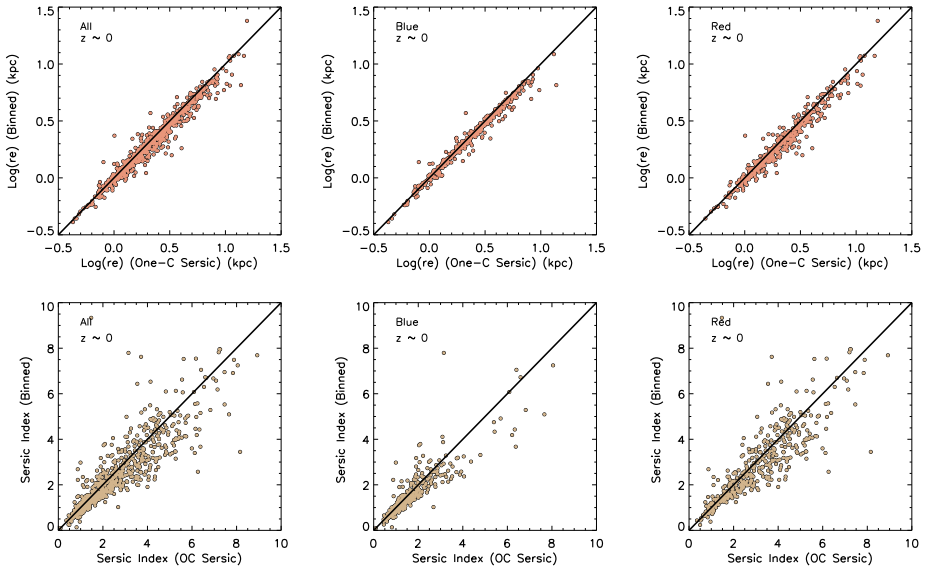
Figure 4.15 – Comparison of sizes (top row) and Sérsic indices (bottom row) of galaxies at $z = 0$ derived from single component Sérsic fits of SDSS galaxies before (labled as One-component) and after degrading the resolution (Labled as Binned; through binning and smoothing). This test shows that using single Sérsic fitting for well-resolved images of nearby galaxies could result in overestimating parameters such as sizes and Sérsic indices in compared to lower resolution images.

Bibliography

Abazajian, K. N., et al. 2009, ApJS, 182, 543

Allen, P. D., Driver, S. P., Graham, A. W., Cameron, E., Liske, J., & de Propris, R. 2006, MNRAS, 371, 2

Barden, M., Jahnke, K., & Häußler, B. 2008, ApJS, 175, 105

Barden, M., et al. 2005, ApJ, 635, 959

Bernardi, M. 2009, MNRAS, 395, 1491

Bernardi, M., Hyde, J. B., Sheth, R. K., Miller, C. J., & Nichol, R. C. 2007, AJ, 133, 1741

Bernardi, M., Meert, A., Vikram, V., Huertas-Company, M., Mei, S., Shankar, F., & Sheth, R. K. 2012, arXiv:1211.6122

Bertin, E., & Arnouts, S. 1996, A&AS, 117, 393

Blanton, M. R., et al. 2005, AJ, 129, 2562

Bouwens, R. J., et al. 2012, ApJ, 754, 83

Brinchmann, J., Charlot, S., White, S. D. M., Tremonti, C., Kauffmann, G., Heckman, T., & Brinkmann, J. 2004, MNRAS, 351, 1151

Buitrago, F., Trujillo, I., Conselice, C. J., Bouwens, R. J., Dickinson, M., & Yan, H. 2008, ApJ, 687, L61

Cimatti, A., et al. 2008, A&A, 482, 21

Conselice, C. J., Bluck, A. F. L., Ravindranath, S., Mortlock, A., Koekemoer, A. M., Buitrago, F., Grützbauch, R., & Penny, S. J. 2011, MNRAS, 417, 2770

Côté, P., et al. 2006, ApJS, 165, 57

Daddi, E., et al. 2005, ApJ, 626, 680

de Vaucouleurs, G. 1948, Annales d'Astrophysique, 11, 247

Dutton, A. A., et al. 2011, MNRAS, 410, 1660

Ferrarese, L., van den Bosch, F. C., Ford, H. C., Jaffe, W., & O'Connell, R. W. 1994, AJ, 108, 1598

Franx, M., van Dokkum, P. G., Schreiber, N. M. F., Wuyts, S., Labbé, I., & Toft, S. 2008, ApJ, 688, 770

Giavalisco, M., Livio, M., Bohlin, R. C., Macchetto, F. D., & Stecher, T. P. 1996, AJ, 112, 369

Graham, A. W., & Driver, S. P. 2005, pasa, 22, 118

Graham, A. W., Erwin, P., Trujillo, I., & Asensio Ramos, A. 2003, AJ, 125, 2951

Graham, A. W., & Worley, C. C. 2008, MNRAS, 388, 1708

Guo, Y., et al. 2009, MNRAS, 398, 1129

Hopkins, P. F., Cox, T. J., Dutta, S. N., Hernquist, L., Kormendy, J., & Lauer, T. R. 2009a, ApJS, 181, 135

Hopkins, P. F., Lauer, T. R., Cox, T. J., Hernquist, L., & Kormendy, J. 2009b, ApJS, 181, 486

Huang, S., Ho, L. C., Peng, C. Y., Li, Z.-Y., & Barth, A. J. 2012, arXiv:1212.2639

Janz, J., & Lisker, T. 2008, ApJ, 689, L25

Jedrzejewski, R. I. 1987, MNRAS, 226, 747

Kauffmann, G., et al. 2003, MNRAS, 341, 54

Kormendy, J. 1985, ApJ, 295, 73

Kormendy, J., Fisher, D. B., Cornell, M. E., & Bender, R. 2009, ApJS, 182, 216

Labbé, I., et al. 2003, ApJ, 591, L95

Lauer, T. R., et al. 1995, AJ, 110, 2622

—. 2007, ApJ, 664, 226

Law, D. R., Steidel, C. C., Shapley, A. E., Nagy, S. R., Reddy, N. A., & Erb, D. K. 2012, ApJ, 745, 85

Lintott, C., et al. 2011, MNRAS, 410, 166

Lisker, T., Debattista, V. P., Ferreras, I., & Erwin, P. 2006, MNRAS, 370, 477

Mancini, C., et al. 2010, MNRAS, 401, 933

Meert, A., Vikram, V., & Bernardi, M. 2012, arXiv:1211.6123

Mosleh, M., Williams, R. J., Franx, M., & Kriek, M. 2011, ApJ, 727, 5

Mosleh, M., et al. 2012, ApJ, 756, L12

Newman, A. B., Ellis, R. S., Bundy, K., & Treu, T. 2012, ApJ, 746, 162

Oesch, P. A., et al. 2010, ApJ, 709, L21

Patel, S. G., et al. 2012, arXiv:1208.0341

Peng, C. Y., Ho, L. C., Impey, C. D., & Rix, H.-W. 2010, AJ, 139, 2097

Petty, S. M., de Mello, D. F., Gallagher, III, J. S., Gardner, J. P., Lotz, J. M., Mountain, C. M., & Smith, L. J. 2009, AJ, 138, 362

Salim, S., et al. 2007, ApJS, 173, 267

Sérsic, J. L. 1963, Boletin de la Asociacion Argentina de Astronomia La Plata Argentina, 6, 41

Sersic, J. L. 1968, Atlas de galaxias australes

Shankar, F., Marulli, F., Bernardi, M., Mei, S., Meert, A., & Vikram, V. 2013, MNRAS, 428, 109

Shen, S., Mo, H. J., White, S. D. M., Blanton, M. R., Kauffmann, G., Voges, W., Brinkmann, J., & Csabai, I. 2003, MNRAS, 343, 978

Simard, L., Mendel, J. T., Patton, D. R., Ellison, S. L., & McConnachie, A. W. 2011, ApJS, 196, 11

Szomoru, D., Franx, M., & van Dokkum, P. G. 2012, ApJ, 749, 121

Szomoru, D., et al. 2010, ApJ, 714, L244

Toloba, E., Boselli, A., Peletier, R. F., Falcón-Barroso, J., van de Ven, G., & Gorgas, J. 2012, A&A, 548, A78

Trujillo, I., et al. 2006b, ApJ, 650, 18

Turner, M. L., Côté, P., Ferrarese, L., Jordán, A., Blakeslee, J. P., Mei, S., Peng, E. W., & West, M. J. 2012, ApJS, 203, 5

van de Sande, J., et al. 2012, arXiv:1211.3424

van den Bergh, S., Abraham, R. G., Whyte, L. F., Merrifield, M. R., Eskridge, P. B., Frogel, J. A., & Pogge, R. 2002, AJ, 123, 2913

van der Wel, A., Holden, B. P., Zirm, A. W., Franx, M., Rettura, A., Illingworth, G. D., & Ford, H. C. 2008, ApJ, 688, 48

van Dokkum, P. G., et al. 2008, ApJ, 677, L5

Weinzirl, T., et al. 2011, ApJ, 743, 87

Williams, R. J., Quadri, R. F., Franx, M., van Dokkum, P., Toft, S., Kriek, M., & Labbé, I. 2010, ApJ, 713, 738

Galaxy Zoo: Passive Red Spirals

K. L. Masters, Moein Mosleh, A. Kathy Romer, Robert C. Nichol, Steven P. Bamford, Kevin Schawinski, Chris J. Lintott, Dan Andreescu, Heather C. Campbell, Ben Crowcroft, Isabelle Doyle, Edward M. Edmondson, Phil Murray, M. Jordan Raddick, Anže Slosar, Alexander S. Szalay, and Jan Vandenberg

Abstract

We study the spectroscopic properties and environments of red (or passive) spiral galaxies found by the Galaxy Zoo project. By carefully selecting face-on, disk dominated spirals we construct a sample of truly passive disks (*i.e.,* they are not dust reddened spirals, nor are they dominated by old stellar populations in a bulge). As such, our red spirals represent an interesting set of possible transition objects between normal blue spiral galaxies and red early types, making up $\sim 6\%$ of late-type spirals. We use optical images and spectra from SDSS to investigate the physical processes which could have turned these objects red without disturbing their morphology. We find red spirals preferentially in intermediate density regimes. However there are no obvious correlations between red spiral properties and environment suggesting that *environment alone is not sufficient to determine if a galaxy will become a red spiral*. Red spirals are a very small fraction of all spirals at low masses ($M_\star < 10^{10} M_\odot$), but are a significant fraction of the spiral population at large stellar masses showing that *massive galaxies are red independent of morphology*. We confirm that as expected, red spirals have older stellar populations and less recent star formation than the main spiral population. While the presence of spiral arms suggests that major star formation cannot have ceased long ago (not more than a few Gyrs), we show that these are also not recent post-starburst objects (having had no significant star formation in the last Gyr), so *star formation must have ceased gradually*. Intriguingly, red spirals are roughly four times as likely than the normal spiral population to host optically identified Seyfert/LINER (at a given stellar mass and even accounting for low luminosity lines hidden by star formation), with most of the difference coming from objects with LINER-like emission. We also find a curiously large optical bar fraction in the red spirals ($70 \pm 5\%$ verses $27 \pm 5\%$ in blue spirals) suggesting that *the cessation of star formation and bar instabilities in spirals are strongly correlated*. We conclude by discussing the possible origins of these red spirals. We suggest they may represent the very oldest spiral galaxies which have already used up their reserves of gas - probably aided by strangulation or starvation, and perhaps also by the effect of bar instabilities moving material around in the disk. We provide an online table listing our full sample of red spirals along with the normal/blue spirals used for comparison.

5.1   Introduction

The advent of large galaxy surveys like the Sloan Digital Sky Survey (SDSS) in which photometry (and therefore colours) are readily available for millions of objects has lead to the common use of optical colours to define "early" and "late" type galaxy samples (e.g. Simon et al. 2009, Salimbeni et al. 2008, Lee & Pen 2007, Croton et al. 2007, Bundy et al. 2006, Cooray 2005). This method is particularly favoured since obtaining morphologies for large numbers of galaxies has until recently been impossible. This simplification is justified since it has been shown many times that the majority of galaxies follow a strict colour-morphology relation. For example Mignoli et al. (2009) argued that 85% of galaxies to z~1 are either red, bulge-dominated galaxies or blue, disk dominated galaxies; while Conselice (2006) showed a similar result for 22000 low redshift galaxies (both using automated methods for morphological classification).

However the clear correlation between colour and morphology is surprising, given that the colours of galaxies are determined primarily by their stellar content (and therefore their recent star formation history, mostly within the last Gyr) while the morphology is primarily driven by the dynamical history. The clear link between colour and morphology then gives a strong indication that the timescales and processes which drive morphological transformation and the cessation of star formation are strongly related - at least in most cases. In this paper however, we consider a class of object (the red spirals) where the link described above appears to be broken.

Since the morphology-density relation was first quantified (Dressler 1980) many mechanisms have been proposed for the transformation of blue, star forming, disk galaxies in low density regions of the universe, to red, passive, early type galaxies in clusters. A recent review of many of the proposed mechanisms, and the evidence supporting them, can be found in Boselli & Gavazzi (2006). Clearly two things must happen for a star forming blue spiral galaxy to turn into a passive red early type. First, star formation must cease (which can indirectly alter the morphology by causing spiral arms and the disk in general to fade, possibly producing an S0 or lenticular from a spiral), and secondly, in order to produce a *bona fide* elliptical the same, or a different process must also dynamically alter the stellar kinematics of the galaxy.

The presence of an unusually red or passive (*i.e.,*. non-star forming) population of spiral galaxies in clusters of galaxies was first noticed by van den Bergh (1976) in the Virgo cluster. Later studies of distant cluster galaxies in *Hubble Space Telescope* (HST) imaging also revealed a significant number of so-called "passive" spiral galaxies with a lack of on-going star formation (Couch et al. 1998; Dressler et al. 1999; Poggianti et al. 1999). Passive late-type galaxies were identified at lower redshifts in the outskirts of SDSS clusters by Goto et al. (2003), using concentration as a proxy for morphology. Passive spirals in a cluster at $z \sim 0.4$ were studied by Moran et al. (2006) who found star formation histories from GALEX observations consistent with the shutting down of star formation from strangulation (as described by Bekki et al. 2002). Passive spirals have also been revealed in a cluster at $z \sim 0.1$ in the STAGES survey, using HST morphologies Wolf et al. (2009), rest frame NUV-optical SEDs (Wolf et al. 2005) and $24\mu m$ data from Spitzer (Gallazzi et al. 2009). In that series of papers, "dusty red late-types" and

"optically passive late-types" are found to be largely the same thing, with a non-zero (but significantly lowered) star formation rate revealed by the IR data.

Red spirals/late types have been studied in several recent papers (Lee et al. 2008, Deng et al. 2009, Hughes & Cortese 2009, Cortese & Hughes 2009), as well as Mahajan & Raychaudhury (2009) who talk about blue passive galaxies (*i.e.,* galaxies with blue colours, but showing no indication of recent star formation in their spectra) which mostly appear to have late type morphologies and have very recently shut down star formation. These might be the progenitors of the red spirals. Bundy et al. (2010) have studied the redshift evolution of red sequence galaxies with disk like components in COSMOS and use it to estimate that as many as 60% of spiral galaxies must pass through this phase on the way to the red sequence - making it an important evolutionary step.

The Galaxy Zoo project (Lintott et al. 2008) revealed the presence of a significant number of visually classified spiral galaxies which are redder than the blue cloud (between 16-28% of the total galaxy population depending on environment, Bamford et al. 2009). In this paper we study in more detail the physical properties and environments of this population of red spiral galaxies. Galaxies drawn from this population have the morphological appearance of spiral galaxies with a distinct spiral arm structure, but have rest-frame colours which are as red as a typical elliptical galaxy, indicating little or no recent star formation activity. We are studying these objects in order to identify the physical process which is most important in their formation.

It is clear that all spiral galaxies can be affected by various physical processes as they evolve – in this paper we attempt to identify which are most important for red spirals, asking how they are able to shut down star formation while retaining their spiral morphology. A list of possible mechanisms includes processes that depend on environment such as: (1) galaxy-galaxy interactions: in high density regions there is an increased probability of interaction with other galaxies. Most major mergers destroy spiral structure (Toomre & Toomre 1972) unless they involve very gas rich progenitors (Hopkins et al. 2009), but some interactions can be quite gentle (*e.g.,* Walker, Mihos & Hernquist 1996), for example minor-mergers, tidal interactions etc. (2) Interaction with the cluster itself also occurs and can remove the gas which forms the reservoir for star formation. This can be due to tidal effects (e.g. Gnedin 2003), or interaction with the hot intercluster gas, either through thermal evaporation (Cowie & Songaila 1977) or ram pressure stripping (Gunn & Gott 1972). (3) Processes like harrassment (Moore et al. 1999) and starvation or strangulation (Larson et al. 1980, Bekki et al. 2002) have also been shown to have a significant effect on late type galaxies. Harrassment refers to the heating of gas by many small interactions, while starvation or strangulation refers to the gradual exhaustion of disk gas after the hot halo has been stripped away. These mechanisms both occur at much larger cluster radii (*i.e.,* lower densities) than the "classic" environmental effects. Internal mechanisms could be more important. For example, (4) the latest semi-analytical models of galaxy formation all invoke feedback from a central massive black hole (or active galactic nuclei; AGN) to explain the most massive red elliptical galaxies (Granato et al. 2004, Silk 2005, Schawinski et al. 2006, Croton et al. 2006, Bower et al. 2006), although the effect of this process on disk galaxies has been studied less, it still may have some effect (Okamoto, Nemmen & Bower 2008). (5) Another culprit could be bar instabilities in spiral galaxies

which drive gas inwards (eg. Combes & Sanders 1981) and may trigger AGN activity and/or central star formation (eg. Shlosman et al. 2000), perhaps using up the reservoir of gas in the outer disk and making spirals red. (6) Finally red spirals could simply be old spirals which have used up all their gas in normal star formation activities without having any major interactions. In normal spirals, the gas that feeds ongoing star formation comes from infall of matter from a reservoir in the outer halo (Boselli & Gavazzi 2006). As first suggested by Larson, Tinsley & Caldwell (1980) and expanded by Bekki et al. (2002) the removal of gas from this outer halo ("strangulation", or "starvation") will cause a gradual cessation of star formation proceeding over several Gyrs.

We describe the sample and data along with the selection of the "red spirals" in more detail in Section 5.2. In Section 5.3 we discuss the stellar populations and star formation history of the red spirals. In Section 5.4 we discuss their environment and the environmental dependence of star formation. The impact of AGN is considered in Section 5.5, and bar instabilities are discussed in Section 5.6. In Section 5.7 we discuss the plausible mechanisms for formation of the red spirals and future directions which could be taken to distinguish between them. We present a summary and conclusions in Section 5.8. The adopted cosmological parameters throughout this paper are $\Omega_m = 0.3$, $\Omega_\Lambda = 0.7$ and $H_0 = 70$ km s^{-1} Mpc^{-1}.

5.2 Sample Selection and Data

The sample of visually classified spiral galaxies used in this paper is drawn from the Galaxy Zoo (GZ1) clean catalogue (Lintott et al. 2008) which, by an order of magnitude, is the largest morphologically classified sample of galaxies. To make this unprecedented sample, over 160,000 volunteers visually inspected images of SDSS galaxies independently via an internet tool (the original GZ1 sample was selected from the SDSS Data Release 6; Adelman-McCarthy et al. 2008). For more information on the classification process in GZ1 and the conversion of multiple classifications per galaxy to redshift bias corrected type "likelihoods" see Lintott et al. (2008) and Bamford et al. (2009). In brief, we use the spiral likelihood p_{spiral} and (in order to tell if the spirals have visible spiral arms) the quantities p_{CW} and p_{ACW} which describe how likely the spiral is to have "clockwise" or "anti-clockwise" arms respectively.

We make a volume-limited sample of galaxies from the GZ1 catalogue by selecting only objects from the SDSS Main Galaxy Sample (Strauss et al. 2002) with spectroscopic redshift between 0.03 < z < 0.085 and by limiting the sample to an absolute magnitude of $M_r < -20.17$. This redshift range is picked to remove problems with peculiar velocities at the low redshift end (which would bias distance dependent quantities) and the upper limit is chosen as a compromise between sample size and luminosity range, (and also a redshift up to which reliable local densities - see below - are available).

Our photometric quantities are taken from the SDSS DR6 Adelman-McCarthy et al. (2008). We use model magnitudes for colours, and Petrosian magnitudes for total luminosities. We also make use of shape/structural parameters from SDSS, namely the axial ratio (a/b) from the r-band isophotal measurement which is used as a proxy for disk incli-

nation; and `fracdeV` (or f_{DeV}) - the fraction of the best fit light profile which comes from the de Vaucouleurs fit (as opposed to the exponential fit) and which is used as a proxy for bulge size in these visually classified spirals (as discussed in Masters et al. 2010).

SDSS 3" fibre spectra are available for all galaxies in our sample. We use equivalent widths (EW) and absorption line indices measured for SDSS DR7 spectra by the MPA-Garching group whose methods are described in Tremonti et al. (2004)[1].

As an estimate of stellar mass, we use the empirical fit in Baldry et al. (2006) which gives a stellar mass-light ratio in the r-band as a function of the $(u-r)$ colour of the galaxy (based on calculations of stellar masses from Kauffmann et al. (2003a) and Granato et al. (2004) using the Bruzual & Charlot (2003) stellar population models). Obviously this is an oversimplification of the calculation of stellar masses, not taking into account the varied star formation histories of galaxies with the same colour and luminosity; however the method does have the advantage of being simply related to only two measured physical properties of the galaxies (colour and luminosity).

The local galaxy densities used in this paper are identical to those used in Bamford et al. (2009). The details of the method are described in Baldry et al. (2006). Briefly, Σ_N is determined by $N/(\pi\, d_N^2)$, where d_N is the projected distance to the Nth nearest galaxy (with $M_r < -20$) within $cz \pm 1000$ km s^{-1}. The final value used, Σ, is the average of Σ_N for N = 4 and 5. These local densities include a correction for redshift incompleteness due to fiber collisions by considering the photometric redshift likelihood distributions for galaxies without spectra. Typical values of Σ range from 0.05 Mpc^{-2} in voids to 20 Mpc^{-2} in clusters (Baldry et al. 2006).

5.2.1 Selection of Red Spiral Galaxies

We wish to select from the GZ1 volume limited sample a subset of truly passive red disk-dominated spiral galaxies (*i.e.,* not dust reddened, nor red because they are dominated by bulge emission). We use a cut in the spiral likelihood (corrected for the small bias described in the Appendix of Bamford et al. 2009) of $p_{spiral} \geq 0.8$. Two things can complicate the picture in a sample selected purely by colour and spiral likelihood:

1. Dust reddening of edge-on spiral galaxies

2. Contamination by early-type spirals and/or S0s.

Masters et al. (2010) show that the impact of dust reddening can be significant for inclined spiral galaxies, and that spiral galaxies with large bulges (as measured by `fracdev`) are intrinsically red. Therefore with no cuts on inclination or bulge size, a red spiral sample will be dominated by inclined dust reddened spirals, and spirals with large bulges. We choose in this work to study only the most face-on spiral galaxies, requiring $\log(a/b) < 0.2$. This will minimize the impact of dust reddening on the sample (although we note that even at face-on spirals can be dust reddened; for example Masters et al. 2010 find a median Balmer decrement of 0.3 ± 0.3 mags in the centres of face-on GZ1 spirals).

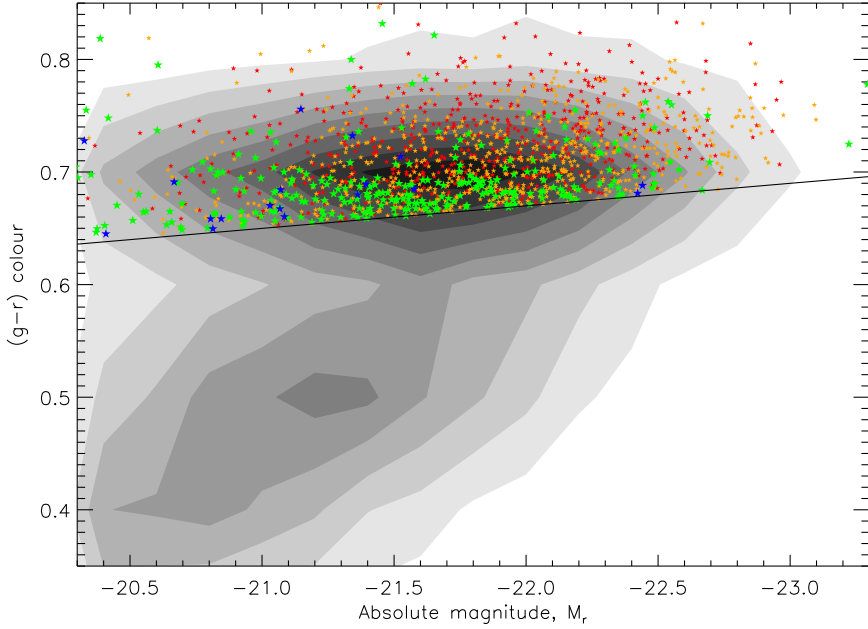[1] http://www.mpa-garching.mpg.de/SDSS/

Figure 5.1 – Colour magnitude diagram of the "face-on" ($\log(a/b) < 0.2$) volume limited clean GZ1 sample. The greyscale contours show the location of galaxies in the red sequence and blue cloud. The solid line indicates the blue edge of the red sequence of GZ1 early types. All red spirals (having visible spiral arms) are shown colour coded by `fracdev` (blue: $f_{DeV} < 0.1$, which roughly corresponds to type Sd; green: $0.1 < f_{DeV} < 0.5$, or Sb-Sc; orange: $0.5 < f_{DeV} < 0.9$, or Sa-S0/a; red: $f_{DeV} > 0.9$ which are spirals having very large bulges - but note that spiral arms are still visible here, so these are not S0s.). Our final red spiral sample selects only those galaxies with $f_{DeV} < 0.5$ (*i.e.,* the blue and green points) to select against spirals dominated by light from the bulge.

Both Lintott et al. (2008) and Bamford et al. (2009) show that contamination of S0s into the GZ1 clean spiral sample should be small - an estimate of 3% contamination is made. Furthermore we use `fracDev` ≤ 0.5 to select "disky" spirals. As illustrated in Masters et al. (2010) using a small sample of GZ1 spirals with B/T from the Millennium Galaxy Catalogue (Liske et al. 2003) this selects spiral galaxies with $B/T < 0.25$, or of types ~Sb–Sc (where this relation between typical B/T and Hubble type comes from Simien & de Vaucouleurs 1986). One caveat to note here is that both `fracdeV` and B/T are light-weighted quantities, so in using the same `fracdeV` limit for both red and blue spirals will results in the red spirals having a slightly *lower* upper limit in bulge *mass* fraction than the blue spirals. This slight bias should only make the conclusions below stronger, as the red spirals may on average be more disk dominated than the comparison blue spiral sample.

Finally we require that spiral arms be visible to GZ1 users, using $p_{CW} > 0.8$ or $p_{ACW} > 0.8$. The presence of spiral arms gives an indication that these red spirals may have only recently stopped forming stars, since spiral structures are expected to persist for only a short time after star formation ceases (for example Bekki et al. (2002) found that spirals arms persisted for only a few Gyrs after the gas which provides the reservoir for ongoing star formation was removed).

We show in Figure 5.1, the colour magitude diagram of the "face-on" volume limited clean GZ1 sample. The locus of the galaxy population is illustrated by the greyscale contours, and the positions of visually classified spirals in the red sequence are hi-lighted. The best fit to the red sequence of early types ($p_{el} \geq 0.8$) is $(g - r) = 0.73 - 0.02(M_r + 20)$, and the scatter is $\sigma = 0.1$ mags. We therefore define the blue edge of the red sequence as

$$(g - r) = 0.63 - 0.02(M_r + 20), \tag{5.1}$$

which is indicated by the solid line in Figure 5.1, and define a red spiral as one redder than this limit. Since the limit depends on magnitude, we point out that in our definition a blue spiral with a high luminosity could actually be slightly redder than a red spiral with a low luminosity.

The colour cut used here to select red spirals is different from than that used by either Bamford et al. (2009), who used a cut in $(u - r)$ vs. stellar mass; or Skibba et al. (2009), who used k-corrected (to $z = 0.1$) magnitudes, which reddens the red sequence by ~ 0.1 mags. Our cut is more conservative that either of those papers; they effectively select red spirals as being redder than most of the blue cloud, while we select red spirals to be *as red as most elliptical galaxies*. The difference in the two approaches is especially large at the low luminosity/stellar mass end of the galaxy population where (as can be seen in Figure 5.1) the blue cloud is significantly bluer than the red sequence. However, the major difference in our sample and all previous ones used to study passive or red spirals is that we have made an effort to remove dust reddened inclined spirals, which has not been done before (e.g. Bamford et al. 2009, Skibba et al. 2009, Wolf et al. 2009).

Our final sample consists of 5433 face-on disky spirals with visible spiral arms, 294 of which (or 6%) are classified as red. In what follows, we refer to the remaining 5139 spirals as our comparison sample a refer to them as either "blue" spirals, or "normal" spirals.
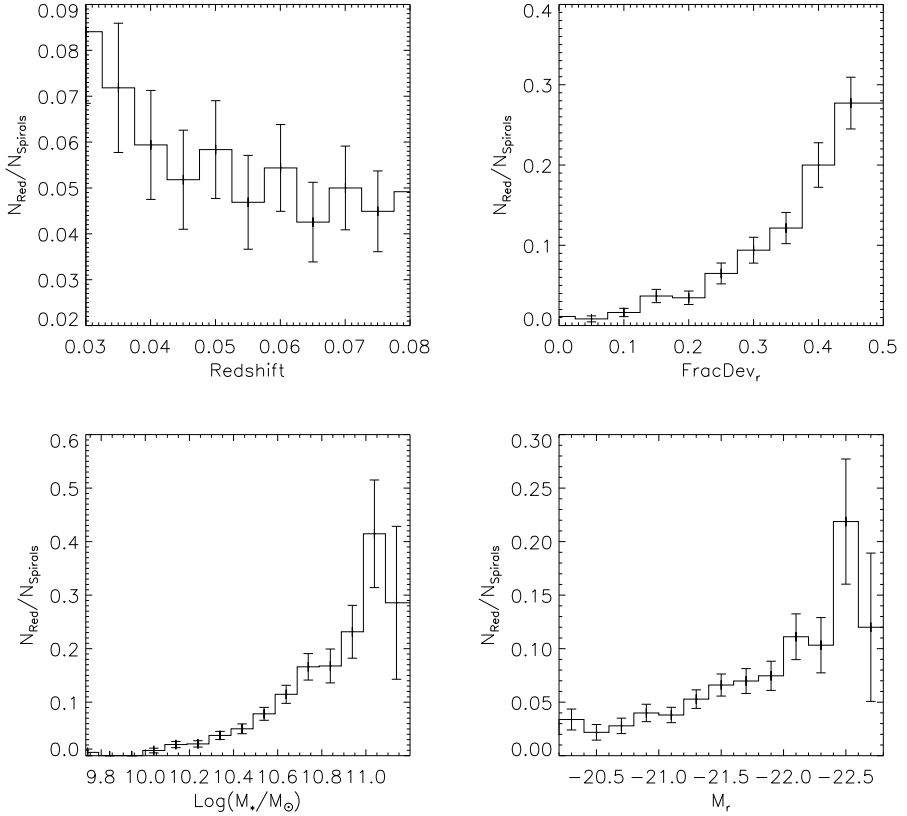
Figure 5.2 – This figure shows the fraction of all face-on, disky GZ1 spirals which are found to be red (*i.e.*, N_{red}/N_{spiral}) as a function of (1) redshift, (2) `fracdeV` (or bulge size), (3) stellar mass, and (4) *r*-band absolute magnitude. $\sqrt{N}$ counting errors are shown.

We provide an electronic table listing the SDSS names, positions and optical photometry parameters used in this paper for these two samples (our red spirals and comparison sample). A sample of this table is provided in the Appendix.

Figure 5.2 shows the redshift, `fracdeV` (for bulge size), luminosity and stellar mass distributions of the red spirals compared to all spirals (in the face-on, disky sample). Red spirals are more likely to be found at the higher luminosity and larger `fracdeV` (and hence larger bulge) end of the spiral distribution showing that as is well known, luminous spirals with large bulges (earlier spiral types) are more likely to be red. There is a slight trend with redshift which can be explained by effect of the luminosity distribution in a volume limited sample.

As also discovered by Wolf et al. (2009), red (or passive) spirals are an insignificant fraction of the total spiral population at stellar masses below $\sim 10^{10}$ $M_\odot$ (although note that Bamford et al. 2009 shows that in the densest regions the few remaining low mass spirals are mostly red) but are a significant fraction of spirals at large stellar masses. This shows that *massive galaxies are red independent of morphology*. However we note here that this mass distribution may be slightly biased by our decision to classify spirals as red only if they are *as red as ellipticals*. This cut biases against low mass red spirals as the blue cloud at low masses/luminosities moves further from the red sequence. Our sample is also incomplete for red objects below $10^{10.3} M_\odot$ which corresponds to the luminosity limit for the reddest objects. Finally, we comment that the stellar population models of Bruzual & Charlot (2003) on which the Baldry et al. (2006) stellar masses are based, struggle to make red low mass objects (since all their red objects must be very old, and therefore have very high mass-light ratios) so the use of this stellar mass estimate may anyway bias high the masses of the redder spirals. A more detailed modelling of the star formation history using stellar populations which account for the known populations of young red stars (the thermally pulsing asymptotic giant branch (TP-AGB) phase included in Maraston 2005) would provide more reliable stellar masses for these objects.

Figure 5.3 shows example images of red and blue spirals from our sample of face-on disky spirals. The blue spirals shown have been picked to have similar redshifts and absolute magnitudes as the red spiral directly above them. A range of redshifts are shown. In these *gri* colour composite images the colour difference between red and blue spirals is quite clear to the eye. Figure 5.4 shows SDSS fibre spectra for the same galaxies in Figure 5.3 (arranged in the same order), and even in this small sample it is clear that red spirals show less (but not zero) nebular emission from on-going star formation than the blue spirals (since they have smaller Hα emission lines) and have older stellar populations (the break at ~ 4000Å is larger in the red spirals than the blue spirals).

5.3   Star Formation in Red Spirals

In this section, we use the SDSS fibre spectra to study in more detail the star formation history and mean stellar age of "red spiral" galaxies with reference to our comparison sample of blue spirals. Spectroscopic parameters are ideal for studying the stellar content of galaxies. A full star formation history model fit to the galaxy spectra is beyond the
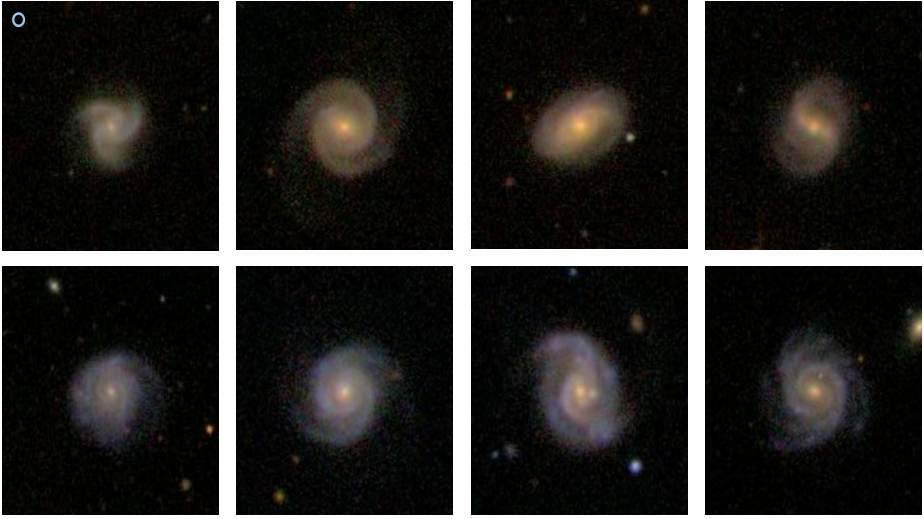
Figure 5.3 – *Top row:* examples of face-on, red, disky spirals with visible arms (as described in the text), *Bottom row*: face-on, blue, disky spirals picked to have similar redshifts, absolute *r*-band magnitudes, angular sizes and `fracdeV` values as the red spiral immediately above them. Images are SDSS *gri* composites, all $1' \times 1'$ in size (these are some of the largest angular size galaxies in our sample). The size of the SDSS fibre is indicated at top left of the top left image. Galaxies are (in red/blue pairs from left to right): SDSS J131428.83+334109.2 and SDSS J130058.63+395132.1 at $z \sim 0.04$, $M_r \sim -20.3$; SDSS J082959.05+304340.1 and SDSS J100515.00+513545.9 at $z \sim 0.05$ and $M_r \sim -21.7$; SDSS J104034.48+004902.6 and SDSS J123317.60+575620.1 at $z \sim 0.07$ and $M_r \sim -22.6$; and SDSS J134248.47+145553.5 and SDSS J155357.57+383923.9 at $z \sim 0.08$ and $M_r \sim -22.3$.
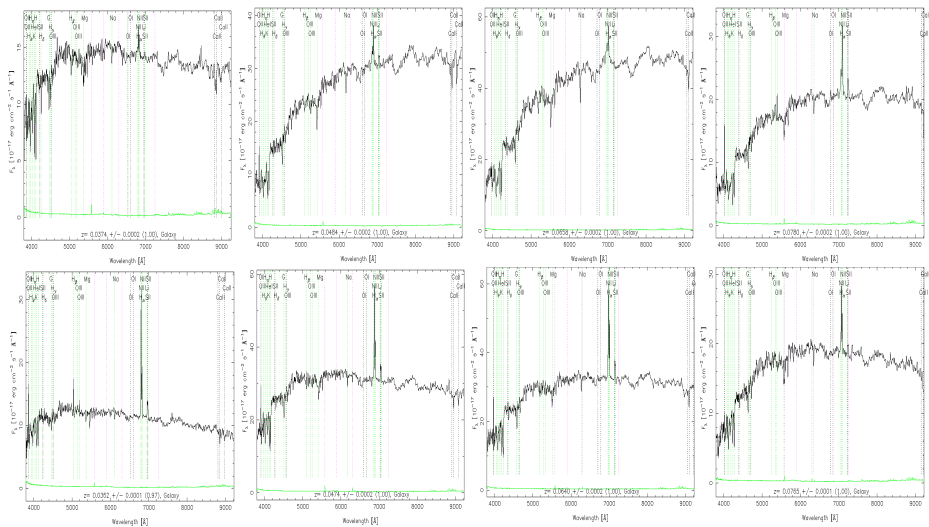
Figure 5.4 – SDSS fibre spectra of the spirals shown in Figure 5.3. Even in the central 3″, these spirals are clearly different in colour; the red spirals (top) mostly have continuum emission which increases towards long wavelengths (*i.e.,* a red colour), while the blue spirals have continuum levels decreasing in that direction. Also note the significantly larger Hα emission in the spectra of the blue spirals (indicative of more ongoing star formation), and the larger break at ~ 4000Å in the spectra of the red spirals (indicating an older stellar population).
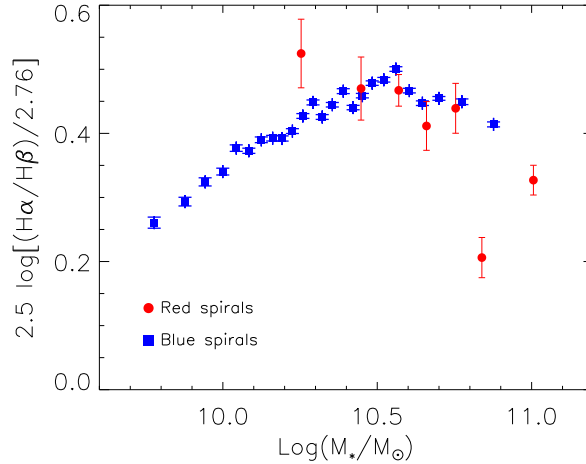
Figure 5.5 – Balmer decrement in the SDSS fibre (expressed in magnitudes of extinction between Hα and Hβ) as a function of stellar mass for the blue (blue squares) and red (red dots) face-on disky spirals. Error bars indicate our estimate of the 1σ error on the median value.

scope of this paper, but absorption line indices such as Hδ_A and the 4000Å break strength provide information about stellar content and recent star formation history of a galaxy, while $H\alpha$ and [OII] emission lines can indicate the presence of recent star formation.

5.3.1 Dust Content

Before proceeding to use the spectral information to study the stellar content of the red spirals we first want to check the dust content of the red spirals relative to the blue spirals. It is possible that the red colours of the spirals could be due to an enhanced amount of extinction and reddening from dust (even in our specially selected sample of face-on spirals designed to minimize dust effects) rather than an ageing stellar population from a lack of recent star formation. In fact Wolf et al. (2009) find that ongoing star formation in their red spirals is obscured, although we note again that their objects include dust reddened inclined spirals which we have removed.

In order to quantify the levels of extinction we compare the difference in flux between the first two lines in the Balmer series (Hα and Hβ). The expected flux ratio between these lines is $\mathfrak{R}_{int} = F_\alpha/F_\beta = 2.76$, and has only a mild dependence on the temperature of the gas emitting the radiation (from $\mathfrak{R}_{int} = 3.30$ at 2500°K to $\mathfrak{R}_{int} = 2.76$ at 20000°K; Osterbrock 1989). Therefore, deviations from the expected ratio can be used to measure the relative extinction between H_α (at 6562.8 Å in the r-band) and H_β (at 4861.3 Å in

g-band). The relative extinction between these two wavelengths in magnitudes is

$$E(H_\beta - H_\alpha) = 2.5 \log \frac{\mathcal{R}_{obs}}{\mathcal{R}_{int}}, \tag{5.2}$$

which is equivalent to a colour in narrow band filters at these wavelengths.

In Figure 5.5, we plot the Balmer decrements from the 3" SDSS fibre of blue and red spirals as a function of their stellar mass. This figure clearly indicates an increase in dust content of blue spirals as a function of stellar mass to a maximum at around $M \sim 10^{10.5} M_\odot$. The trend is less clear in the red spirals where the numbers are significantly smaller, but tentatively supports a drop off in dust content for the highest mass objects (as also seen in Masters et al. 2010). A negligible number of face-on spirals (either red or blue) have zero Balmer decrements in their central regions, showing that dust reddening always plays some role. However, we see no evidence for red spirals having significantly larger dust content than blue spirals at a given stellar mass (except perhaps in the lowest mass bin of the red spirals) and thus argue that the difference in colour is not due to differences in the dust content of the two populations.

5.3.2 Recent Star Formation History

Following the method in Kauffmann et al. (2003a), we use the Balmer absorption-line index $H\delta_A$ and the $D_n(4000)$ break to estimate mean stellar ages and recent star-burst activity of our sample.

The observed spectrum of a galaxy is the combination of flux from many stars. In galaxies with old stellar populations there are a large number of stellar absorption lines (mostly from ionized metals) which crowd together at around 4000Å. The 4000Å break which they produce is the strongest discontinuity seen in the optical spectrum of a galaxy. In galaxies with a younger stellar population, there are many more hot stars, and the metals in them are multiply ionized. This significantly reduces the strength of the break, making it a good indicator of the mean age of a galaxy's stellar population. We follow Kauffmann et al. (2003a) and represent the strength of the 4000Å break by the $D_n(4000)$ index (Balogh et al. 1999).

$H\delta_A$ absorption lines can be used to trace the recent (≤ 1 Gyr) star formation activity of galaxies (Kauffmann et al. 2003a). $H\delta_A$ in the integrated galaxy spectra is almost entirely the contribution of A-type stars. The peak of this absorption feature thus occurs roughly 1 Gyr after a burst of star formation, once O and B stars have expired and the integrated light is dominated by A stars.

Histograms of the distribution of the two measurements for all the red and blue spirals are shown in Figure 5.6. In Figure 5.7, we plot $H\delta_A$ versus $D_n(4000)$ for our blue and red spirals samples split into 4 bins of stellar mass (starting at $\log(M_\star/M_\odot) = 10.3$ where the sample is complete for both red and blue spirals). These figures illustrate that the red spirals, on average (luminosity weighted), have both older stellar populations and are less likely to have had significant bursts of star formation in the last Gyr (they have larger mean $D_n(4000)$ and smaller $H\delta_A$). The data are overplotted on the models of Kauffmann et al. (2003a) showing the regions covered by their starburst (filled triangle), poststarburst
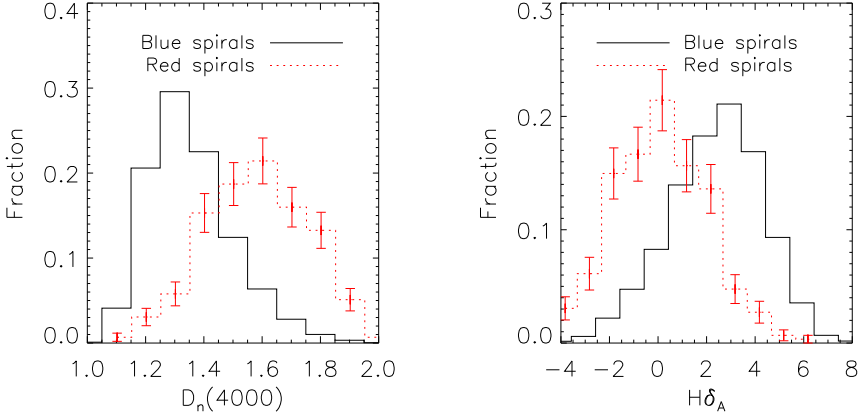
Figure 5.6 – Histograms of the distribution of Hδ_A and $D_n(4000)$ for the red and blue spiral samples (solid and dotted lines respectively). The y-axis shows the number in a given bin, relative to the total number in the respective sample. Counting errors are shown on the histogram for red spirals; due to the larger numbers of blue spirals the errors on those histograms are significantly smaller.

(open triangle) and quiescent galaxies (filled squares). We can clearly see that red spirals at all masses are unlikely to fall in the part of the $D_n(4000)$-Hδ_A plane which is occupied by star bursting or post star bursting galaxies (*i.e.,*. they are not above the main locus of points), but that a significant fraction do lie in the part of the plane in which galaxies are expected to have formed an insignificant fraction of their stars in the last 2 Gyrs (Kauffmann et al. 2003a), as well as in the mid-region where galaxies are expected to have mixed star formation histories (ie. a mix of recent and much older star formation). In contrast, many of the blue spirals (especially at the lower stellar masses) are in the region of the plane occupied by galaxies with mixed star formation histories, although there are also star-burst/post star-burst as well as more quiescent blue spirals.

Figure 5.7 illustrates clearly the mass dependence of spiral star formation history; lower mass spirals are more likely to have had recent star formation. This is true both for red and blue spirals in our sample, however in any given mass bin the red spirals have both lower Hδ_A and larger $D_n(4000)$ than equivalent blue spirals. It is clearly not stellar mass alone which is determining the SF history of the red spirals.

The range of stellar ages of red spirals are similar to early-type galaxies (at least to first order considering the range of $D_n(4000)$ – this does not account for metallicity effects which could cause a systematic offset) and they have not experienced recent burst of stars (in the last 1-2 Gyr); i.e. they are not post-starburst galaxies. However, the presence of spiral arms gives an indication that these red spirals must have recently been forming some stars, since spiral structures are expected to persist for only a short time after star formation completely ceases. The prevailing model for the origin of spiral structure
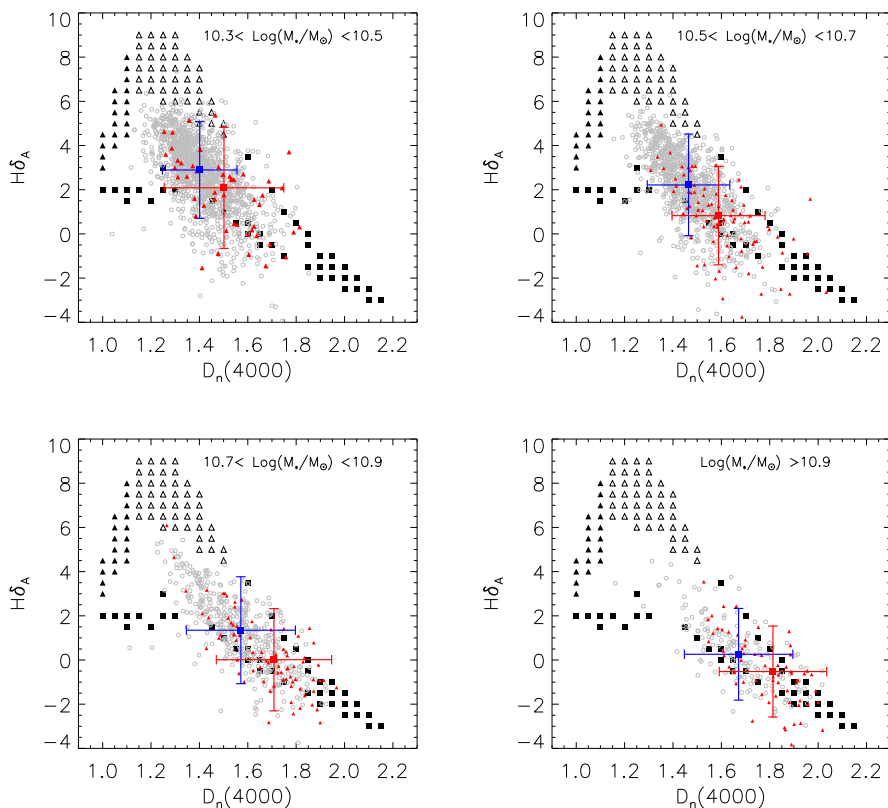
Figure 5.7 – Hδ_A versus $D_n(4000)$ is plotted for our sample of blue and red face-on, disky spirals. In each panel the blue spirals are shown by grey circles, and the red spirals are shown by red triangles. The red and blue error bars indicate the interquartile ranges for the red and blue spirals respectively. The different panels show the evolution with stellar mass, with the lowest mass galaxies at the upper left, down to the highest masses at the lower right. The red spiral galaxies on average show older stellar populations and less recent bursts of star formation in every mass bin. The data are plotted over galaxy models of Kauffmann et al. (2003a) showing regions covered by their starbursting (filled triangle), post starburst (open triangle) and quiescent (filled squares) galaxies.

in disk galaxies is the density wave theory proposed originally by Lin & Shu (1964). Discussing observations available at the time, which showed that galaxies without significant amount of interstellar gas do not have prominent spiral patterns, Lin & Shu (1964) suggest that any spiral structure, even if present in the old stellar population would not be visible, due to a lack of gas and star formation. More recent numerical simulations support this early picture of a relatively rapid fading of spiral arms after star formation ceases. For example Bekki et al. (2002) found that spiral arms persisted for only a few Gyrs after the gas which provides the reservoir for ongoing star formation was removed. Observationally Ishigaki et al. (2007) use spatially resolved spectroscopy of the passive spiral SDSS J074452.52+373852.7 to show that this galaxy probably stopped forming stars about 1-2 Gyrs ago - and it's spiral structure is still just visible. Follow-up integral field unit, and/or higher S/N spectroscopy for a representative sample of the red spirals could measure population ages and test this picture further. Such work is planned.

In the red spirals, current star formation is significantly reduced compared to the normal/blue spirals, *even at fixed stellar mass* but it does not appear to have completely stopped in all objects (as we will see below). Major amount of star formation cannot have ceased abruptly recently (as they are not post-starburst), or very long ago (more than a few Gyrs because of the presence of spiral arms). It is therefore possible to conclude that star formation either ceased abruptly in the red spirals between the post-starburst and spiral arm fading time scales (about one to a few Gyrs ago) or that there has been a gradual cessation of star formation in the red spirals over the past few Gyrs.

5.4 The Effect of Environment

The morphology-density relation (Dressler 1980) revealed that spiral galaxies favour lower density environments than early-types. However, recent work (Ball et al. 2008, Bamford et al. 2009, Skibba et al. 2009, Deng et al. 2009, e.g.) has shown that the colour-density relation is stronger than the morphology-density relation (ie. at a fixed morphology galaxies in higher density environments are redder, but at a fixed colour, there is little morphology-density dependence). We have already seen (Bamford et al. 2009, Skibba et al. 2009) that GZ1 red spirals are more common in high density regions (and conversely blue early-types are more common in low density regions; Schawinski et al. 2009b). There are also clear suggestions in both Bamford et al. (2009) and Skibba et al. (2009) that the peak of the red spiral distribution occurs in intermediate density regions. Therefore environment is clearly a candidate for driving the process which turns spirals red. As discussed in Section 5.1, various environmental mechanisms have been proposed to suppress star formation and turn galaxies red in high density regions. In this section we will consider the effect of environment on the red spirals in particular, looking at their preferred locations, and tracers of their star formation as a function of local density.
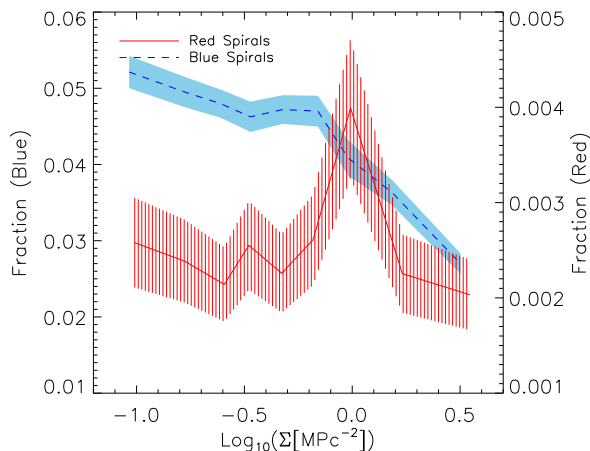
Figure 5.8 – Fraction of red spiral galaxies (red solid line) and blue spirals (blue dashed line) relative to all types of SDSS galaxies in our volume limited sample plotted versus environment as measured by Σ. The error regions are also shown; note that the binning is the same for both red and blue spiral samples, and adjusted to have $\sim$ 30 red spirals per bin.

5.4.1 The Environments of Red Spirals

In Figure 5.8, we present the fraction of galaxies in our red and blue spiral samples (relative to the full volume limited galaxy sample) versus the local galaxy density. We confirm the previous findings that red spiral fraction increases with local galaxy density, along with the well established observation that the fraction of blue (or normal) spirals decreases. This figure suggests that the red spiral fraction peaks at intermediate densities, around $\Sigma = 1$ Mpc^{-2}, inside the infall radius of a typical cluster, but not in their cores (see Figure 5 of Bamford et al. 2009 for the correlation of Σ with distance to the nearest cluster centre, this level of Σ corresponds to $d \sim 5 - 15$ Mpc depending on the richness of the cluster - for example it could be quite close in to a poor group, or much further away from a rich cluster). In order to look at the impact of close neighbours, and not just local density, we also consider the (projected) distance to the nearest neighbour (within 100 kms^{-1} in the SDSS DR6 Spectroscopic Galaxy Sample). Figure 5.9 shows the fraction of red and blue spirals in our face-on disky spiral sample as a function of this distance, showing that red spirals are a lot more likely to have close neighbours than blue spirals. (Of course Σ and the distance to the nearest neighbour are correlated - galaxies with a higher Σ will naturally have a nearer closest neighbour, and we have not attempted to disentangle the two measurements here.)
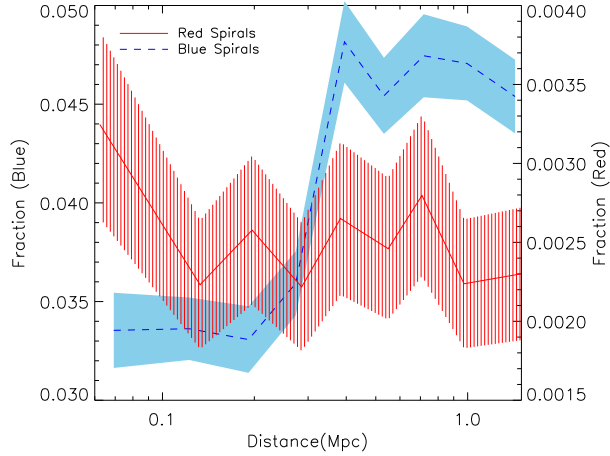
Figure 5.9 – Fraction of red spiral galaxies (red solid line) and blue spirals (blue dashed line) relative to all types of SDSS galaxies in our volume limited sample as a function of projected distance to nearest neighbour. The error regions are also shown; note that the binning is the same for both red and blue spiral samples, and adjusted to have ∼ 30 red spirals per bin.

5.4.2 Environmental Dependence of Star Formation

We now study the environmental dependence of star formation tracers in our samples of red and blue spirals. In Figure 5.10, we show the median equivalent widths (EW) of [OII] and Hα as a function of local galaxy density for both blue and red face-on disky spirals.

At all densities, red spirals have significantly lower but *non-zero* equivalent widths in these two tracers of ongoing star formation, but interestingly there are no significant trends with local density in either population, neither do we see any evidence for a change in the distribution of the quantities with environment (consistent with the findings of Bamford et al. 2008 for Hα in the galaxy population as a whole). There is perhaps a hint that the [OII] EW decreases with density for red spirals - a straight line fit to this trend has a ∼ 2σ significance (a slope of -1.0 ± 0.4). We also see a slight increase in the Hα EW in blue spirals at very high density, which may be related to interaction triggered star formation in this population - or perhaps a higher rate of AGN contamination in blue spirals in high density regions. This figure includes all galaxies, including those classified as AGN by their optical spectra (see Section 5.5 below), however in Section 5.5 we will show there is a higher AGN fraction in the red spirals than the blue, so removing AGN contamination from these lines will only make the difference between red and blue spirals stronger.

Figure 5.11 shows similar relations to that shown in Figure 5.10 for the tracers Hδ_A and $D_n(4000)$ (as discussed in Section 5.3, these are tracers of recent starbursts and the mean age of the stellar population respectively). Again we see that *at all densities* these indicators show less recent star formation and older stellar populations in red spirals than
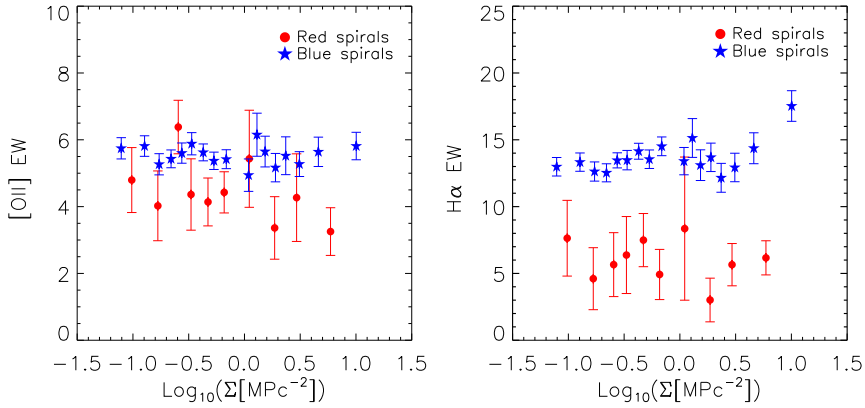
Figure 5.10 – The median equivalent widths of [OII] and Hα as a function of local galaxy density. Blue and red spirals are shown as blue stars/red dots respectively. Error bars show our estimate of the 1σ error on the median value.
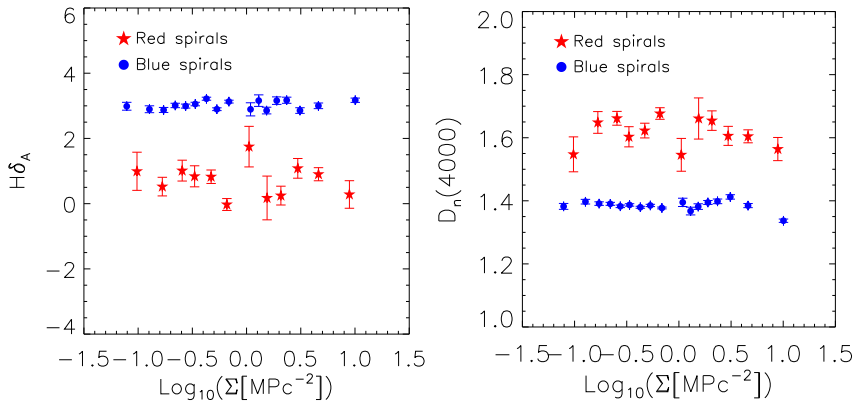

Figure 5.11 – Median values of Hδ_A (a tracer of recent star formation) and $D_n(4000)$ (a tracer of average stellar age) as a function of local galaxy density. Blue and red spirals are shown as blue stars/red dots respectively. Error bars show our estimate of the 1σ error on the median value.
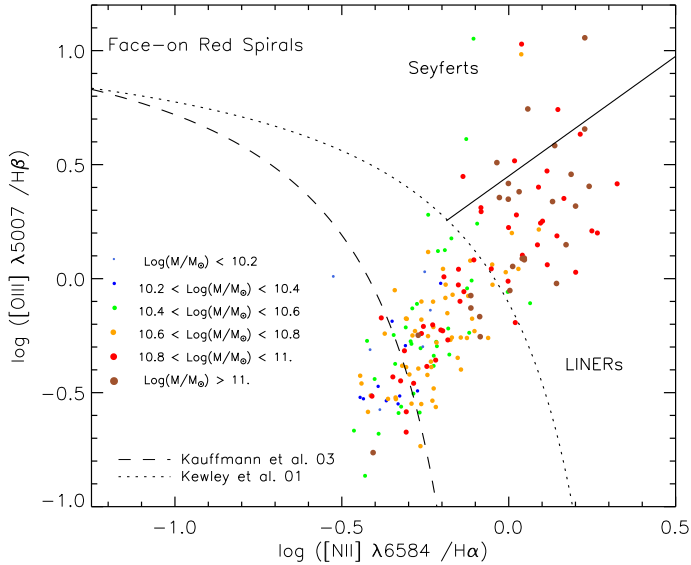
Figure 5.12 – Distribution of face-on disky red spiral galaxies in BPT diagram. The size and colour of the points indicates the stellar mass of the galaxies (as labelled). The diagonal dividing line for LINERS/Seyferts is taken from Schawinski et al. (2007).

blue spirals, and that there are no significant trends with density in either population. We have repeated this exercise using (projected) distance to the nearest neighbour, and find similar results.

Red spirals in all environments have lower rates of recent and on-going star formation than blue spirals. This suggests that despite the increased fractions of red spirals in high density regions, *environment is not the only factor in the shutting down of star formation in red spirals - i.e.,* the main physical process cannot only happen in high density regions (ruling out ram pressure stripping as the dominant process) and neither can it proceed faster in higher densities.

Our data are consistent with the process that turns spirals red being more likely to happen in high density regions as long as it is possible and proceeds in the same fashion in all environments. Both gentle interactions, and/or strangulation mechanisms could explain these observations.

5.5 The Impact of AGN

The most recent semi-analytic models for galaxy formation all invoke some form of AGN feedback which inhibits star formation in the most massive, red (early-type) galaxies
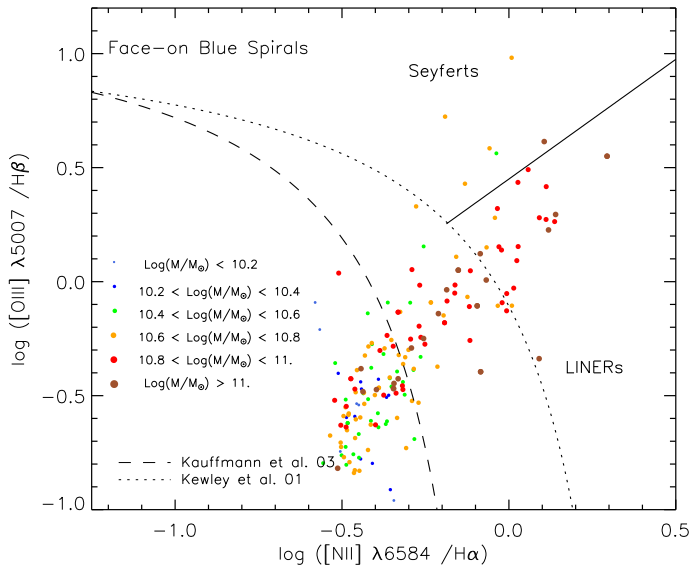
Figure 5.13 – Distribution on the BPT diagram of our sample of face-on disky blue spiral galaxies with the same number of objects in each mass bin as the red spirals shown in Figure 5.12 (selected randomly). The size and colour of the points indicates the stellar mass of the galaxies (as labelled).

(Granato et al. 2004, Silk 2005, Croton et al. 2006, Bower et al. 2006) in order to match the number counts and properties of these objects in the local universe. Observational evidence now exists to support this hypothesis, showing that the AGN fraction peaks in the region between the blue cloud and the red sequence (Schawinski et al. 2007, 2009a). Could AGN feedback be responsible for the shutdown of star formation in the red spirals?

We test this by using emission line diagnostic diagrams (Baldwin Phillips & Terlevich 1981, hereafter BPT; Veilleux & Osterbrock 1987, Kewley et al. 2001, 2006, Cid Fernandes et al. 2001) to probe the dominant source of ionisation in the red and blue spiral galaxies. For this study, we restrict our analysis to galaxies with greater than 2σ emission line detection for all four lines used in the BPT diagram (i.e. [OIII], Hα, [NII] and Hβ). Likewise, in order to reduce the effect of aperture bias of the SDSS 3″ fibre on the BPT diagram, we shift the lower redshift range of our sample up from $z > 0.03$ to $z > 0.05$. This reduces the sample size to 181 (60%) of the red spirals, and 3462 (66%) of the blue spirals.

Standard emission line diagnostic diagrams (e.g. Kauffmann et al. 2003b, Schawinski et al. 2007) are used to divide galaxies whose budget of ionising photons is dominated by current star formation (i.e. ionisation from OB associations) and those whose interstellar medium is excited by other processes. These other processes include AGN, but

also shocks and evolved stellar populations such as post-asymptotic giant branch (pAGB) stars, extreme horizontal branch stars, white dwarfs (Stasińska et al. 2008, Sarzi et al. 2009).

Observationally, the area between these two regions is populated by transition or composite objects where the total contribution to the ionising budget from star formation and other processes is roughly comparable. Kewley et al. (2001) give a prescription based on theoretical modelling of starburst galaxies which indicates the region of the diagram which can be explained by starburst emission (to the lower left of the line), while Kauffmann et al. (2003b) made an empirical fit to the observed separation between the populations in SDSS galaxies, which is often used as a lower limit for the location of AGN. Here as a short-hand, we will call objects to the upper right of the Kewley et al. (2001) line "AGN" (even if other processes may be more important in some objects), or sometimes "Seyfert+LINER" (as explained below), objects below the Kauffmann et al. (2003b) line "star-forming" and objects falling between the two lines "composite" objects.

The region dominated by ionization from processes other than star formation is furthermore divided into Seyferts and LINERs (low-ionisation nuclear emission-line regions; Heckman 1980). To split this region into Seyfert and LINER types we use the diagonal dividing line suggested by Schawinski et al. (2007). Objects in the Seyfert region are clearly identified as classical obscured (Type 2) Seyferts (*i.e.,* AGNs), while the LINER region is more controversial and possibly represents a heterogeneous population (see Section 5.6 of Ho 2008 for a recent review of possible sources of ionisation for LINERs). Recent results from the SAURON survey by Sarzi et al. (2009) show that the extended LINER emission seen in most SDSS fibre spectra (whose physical footprint corresponds to 2-3 kpc in the sample studied here) is inconsistent with a central point source for the ionisation, ruling out nuclear activity as the dominant source for the emission. Intriguingly, this is even the case when the presence of nuclear activity (e.g. from radio data) is detected.

The position of red spirals on a BPT diagram is illustrated in Figure 5.12 where points are coded (both in size and colour) by the stellar mass of the galaxy. Many more of the red spirals than the blue are placed above the Kewley et al. (2001) dividing line, indicating that they are not dominated by emission from star forming regions, but their gas must be ionised by other mechanisms ($30 \pm 4\%$[2] of all face-on disky red spirals in redshift interval of 0.05-0.085, compared to $4 \pm 1\%$ of blue spirals). As the plot indicates, a significant fraction of these galaxies are LINER-type ($82 \pm 12\%$). The remaining red spirals have many more composite objects than are found in the normal spiral population ($49 \pm 5\%$ compared to $15 \pm 1\%$ of blue spirals) with only a relatively small fraction being classed as starforming by the Kauffmann et al. (2003b) criterion ($21 \pm 3\%$ of red spirals compared to $81 \pm 2\%$ of blue spirals).

Part of these trends can be explained by the larger stellar masses of the red spirals, since it is well known that Seyferts and LINERs are more common in higher mass galaxies (e.g. Kauffmann et al. 2003b). Therefore for a fair comparison we construct a sample of blue spirals selected from the full blue spiral population in such a way that they have the

---

[2] Errors on the fractions given in this Section and elsewhere are $\sqrt{N}$ counting errors. This obviously breaks down when fractions approach zero or one, however for the purposes of this work the approximation of the errors is adequate.

same mass distribution as the red spirals (our "mass matched" blue spiral sample). We show 181 of these galaxies (*i.e.,* the same number as in the red spiral sample for ease of comparison) on the BPT diagram in Figure 5.13. Compared to this mass matched sample of blue spirals, red spirals are still significantly more likely to host optically identified Seyfert+LINER emission lines. Recall, $30 \pm 4\%$ of red spirals are above the Kewley et al. (2001) division and $48 \pm 5\%$ are in the composite region. In comparison we find only $7 \pm 1\%$ mass matched blue spirals in the Seyfert+LINER region and $23 \pm 1\%$ in the composite region. Red spirals are therefore ~4 times as likely to have Seyfert+LINER emission lines, and twice as likely to be composite objects when compared to similar blue spirals.

We plot in Figure 5.14 the observed fractions of Seyfert+LINER and starforming galaxies as a function of mass for both the red and blue spirals. For both sub-populations the Seyfert+LINER fraction increases with stellar mass, while the starforming fraction decreases, however as previously commented, at a given stellar mass red spirals are roughly twice as likely to be classifed as Seyfert/LINER, and less likely (roughly half as likely) to be classified as a starforming. There is a suggestion that the increase of Seyfert+LINER fraction with mass is also faster in the red spirals than it is in the blue spirals (at the expense of "composite" objects, since the starforming fractions are seen to decrease at approximately the same rate).

AGN fractions in all galaxies have generally been shown to be independent of environment (Miller et al. 2003, Sorrentino, Radovich & Rifatto 2006). However, recent work on X-ray selected AGNs does suggest an environmental dependence such that X-ray selected AGN are more common in groups than clusters (Arnold et al. 2009, this work also comments on the complete disjoint of X-ray selected and BPT selected AGN samples making such studies hard to compare) and Lee et al. (2009) also suggest AGN are less common in higher densities. Here, we see no signature of a density dependence of the Seyfert+LINER fraction of red spirals, although we note that the red spiral sample is quite small to divide in this way and covers only a limited range of densities.

Red spirals with emission lines which are not classified as coming from star formation are more likely to be classified as LINERS than similar objects in the blue spirals population, with $82 \pm 12\%$ of those in red spirals being LINERS versus $57 \pm 7\%$ in the mass matched blue spirals. This means the Seyfert fractions of red and blue spirals of the same mass are actually quite similar ($6 \pm 2\%$ of red spirals versus $3 \pm 1\%$ of blue spirals) - the main difference in the two populations appears to be in the LINER fraction which suggests a link between LINER emission and the shutting down of star formation in spiral galaxies. Overall $25 \pm 4\%$ of the red spirals are classified as having LINERs, while only $4 \pm 1\%$ of the (mass matched) blue spirals meet the LINER criteria. Interestingly in visually classified early type galaxies, Schawinski et al. (2007) also found that an increase in LINER fraction was associated with "stellar quiescence", while Smolčić (2009) studying radio loud AGN also found that the radio AGN in the red sequence were dominated by low ionization AGN which were classified as LINERs in the BPT diagram.

The Balmer line emission from even a small amount of star formation is expected to dominate any AGN emission. Schawinski et al. (2010) study the masking of AGN (Seyfert) emission in star forming galaxies and show that for AGN [OIII] luminosities
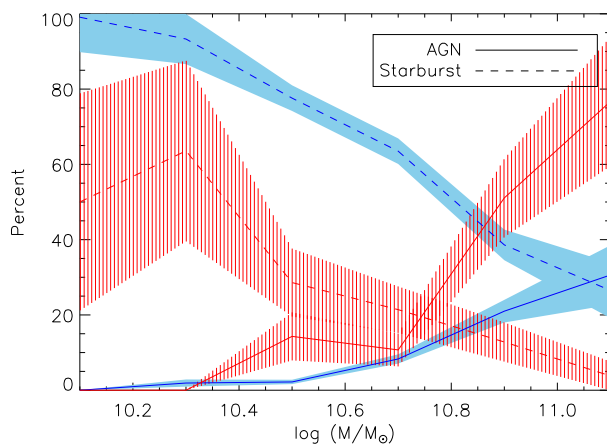
Figure 5.14 – Fraction of galaxies in a given stellar mass range which are classifed as "AGN" (Seyfert+LINER) or starforming from the BPT diagram (expressed as a percentage; note that the fraction classified as composites are not shown). The trends for blue spirals are shown with the blue lines, red spirals by the red lines. Shaded regions show the $\sqrt{N}$ counting errors on the fractions. Obviously these errors break down where the fractions approach zero or one, but give a reasonable estimate elsewhere.
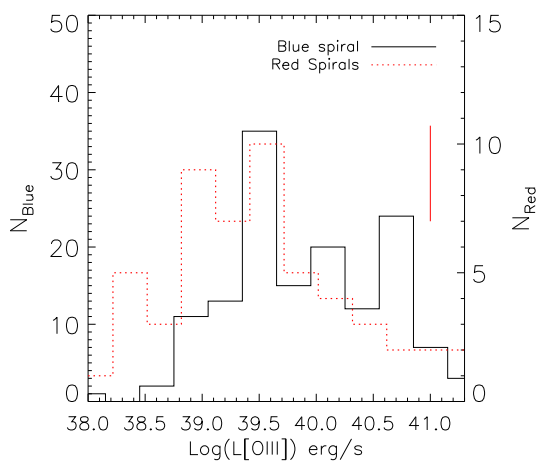

Figure 5.15 – Histogram of [OIII] luminosities of optically identified Seyferts and LINERS in the red spirals (red dotted line) and blue spirals from the mass matched sample (black solid line). The typical error on the red spiral histogram is indicated, offset for illustration purposes. Note that the *y*-axes are scaled such that the total area under each histogram is equal.

below 10^{39} erg s^{-1} most galaxies with star formation present will not be classified as AGN, and that only above 10^{40} erg s^{-1} will the sample of AGN identified by optical emission lines be reasonably complete in the blue cloud. We show in Figure 5.15 histograms of the [OIII] luminosities (extinction corrected using the method described in Lee et al. 2009) of both red and blue spirals (from the sample matched in mass with the red spirals) classified as having either Seyfert or LINER emission. This diagram suggests that there may be a difference in the luminosities of the emission lines identified in the two populations, such that fainter lines (below about $10^{39.3}$ erg s^{-1}) are found in the red spiral population which are not found in the blue spiral population. However, since the actual number of red spirals are small, the histograms do agree within the error.

If true, the above observation suggests that at least some LINERs are being revealed in the red spiral population, either because the emission lines are no longer dominated by star formation, or perhaps because the smaller amount of recent star formation means there is less dust shrouding the AGN. However the difference cannot account for all of the extra LINERs in the red spirals - *i.e.,* even at the luminous end of the distribution where we would not expect LINERs to be hidden in the blue spirals, we find more LINERs in red spirals (considering only emission with L[OIII]$> 10^{39}$ erg s^{-1} we find 24 ± 4% of the red spirals have emission not consistent with star formation compared to 7 ± 1% of the mass matched blue spirals), so we are able to say that at least high luminosity LINER emission is correlated with the shutting down of star formation in spiral galaxies.

Since we do not have either integral field observations or X-ray/radio data of red spirals, we present two alternative interpretations for the high LINER fraction in red spirals:

1. *Photoionisation from evolved stellar populations.*
   If we assume that the LINER emission in red spirals is mostly due to photoionisation from evolved stellar populations (e.g. Stasińska et al. 2008), then we can naturally account for the relatively higher fraction of LINERs in red compared to blue spirals in the following way: in massive galaxies, there is a substantial component of hard ionising radiation coming from evolved stellar populations, that would, in the absence of other factors, produce a weak LINER spectrum. In blue spiral galaxies, this signature is mostly overwhelmed by ongoing star formation, whereas in red spirals, where star formation has been gently quenched, no such competing source of photons is available.

2. *Low-luminosity nuclear activity.*
   If we assume that the LINER emission in red spirals is due to photoionisation from a low-luminosity, low-Eddington AGN (e.g. Kewley et al. 2006), we can ask about the role of this AGN in the evolution of red spirals. As suggested earlier, red spirals gently quenched their star formation in an extended process that began about 2 Gyr in the past. This in turn implies that the *current* LINER AGN can not be responsible for the suppression of star formation as it is happening now - with a substantial time delay after the quenching process. A similar, though shorter time delay is seen between the suppression of star formation and the start of substantial black hole growth (Schawinski et al. 2007). The LINER phase in red spirals, like in

early-types (Schawinski et al. 2007), seems to be a post-quenching phenomenon. The interesting question then becomes why the particular internal environments of red spiral galaxies that have already quenched their star formation is so conducive to low-level black hole growth.

Further observations of red spirals are required to fully distinguish between these two interpretations. Spatially resolved spectroscopic observations (long-slit or IFU) are needed to test whether the LINER emission in red spirals is spatially extended as it is in early-types. Deep X-ray or radio observations could yield evidence for ongoing black hole accretion.

5.6 Bar Fractions in Red/Blue Spirals

Even a cursory inspection of a small sample of images suggests that red spirals may have a significantly higher bar fraction than blue spirals (e.g. Figure 5.3). Two of us (BC and KLM) visually inspected the entire face-on disky red spiral sample, along with a similar number of the random mass matched blue spirals. We find that red spirals have an optical bar fraction of at least $67 \pm 5\%$ (raw fractions were 72% for BC and 67% for KLM) and up to 100% including more uncertain identifications, while the blue spirals have a bar fraction of only $27 \pm 5\%$ (28% from BC and 26% from KLM). These bar identifications used the SDSS *gri* images typically used by Galaxy Zoo, and were based on classic visual bar identification methods such as those used by de Vaucouleurs et al. (1991) to find a bar fraction of 25-30% in the RC3. More recent work on bar fractions in the literature (e.g. Jogee et al. 2004, Sheth et al. 2008, Barazza et al. 2008, Aguerri et al. 2009) use automated techniques for finding bars using elliptical isophote fitting. The two studies using SDSS data on ~2000 "disk" galaxies (Barazza et al. 2008, Aguerri et al. 2009) are most directly comparable to this study. Both however use automated techniques to identify disk/spiral samples based largely on concentration (Aguerri et al. 2009) and colour (Barazza et al. 2008, this study does also consider Sersic fits, but the final results are from colour selected "spirals" only), so we expect systematic differences with our visually identified face-on spiral sample and inparticular point out that red spirals by our definition will be completely absent from the Barazza et al. (2008) study, and extremely rare in Aguerri et al. (2009). The overall bar fractions found by Barazza et al. (2008), Aguerri et al. (2009) are comparable to our total bar fraction of ~50% (they find 50% and 45% of their disk samples hosting bars), but intriguingly both studies suggest a trend for bluer disk galaxies to be more likely to host bars, in direct contrast to the clear signal we find for red spirals to have more obvious bars in the *gri* images. It is not clear at this point if the difference in these trends is due to the sample selection or the bar identification method (although Aguerri et al. (2009) claim only a 7% difference between their automated bar finder and a visual check of their sample). A more detailed study of bar fractions in Galaxy Zoo galaxies as a function of various galaxy properties and considering possible biases on the visual bar identification method with *gri* images is being prepared using bar identifications for almost 30,000 spiral galaxies collected during

the second phase of Galaxy Zoo (GZ2; Masters et al. in prep.). For the purposes of this work, the huge increase in bar fraction between the blue and red spiral samples gives such a strong hint of a trend of bar fraction with colour (in the sense that red spirals are much more likely to host bars), that it suggests bars may be providing an important clue to the formation of the red spirals and therefore the impact of bars should be considered in a discussion of their possible origin.

In simulations of spiral galaxy formation, bars form quickly once a stable disk is formed, and are difficult to destroy (e.g. Debattista et al. 2006). However, the impact of higher density environments on bars is unclear. Tidal interactions might induce bar formation (eg. Hernquist & Mihos 1995), but they also act to heat the disks of spirals, and bars form most quickly in cold disks (eg. Toomre 1964). If external triggers such as tidal interactions are the most important source of bar instabilities, then the higher density environments of the red spirals may naturally lead to high bar fractions.

A possible explanation for the high bar fraction in red spirals could be that the bars themselves are at least partly responsible for the process which turned off star formation in these objects. Bars are known to be the most efficient way to redistribute material in the disks of galaxies (eg. Combes & Sanders 1981), by channelling gas into the central regions of the galaxy. Bars have been invoked (eg. Shlosman et al. 2000) as a way to feed gas to the central black hole - the increase in LINER fraction we observe in the red spirals could be a remnant of this process (if they are LINERs associated with AGN). Perhaps the bars in the red spirals have removed the cold gas from the disk and channelled it inwards where it has either been used as fuel for the AGN, or created a starburst. Of course, this starburst must have happened more than ~ 1 Gyr ago, to be consistent with our observation that red spirals are not post starburst objects, but if bars are as robust as simulations suggest then they would still persist for a long time after evidence of any bar triggered central starburst was removed.

5.7   Discussion

Since red spirals are observed at all density levels, the process which creates red spirals cannot be confined only to regions of high galaxy density; environment alone is not sufficient to determine whether a galaxy will become a red spiral or not. The lack of any clear correlation of the star formation rates of red spirals with environment, also indicates that red spirals in low density regions are similar to those in clusters making it more difficult to invoke only environmental processes in their formation. The process which turns spirals red may be more likely to occur in higher density regions, but must be possible, *and proceed in a similar way* in all environments, unless completely different mechanisms are responsible for red spirals in high and low density regions. That the red spiral population has a significantly higher mean mass than the population of blue spirals, also indicates that they are not uniformly sourced from the field population. However, perhaps the mass transition between red and blue spirals represents the lowest mass spiral which can retain its spiral structure under the influence of environmental effects which shut off its star formation (*i.e.,*. low mass blue spirals might pass through the red spiral phase very quickly,

or experience both morphological and colour transformation at the same time).

We suggest that rather than representing an intermediate stage of environmental transformation, red spirals could be "old spirals" who through normal internal evolution have already used up their reservoirs of gas - perhaps aided by the redistribution of gas due to a bar instability. We suggest that part of the reason they are found to be more common in higher density regions is because the initial density fluctuations decoupled from the Hubble flow earlier there (see Bromm et al. 2009, for a review) and galaxies started assembling at much earlier times (Cooper et al. 2009) in dense environments so have had longer to use up their gas. Such objects would naturally be found at the high mass end of the galaxy distribution as they have been assembling for a long time. Red spirals presumably become less common in the highest densities where strong environmental processes are more important and may have already changed all spirals into early type galaxies.

It has been shown that for a typical spiral (*i.e.,* with typical star formation rates) to use up all its gas within a Hubble time requires that there is no infall of additional gas from its halo (Larson et al. 1980). Therefore strangulation (or removal of gas from the outer halo - a process which would be more common in satellite galaxies in higher density regions, but can happen even in low mass groups Kawata & Mulchaey 2008) is probably required and could by itself create a population of red spirals preferentially found in intermediate density regions (if those in the highest densities were further disrupted). It was observed by Skibba et al. (2009) that the Galaxy Zoo red spirals are preferentially satellite galaxies in massive halos (while blue spirals are preferentially the central galaxy in a low mass halo). This observation supports the idea of strangulation as an important part of the mechanism which creates red spirals. In this scenario they are accreted onto the massive halo as a blue spiral, after which their outer halo gas reservoirs are gently stripped by the main galaxy, and no further accretion of cold gas can take place. (Bekki et al. 2002) showed that in such a scenario spiral arms would persist for a few Gyrs after the gas was removed. Lower mass spirals presumably are disrupted by gravitational effects in the massive halo and cease to display spiral features, so this model can explain both the mass and environmental distribution of the red spirals.

If other environmental processes are responsible for turning spirals red, they must be very gentle and happen over long timescales. Continued tidal interactions and/or minor mergers (*i.e.,* galaxy harrassment, Moore et al. 1999) could be responsible - these would heat the disk gas above the density required for star formation, but not remove it. If tidal interactions are also responsible for creating bars (e.g. Hernquist & Mihos 1995) the high bar fraction we observe could be a remnant of this (although the bars may still help to shut down star formation by re-distributing and heating the gas themselves).

Several authors (e.g. Goto et al. 2003, Wolf et al. 2009) have suggested that red (or passive) spirals are the progenitors of S0 galaxies. The origin of the S0 galaxies has been an ongoing debate for more than three decades (Dressler 1980, Moran et al. 2007). S0s are often argued to be too bright and massive and have too large bulge-disk ratios to simply be faded spirals (e.g. Burstein et al. 2005), but Moran et al. (2007) argue that they have linked passive spirals with young S0s in two $z \sim 0.5$ clusters and that a combination of gas stripping and gentle galaxy-galaxy interactions could be responsible for the change, and Driver et al. (2007) show that bulge light is severely attenuated by dust in spiral galaxies

which may help to resolve the bulge-disk ratio issue.

There is only one observation in this paper which is immediately in conflict with the idea of the Galaxy Zoo red spirals being the progenitors of S0s. We observe a high optical bar fraction in the face-on disky red spirals, while S0s have a significantly lower bar fraction (Aguerri et al. 2009). Our disky red spirals cannot simply turn into S0s as their spiral arms fade, as the bar instability would remain much longer than the arms. However in this work we have purposely selected red spirals with small bulges. Perhaps S0s form from red spirals with large bulges. Further study of the red Galaxy Zoo spirals with large bulges may clear up this issue.

5.7.1   Future Directions

This work has used optical data from SDSS to reveal the star formation history, dust content, AGN properties, environments and morphologies of a unique sample of intrinsically red disk dominated spiral galaxies. It is clear that significantly more information can be obtained from other surveys, wavelengths, and from future theoretical modelling, which will help to shed light on the dominant physical process which formed these objects.

If strangulation is the dominant process forming red spirals they should have almost no residual neutral hydrogen (alternatively, if tidal interactions are responsible by gently heating the disk gas, and thus lowering its density below the threshold for star formation, they should still contain significant quantities of HI). This will be tested using data from the ALFALFA blind HI survey (Giovanelli et al. 2005) which covers much of the SDSS footprint.

The debate over the nature of the LINER emission could be solved by moving to other wavelengths to reveal the AGN or by obtaining spatially resolved optical spectra to look at the extent of the emission. Deep targeted X-ray observations would reveal objects currently growing their black holes. Unfortunately, currently available public X-ray surveys are too small an area or at too low luminosity levels to be of use. (For example the XMM Cluster Survey, XCS (Romer et al. 2001) has only 220 of the blue spirals and 6 of the red spirals studied here in its footprint (1 blue spiral is detected), while the ROSAT All-Sky Survey, RASS (Voges et al. 1999) has a high flux limit). Current radio continuum surveys (for example the NRAO-VLA Sky Survey, NVSS; Condon et al. 1998) could also reveal ongoing black hole accretion, or radio-loud AGN.

More sophisticated modelling of the spectral information (for example from VESPA, Tojeiro et al. 2009) would provide time resolved star formation histories and more reliable stellar masses. Spatially resolved spectra would additionally allow separate study of the star formation histories of the different regions of these galaxies, and provide dynamical information possibly helpful in determining the role of the bars.

The interpretation of the increased bar fraction in the red spirals is made difficult by the wide range of suggestions of the impact of bars on spiral galaxies. More detailed modelling of spiral galaxies with bars would be extremely helpful in interpreting those observations. We can also use Galaxy Zoo 2 data (which asks for a more detailed classification of among other things barred galaxies) to study the more general properties of a large sample of galaxies with bars. For example studying the environmental dependence

of barred galaxies compared to non-barred galaxies would shed light on the role tidal interactions play in bar formation.

5.8   Summary and Conclusions

We study the interesting population of red, or passive, spiral galaxies found by the Galaxy Zoo project. We identify from these red spirals a population of intrinsically red true disk dominated spirals by limiting the sample in inclination (to reduce the impact of dust reddening), requiring that spiral arms be visible, and removing bulge dominated systems using the SDSS parameter `fracdeV`. We compare this sample to blue spirals selected in the same way and find that:

- Red spirals are more likely to be more massive, luminous galaxies than blue spirals. They represent an insignificant fraction of the spiral population at masses below $10^{10}M_\odot$ but are significant at the highest masses, showing that *massive galaxies are red regardless of morphology*.

- At the same mass as blue spirals, face-on red spirals do not have larger amounts of dust reddening (as measured by the Balmer decrement), therefore their red colours indicate an ageing stellar population not an increased dust content.

- Red spirals have lower (but not zero) rates of ongoing and recent star formation when compared to blue spirals. This is partly related to their higher average mass, however *at a fixed mass, red spirals still have less recent star formation than blue spirals*.

- As previously observed, red spirals are more common at intermediate local densities (around, or just inside the infall regions of clusters). They are also observed to be more likely than blue spirals to have close neighbours.

- Red spirals in all environments have lower rates of recent and on-going star formation than blue spirals, and there are no significant trends of the star formation rates with environment when spirals are split into red/blue. Clearly the process which creates red spirals is not confined to regions of high galaxy density. So *environment alone is not sufficient to determine whether a galaxy will become a red spiral or not*.

- Red spirals are more than four times more likely to be classified as Seyfert+LINER/composite objects from their optical spectra than blue spirals. This is partly due to the higher masses of red spirals but is still observed when they are compared to a blue spiral sample selected to have the same mass distribution. We find that a small fraction of low luminosity AGN are being revealed as the star formation is turned off in the red spirals, but this is not enough to account for all the difference. Most of the difference comes from an increased fraction of LINER-like emission ($82 \pm 12\%$ of Seyfert/LINERs found in red spirals are LINERs compared to $57 \pm 7\%$ in blue spirals).

- Red spirals have significantly higher bar fractions than blue spirals (70% versus 27%), suggesting that bar instabilities and the shutting down of star formation in spirals are correlated.

We propose three possible origins for the red spiral population studied in this work and suggest the most likely explanation is that a combination of the three accounts for the shutting down of their star formation while they retain their spiral structure:

1. Perhaps red spirals are just old spirals which have used up all of their gas. They are found preferentially in intermediate density regions because structures first starts to form at the peaks of the dark matter distribution, but in the centres of clusters spiral morphologies cannot stand up to the environmental disturbances. Red spirals then represent the end stages of spiral evolution irrespective of environment (and in the absence of major mergers) - the spiral version of "downsizing".

2. Perhaps red spirals are satellite galaxies in massive dark matter halos. In this scenario, they are accreted onto the halo as a normal blue spiral and have experienced either strangulation (where the gas in their outer halos has been gently stripped off, and no further cold gas has been allowed to accrete) or harassment (heating their disk gas and preventing further star formation). Low mass spirals would probably be disrupted in this process and so are not observed as red spirals.

3. Perhaps red spirals evolved from normal blue spirals which had bars that were particularly efficient at driving gas inwards. This removed gas from the outer disk and turned the spiral red. If it triggered star formation in the central regions it must have occured more than ~ 1 Gyr ago since red spirals are not post starburst galaxies.

The red spirals in this work probably cannot be the progenitors of S0s as they have a significantly higher bar fraction than in observed in the S0 population. S0s may however be the end product of red spirals with larger bulges than we have studied here.

5.9 Appendix A: Sample of Data Tables

We provide in this Appendix samples of the data tables we make available electronically listing important information (all based on SDSS data) for both our red (Table 5.1) and blue (Table 5.2) face-on disky spiral samples. In both tables columns are (1) SDSS objid; (2 and 3) RA and Dec in J2000 decimal degrees; (4) Redshift; (5) Absolute r-band (Petrosian) magnitude, M_r; (6) $(g - r)$ colour (from model magnitues); (7) "redness", defined as the distance in magnitudes from the blue limit of the $(g - r)$ verses M_r red sequence (see Equation 5.1 in Section 5.2.1); (8) axial ratio, $\log(a/b)$ from the r-band isophotal measurement; and (9) fracdeV; the fraction of the best fit light profile made up by a de Vaucouleur profile (as opposed to an exponential disk).

Table **5.1** – A Sample of Face-On, "Disky" Red Spirals. (The full table is available in the online version of the paper.)

SDSS objid	RA (J2000 deg)	Dec (J2000 deg)	Redshift	M_r	$(g - r)$	"Redness"	$\log(a/b)$	fracdeV
587731186741346415	1.218164	0.351724	0.0833	-21.26±0.01	0.695±0.020	0.040	0.144	0.42
588015509270364319	2.277073	0.042422	0.0735	-21.75±0.01	0.701±0.021	0.036	0.143	0.46
587731187227926598	3.718539	0.634254	0.0642	-21.15±0.01	0.756±0.039	0.103	0.042	0.00
587731187227933141	3.771462	0.642945	0.0621	-21.50±0.01	0.662±0.017	0.002	0.179	0.32
588015508734148754	3.789492	-0.366536	0.0661	-22.18±0.01	0.687±0.018	0.013	0.070	0.40
⋮	⋮	⋮	⋮	⋮	⋮	⋮	⋮	⋮

Table 5.2 – A Sample of Face-On, "Disky" Blue Spirals. (The full table is available in the online version of the paper.)

SDSS objid	RA (J2000 deg)	Dec (J2000 deg)	Redshift	M_r	$(g - r)$	"Redness"	$\log(a/b)$	fracdeV
587727225690259639	0.276560	-10.400263	0.0754	-21.41±0.01	0.434±0.020	-0.225	0.084	0.12
587727225690259660	0.325174	-10.426144	0.0767	-21.03±0.02	0.561±0.028	-0.090	0.078	0.07
587730773888991473	0.566363	14.671807	0.0834	-20.91±0.02	0.503±0.035	-0.145	0.106	0.06
588015510343385206	0.665200	0.942673	0.0807	-22.38±0.01	0.632±0.018	-0.046	0.079	0.22
588015510343516321	0.941711	0.854914	0.0611	-20.69±0.01	0.378±0.023	-0.266	0.185	0.00
⋯	⋯	⋯	⋯	⋯	⋯	⋯	⋯	⋯

Bibliography

Adelman-McCarthy, J. K., et al. 2008, ApJS, 175, 297

Aguerri, J. A. L., Méndez-Abreu, J., & Corsini, E. M. 2009, A&A, 495, 491

Arnold, T. J., Martini, P., Mulchaey, J. S., Berti, A., & Jeltema, T. E. 2009, ApJ, 707, 1691

Baldry, I. K., Balogh, M. L., Bower, R. G., Glazebrook, K., Nichol, R. C., Bamford, S. P., & Budavari, T. 2006, MNRAS, 373, 469

Baldwin, J. A., Phillips, M. M., & Terlevich, R. 1981, PASP, 93, 5

Ball, N. M., Loveday, J., & Brunner, R. J. 2008, MNRAS, 383, 907

Balogh, M. L., Morris, S. L., Yee, H. K. C., Carlberg, R. G., & Ellingson, E. 1999, ApJ, 527, 54

Bamford, S. P., Rojas, A. L., Nichol, R. C., Miller, C. J., Wasserman, L., Genovese, C. R., & Freeman, P. E. 2008, MNRAS, 391, 607

Bamford, S. P., et al. 2009, MNRAS, 393, 1324

Barazza, F. D., Jogee, S., & Marinova, I. 2008, ApJ, 675, 1194

Bekki, K., Couch, W. J., & Shioya, Y. 2002, ApJ, 577, 651

Binette, L., Magris, C. G., Stasińska, G., & Bruzual, A. G. 1994, A&A, 292, 13

Bruzual, G., & Charlot, S. 2003, MNRAS, 344, 1000

Boselli, A., & Gavazzi, G. 2006, PASP, 118, 517

Bower, R. G., Benson, A. J., Malbon, R., Helly, J. C., Frenk, C. S., Baugh, C. M., Cole, S., & Lacey, C. G. 2006, MNRAS, 370, 645

Bromm, V., Yoshida, N., Hernquist, L., & McKee, C. F. 2009, *Nature*, 459, 49

Bundy, K., et al. 2006, ApJ, 651, 120

Bundy, K., et al. 2010, ApJ (submitted; arXiv:0912.1077)

Burstein, D., Ho, L. C., Huchra, J. P., & Macri, L. M. 2005, ApJ, 621, 246

Cid Fernandes, R., Heckman, T., Schmitt, H., González Delgado, R. M., & Storchi-Bergmann, T. 2001, ApJ, 558, 81

Combes, F., & Sanders, R. H. 1981, A&A, 96, 164

Condon, J. J., Cotton, W. D., Greisen, E. W., Yin, Q. F., Perley, R. A., Taylor, G. B., & Broderick, J. J. 1998, AJ, 115, 1693

Conselice, C. J. 2006, MNRAS, 373, 1389

Cooper, M. C., Gallazzi, A., Newman, J. A., & Yan, R. 2009, MNRAS, 1868 (arXiv:0910.0245)

Cooray, A. 2005, MNRAS, 363, 337

Cortese, L., & Hughes, T. M. 2009, MNRAS, 400, 1225

Cowie L. L., & Songaila A. 1977, *Nature*, 266, 501

Croton, D. J., Norberg, P., Gaztañaga, E., & Baugh, C. M. 2007, MNRAS, 379, 1562

Croton, D. J., et al. 2006, MNRAS, 365, 11

Debattista, V. P., Mayer, L., Carollo, C. M., Moore, B., Wadsley, J., & Quinn, T. 2006, ApJ, 645, 209

Deng, X.-F., He, J.-Z., Wu, P., & Ding, Y.-P. 2009, ApJ, 699, 948

de Vaucouleurs, G., de Vaucouleurs, A., Corwin, H. G., Jr., Buta, R. J., Paturel, G., & Fouqué, P.

1991, Third Reference Catalogue of Bright Galaxies, Springer, New York, NY (USA).

Dressler, A. 1980, ApJ, 236, 351

Driver, S. P., Popescu, C. C., Tuffs, R. J., Liske, J., Graham, A. W., Allen, P. D., & de Propris, R. 2007, MNRAS, 379, 1022

Gallazzi, A., et al. 2009, ApJ, 690, 1883

Giovanelli, R., et al. 2005, AJ, 130, 2598

Glazebrook, K., et al. 2004, *Nature*, 430, 181

Gnedin, O. Y. 2003, ApJ, 582, 141

Goto, T., Yamauchi, C., Fujita, Y., Okamura, S., Sekiguchi, M., Smail, I., Bernardi, M., & Gomez, P. L. 2003, MNRAS, 346, 601

Granato, G. L., De Zotti, G., Silva, L., Bressan, A., & Danese, L. 2004, ApJ, 600, 580

Gunn, J. E., & Gott, J. R. I. 1972, ApJ, 176, 1

Heckman, T. M. 1980, A&A, 87, 152

Hernquist, L., & Mihos, J. C. 1995, ApJ, 448, 41

Ho, L. C. 2008, ARA&A, 46, 475

Hopkins P. F., et al. 2009, MNRAS, 397, 802

Hughes T. M., & Cortese, L. 2009, MNRAS, 396, L41

Ishigaki, M., Goto, T., & Matsuhara, H. 2007, MNRAS, 382, 270

Jogee, S., et al. 2004, ApJ, 615, L105

Lee J. H., Lee M. G., Park C., Choi Y.-Y. 2008, MNRAS, 389, 1791

Kauffmann, G., et al. 2003a, MNRAS, 341, 33

Kauffmann, G., et al. 2003b, MNRAS, 346, 1055

Kawata, D., & Mulchaey, J. S. 2008, ApJ, 672, L103

Kewley, L. J., Groves, B., Kauffmann, G., & Heckman, T. 2006, MNRAS, 372, 961

Kewley, L. J., Dopita, M. A., Sutherland, R. S., Heisler, C. A., & Trevena, J. 2001, ApJ, 556, 121 (Ke01)

Lamastra, A., Bianchi, S., Matt, G., Perola, G. C., Barcons, X., & Carrera, F. J. 2009, A&A, 504,73

Larson, R. B., Tinsley, B. M., & Caldwell, C. N. 1980, ApJ, 237, 692

Lin, C. C., & Shu, F. H. 1964, ApJ, 140, 646

Lintott, C. J., et al. 2008, MNRAS, 389, 1179

Liske, J., Lemon, D. J., Driver, S. P., Cross, N. J. G., & Couch, W. J. 2003, MNRAS, 344, 307

Lee, J. H., Lee, M. G., Park, C., & Choi, Y.-Y. 2009, MNRAS (in press: arXiv:0911.4386)

Lee, J., & Pen, U.-L. 2007, ApJ, 670, L1

Mahajan, S., & Raychaudhury, S. 2009, MNRAS, 400, 687

Maraston, C. 2005, MNRAS, 362, 799

Masters, K. L., et al. 2010, MNRAS, (in press; arXiv:1001.1744)

Mignoli, M., et al. 2009, A&A, 493, 39

Miller, C. J., Nichol, R. C., Gómez, P. L., Hopkins, A. M., & Bernardi, M. 2003, ApJ, 597, 142

Moore, B., Lake, G., Quinn, T., & Stadel, J. 1999, MNRAS, 304, 465

Moran, S. M., Ellis, R. S., Treu, T., Salim, S., Rich, R. M., Smith, G. P., & Kneib, J.-P. 2006, ApJL, 641, L97

Moran, S. M., Ellis, R. S., Treu, T., Smith, G. P., Rich, R. M., & Smail, I. 2007, ApJ, 671, 1503

Okamoto, T., Nemmen, R. S., & Bower, R. G. 2008, MNRAS, 385, 161

Osterbrock, D. E. *Astrophysics of Gaseous Nebulae and Active Galactic Nuclei*, 1989, University

Science Books, Mill Valley, CA

Romer, A. K., Viana, P. T. P., Liddle, A. R., & Mann, R. G. 2001, ApJ, 547, 594

Salimbeni, S., et al. 2008, A&A, 477, 763

Sarzi, M., et al. 2009, MNRAS, (in press, arXiv:0912.0275)

Schawinski K., et al. 2006, *Nature*, 442, 888

Schawinski K., Thomas D., Sarzi M., Maraston C., Kaviraj S., Joo S.-J., Yi S. K., Silk J. 2007, MNRAS, 382, 1415

Schawinski K., et al. 2009a, ApJ, 690, 1672

Schawinski K., et al. 2009b, MNRAS, 396, 818

Schawinski K., et al. 2010, ApJ, (in press: arXiv:1001.3141)

Sheth, K., et al. 2008, ApJ, 675, 1141

Shlosman, I., Peletier, R. F., & Knapen, J. H. 2000, ApJL, 535, L83

Silk, J. 2005, MNRAS, 364, 1337

Silk, J., & Rees, M. J. 1998, A&A, 331, L1

Simien, F., & de Vaucouleurs, G. 1986, ApJ, 302, 564

Simon, P., Hetterscheidt, M., Wolf, C., Meisenheimer, K., Hildebrandt, H., Schneider, P., Schirmer, M., & Erben, T. 2009, MNRAS, 1058

Skibba, R. A., et al. 2009, MNRAS, 399, 966

Smolčić, V. 2009, ApJ, 699, L43

Sorrentino, G., Radovich, M., & Rifatto, A. 2006, A&A, 451, 809

Stasińska, G., Vale Asari, N., Cid Fernandes, R., Gomes, J. M., Schlickmann, M., Mateus, A., Schoenell, W., & Sodré, L., Jr. 2008, MNRAS, 391, L29

Stasińska, G., Cid Fernandes, R., Mateus, A., Sodré, L., & Asari, N. V. 2006, MNRAS, 371, 972

Strauss, M. A., et al. 2002, AJ, 124, 1810

Tojeiro, R., Wilkins, S., Heavens, A. F., Panter, B., & Jimenez, R. 2009, ApJS, 185, 1

Toomre, A., & Toomre, J. 1972, ApJ, 178, 623

Toomre, A. 1964, ApJ, 139, 1217

Tremonti, C. A., et al. 2004, ApJ, 613, 898

van den Bergh, S. 1976, ApJ, 206, 883

Veilleux, S., & Osterbrock, D. E. 1987, ApJS, 63, 295

Voges, W., et al. 1999, A&A, 349, 389

Walker, I. R., Mihos, J. C., & Hernquist, L. 1996, ApJ, 460, 121

Wolf, C., Gray, M. E., & Meisenheimer, K. 2005, A&A, 443, 435

Wolf, C., et al. 2009, MNRAS, 393, 1302

Nederlandse samenvatting

Geschiedenis

Aan het begin van de twintigste eeuw was het algemeen aanvaard dat onze Melkweg bijna het hele Universum vulde. Pas in de jaren '20 van de vorige eeuw werden er aanwijzingen gevonden voor sterrenstelsels buiten onze Melkweg. Pioniers zoals Edwin Hubble vonden bewijs dat veel van de waargenomen "planetaire nevels" eigenlijk sterrenstelsels buiten onze Melkweg zijn. Grote aantallen sterrenstelsels zijn sindsdien gevonden en waargenomen. Om op een effectieve manier over deze objecten te kunnen praten werd door astronomen besloten om sterrenstelsels te classificeren aan de hand van hun structuur en vorm, of kortweg morfologie. Eén van de eerste classificatieschema's werd geïntroduceerd door Edwin Hubble (1926), en is bekend geworden als Hubble's Stemvork. Dit schema, dat vandaag de dag nog steeds gebruikt wordt, onderscheidt sterrenstelsels als elliptisch, lenticulair, spiraalvormig, of onregelmatig. Elke klasse kan op zijn beurt weer opgesplitst worden in subklassen aan de hand van extra kenmerken, zoals bijvoorbeeld de aanwezigheid van een balk. De verschillen tussen deze type sterrenstelsels reflecteren de verschillen in hun fysieke eigenschappen. Sinds de eerste classificaties is het doel van astronomen geweest om deze sterrenstelsels en hun fysieke eigenschappen in meer detail te bestuderen.

Men ontdekte dat spiraalvormige sterrenstelsels andere sterpopulaties hadden dan elliptische. De hoeveelheid gas en recente gevormde nieuwe sterren in spiraalstelsels zijn verschillend ten opzichte van elliptische sterrenstelsels, en verder hebben ze blauwere kleuren. De sterpopulaties van elliptische sterrenstelsels zijn oud, met rodere kleuren, en elliptische stelsels zijn gemiddeld zwaarder dan spiraalstelsels (Kauffmann et al. 2003, Blanton et al. 2005). Over het algemeen vormen observationele eigenschappen zoals kleur, vorm, helderheid, huidige sterformatie, stellaire en dynamische massa, circulaire snelheid, en snelheidsdispersie de empirische grondslag voor het onderscheiden en het bestuderen van de onderliggende fysica in sterrenstelsels (zie bijvoorbeeld Blanton & Moustakas 2009).

De diversiteit aan verschillende soorten sterrenstelsels in het nabije Universum leidde tot de vraag waar deze verschillende types vandaag komen. Astronomen proberen daarom het onderliggende verhaal te ontdekken over de vorming en evolutie van sterrenstelsels, vanuit zowel theoretisch als observationeel oogpunt. Het theoretische raamwerk afkomstig uit de jaren 1960-70 (bijv., Eggen et al. 1962, Sandage et al. 1970, Press & Schechter 1974), beschrijft de vorming van sterrenstelsels vanuit gravitationele instabiliteiten, ontstaan uit perturbaties in de verdeling van donkere materie en condensatie van gas.

Volgens de huidige theorie voor de vorming van sterrenstelsels geldt dat, zodra een

halo van donkere materie ineenstort, het gas binnenin deze halo zeer snel afkoelt. Deze afkoeling vermindert de druk van het gas; om te voorkomen dat al het gas naar het centrum valt is een hoeveelheid impulsmoment nodig (ontstaan uit getijdenkrachten in het jonge Universum). Dit zorgt ervoor dat het gas samenkomt in een roterende schijf (zie bijvoorbeeld, Mo et al. 1998). Echter, verschillende theoretische modellen gebruiken verschillende aannames voor de dichtheidsprofielen van de halo van donkere materie, evenals voor de initiële afhankelijkheid van het gas-impulsmoment op de halo van donkere materie. Het is onduidelijk of het gas-impulsmoment kan veranderen met de tijd, of hoe sterformatie en feedback processen een effect hebben op de structuur van sterrenstelsels, zoals bijvoorbeeld hun afmeting.

Er zijn kortweg twee verschillende scenario's voor de formatie van de *bulge* (centrale verdikking) van spiraalsterrenstelsels. Men gaat ervan uit dat ze gevormd worden door een botsing van twee sterrenstelsels, of door de instabiliteit van de schijf. De formatie van de bulge door middel van een botsing van twee sterrenstelsels, vereist de aangroei van gas op een later moment om een schijf te vormen rond de bulge. Daarom is het goed mogelijk dat in dit scenario de kern en de schijf verschillende sterpopulaties hebben. Bij een scenario met een instabiele schijf zal materiaal dat al aanwezig is de bulge vormen. Toch zijn er nog veel extra aannames nodig (bijvoorbeeld feedback processen) om een compleet beeld te krijgen over de vorming en evolutie van typische spiraalsterrenstelsels.

De vorming van elliptische sterrenstelsels wordt ook niet goed begrepen. Een van de mogelijke mechanismen voor de formatie van deze elliptische sterrenstelsels is door middel van een botsing van twee sterrenstelsels. Uit simulaties van botsende schijfsterrenstelsels is gebleken dat globale eigenschappen van elliptische sterrenstelsels gereproduceerd kunnen worden (bijv., Hernquist 1992). Ondanks het feit dat dit algemene model veel simpele karakteristieken voor deze sterrenstelsels goed kan voorspellen blijven er veel aspecten die niet overeen komen met waarnemingen.

Om die reden blijven directe waarnemingen essentieel om de formatiemodellen voor sterrenstelsels te testen. Het is van groot belang dat er niet alleen wordt gekeken naar complete verzamelingen van nabije sterrenstelsels, maar ook naar grote verzamelingen van sterrenstelsels op het moment dat ons Heelal jonger was. Om deze reden is het identificeren van de eerste en verste sterrenstelsels steeds belangrijker geworden sinds de midden-jaren '70. In de jaren '90 verschoof de waarneembare grens van verre sterrenstelsels naar roodverschuiving $z \sim 1 - 4$, wat overeenkomt met een terugkijktijd van $\sim 7 - 12$ miljard jaar. Dankzij zeer diepe waarnemingen zijn in de laatste tien jaar de verzamelingen hoge-roodverschuiving sterrenstelsels enorm gegroeid en is de observationele limiet verder vooruitgeschoven naar $z \sim 10$ (Bouwens et al. 2012).

Schalingrelaties

Een van de belangrijkste onopgeloste problemen in de astrofysica is het begrijpen van de formatie en evolutie van sterrenstelsels. Er zijn veel complementaire manieren om de evolutie van sterrenstelsels te bestuderen en om de connectie te vinden tussen verre
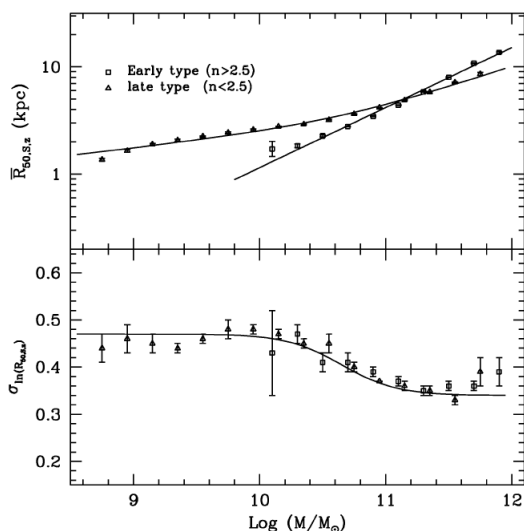
sterrenstelsels en sterrenstelsels in het huidige Heelal. De meeste geaccepteerde metho-des zijn of gericht op de evolutie in de helderheids- of massafuncties van sterrenstelsels, of op de evolutie in de hoeveelheid sterformatie of stellaire massa dichtheid, of op de evolutie van de waargenomen schalingrelaties van sterrenstelsels. Neem bijvoorbeeld de helderheidsfunctie; deze beschrijft het aantal sterrenstelsels met een bepaalde helderheid. Dit kan op zijn beurt gebruikt worden om het totale aantal sterrenstelsels te bepalen op verschillende tijdstippen. Op deze manier geeft de evolutie van de helderheidsfunctie met roodverschuiving ons essentiële informatie om de evolutie van sterrenstelsels te begrijpen.

Sterrenstelsel tonen een grote verscheidenheid aan fysieke eigenschappen zoals hel-derheid, stellaire massa, afmeting en rotationele snelheid. Sterrenstelsel vertonen goed gedefinieerde schalingrelaties tussen deze eigenschappen. Voor spiraalstelsels, bijvoor-beeld, wordt het verband tussen de helderheid en de rotationele snelheid beschreven door de 'Tully-Fisher' relatie (Tully & Fisher 1977). Dit is kortweg de correlatie tussen de dynamische massa en de helderheid van sterrenstelsels. De relatie tussen de snelheids-dispersie en de helderheid van elliptische sterrenstelsel is bekend als de 'Faber-Jackson' relatie (Faber & Jackson 1976), waarbij elliptische sterrenstelsels met een hogere snel-heidsdispersie helderder zijn.

Het is essentieel om deze schalingrelaties te bestuderen over een groot bereik in rood-verschuiving. Dit kan ons helpen vast te stellen hoe sterrenstelsels zich bewegen binnen deze relatie en maakt het dus mogelijk om verschillende evolutionaire modellen te tes-ten. Over het algemeen geldt dat het bepalen van de helling, nulpunt en spreiding rond deze relaties op verschillende tijdstippen van fundamenteel belang is om de verschillende modellen voor de formatie voor sterrenstelsels te testen.

Echter, er zijn een aantal uitdagingen om de benodigde precisiewaarnemingen te ver-krijgen. Om bijvoorbeeld de rotationele snelheid of snelheidsdispersie te meten voor sterrenstelsels op hoge roodverschuiving zijn diepe spectroscopische observaties vereist. Het verkrijgen van een groot aantal van deze metingen is een tijdsintensief proces. Daar komt bij dat als sterrenstelsels minder helder worden de onzekerheid van deze metingen toeneemt. Om deze reden is het bepalen van correlaties tussen sommige eigenschappen van sterrenstelsels bijzonder moeilijk op hoge roodverschuiving.

Van deze schalingrelaties is degene tussen de stellaire massa en de afmeting van ster-renstelsels bijzonder belangrijk. De afmeting van een sterrenstelsel kan worden bepaald door middel van waarnemingen in een enkele filter (fotometrie). De stellaire massa van een sterrenstelsel kan ook robuust worden gemeten met behulp van fotometrie op vele verschillende golflengtes en precieze modellen voor sterpopulaties. Het is daarom minder moeilijk om een goede schatting te maken voor de afmeting en massa als het gaat om grote hoeveelheden sterrenstelsels op hoge roodverschuiving in vergelijking met de spec-troscopische metingen zoals eerder beschreven. Daar komt bij dat de stellaire massa en de afmeting van sterrenstelsels twee belangrijke ingrediënten zijn voor het karakteriseren van sterrenstelsels en belangrijke fysische betekenis hebben. Het bestuderen van deze eigenschappen op verschillende tijdstippen in het Heelal zal bijdragen in het onderzoek naar hoe de structuur van nabije sterrenstelsels is ontstaan en wat de eigenschappen zijn van hun voorgangers op hoge roodsverschuiving. In het kort, het kan ons helpen om de verschillende evolutionaire scenario's voor de formatie en evolutie van sterrenstelsels af
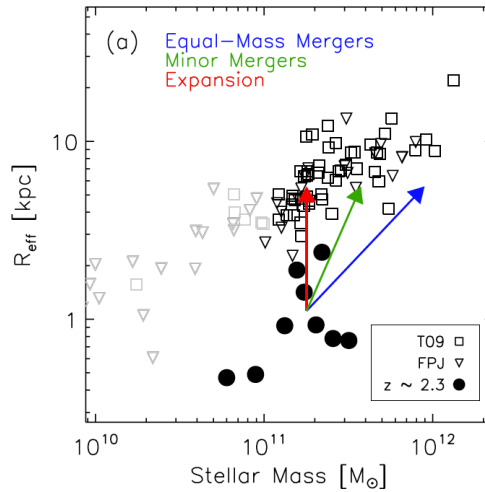
Figuur 1 – De stellaire massa-grootte relatie voor spiraal- en elliptische sterrenstelsels in de SDSS (bovenste paneel) en de dispersie in de afmetingen als een functie van stellaire massa (onderste paneel) uit de studie door Shen et al. (2003).

te bakenen.

De relatie tussen de stellaire massa en de afmeting van sterrenstelsels in het huidige Heelal is voor het eerst beschreven in Kauffmann et al. (2003), en goed gekarakteriseerd door Shen et al. (2003), die gebruik maken van een verzameling sterrenstelsels in de Sloan Digital Sky Survey (SDSS). Het bovenste paneel van Figuur 1 laat de massa-grootte relatie zien voor spiraal- en elliptische sterrenstelsels zoals bestudeerd door Shen et al. (2003). De relatie is verschillend voor spiraal- en elliptische sterrenstelsels. Op hoge massa geldt dat spiraalsterrenstelsels een steilere relatie hebben in vergelijking met elliptische. Dit reflecteert verschillen in de formatiemechanismen van elk type sterrenstelsel. De spreiding in de afmetingen (onderste paneel van Figuur 1) laat ook een variatie zien als functie van de stellaire massa: de spreiding neemt af voor massievere sterrenstelsels.

De eerste baanbrekende onderzoeken naar de afmetingen van sterrenstelsels op hoge roodverschuiving werden gedaan in de jaren '90 (bijv., LBGs op $z \sim 3$ door Giavalisco et al. (1996), of Lilly et al. (1998) sterrenstelsels tot $z \sim 1$). Echter, de resultaten van deze verschillende onderzoeken waren niet in overeenkomst, mede veroorzaakt door de moeilijkheidsgraad om een groot aantal van deze sterrenstelsels te meten op hoge roodverschuiving, maar ook door selectie-effecten voortkomend uit de oppervlakte helderheid limiet. Deze studies naar de helderheid-grootte relatie van sterrenstelsels verbeterden later door het gebruik van diepe waarnemingen vanaf de grond en vanuit de ruimte. Deze onderzoeken lieten zien dat sterrenstelsels in het jonge Heelal kleiner waren in vergelijking met sterrenstelsels met een vergelijkbare massa/helderheid in het lokale Universum

Figuur 2 – De relatieve distributie van de stellaire massa en afmeting van dode sterrenstelsels op $z \sim 2$ en in het nabije Universum. De verschillende pijlen laten de voorspelling zien voor elk model als functie van roodverschuiving. (Figuur afkomstig uit Bezanson et al. (2009)).

(bijv., Trujillo et al. 2006b, Zirm et al. 2007, van Dokkum et al. 2008). Dit betekent dat de afmeting van sterrenstelsels, gegeven een stellaire massa, moeten groeien in tijd met maximaal een factor ~ 6.

Dit proces van groei in de afmeting van sterrenstelsels kan verschillend zijn voor elke type en kan variëren op elk tijdstip. Stervormende sterrenstelsels op hoge roodverschuiving (bijv op $z \sim 2$), hebben een grotere fractie gas per stellaire massa in vergelijking met hun tegenhangers op lage roodverschuiving (e.g., Erb et al. 2006). Een mogelijke verklaring voor de groei in afmeting voor deze sterrenstelsels zou kunnen worden gegeven door de aanwas van gas op de schijf wat weer omgezet wordt in nieuwe sterren (bijv., Law et al. 2012).

Verschillende observaties hebben verder laten zien dat elliptische sterrenstelsels op hoge roodverschuiving ook significant kleiner zijn dan stelsels op lage roodverschuiving. Er zijn twee belangrijke vraagstukken voor deze sterrenstelsels. Allereerst: hoe zijn deze sterrenstelsels gevormd op hoge roodverschuiving? En ten tweede: hoe verhouden deze sterrenstelsels zich tot hun lokale analogen. De formatie van deze compacte dode sterrenstelsels wordt nog nauwelijks begrepen. Niettemin zijn verscheidene mechanismen voorgesteld om de groei in afmeting van deze sterrenstelsels te verklaren. De vaakst voorkomende voorbeelden zijn door middel van grote botsingen, kleine botsingen, of adiabatische expansie (bijv., Khochfar & Silk 2009, Naab et al. 2009, Bezanson et al. 2009, Fan et al. 2008). Deze verschillende mechanismen kunnen de stellaire massa en massa-profielen op verschillende manier veranderen.

De waargenomen stellaire massa-grootte relatie voor deze massieve dode sterrenstel-

sels zou kunnen helpen om te bepalen welke van de verschillende modellen de juiste is. Botsingen van sterrenstelsels met weinig gas en met dezelfde massa (grote botsingen) kunnen de afmeting en de stellaire massa van deze sterrenstelsels verdubbelen. Kleine botsingen zorgen voor een grotere groei in afmeting ten opzichte van de groei in stellaire massa, en dit proces conserveert de centrale dichtheid en snelheidsdispersies. Het adiabatische expansie scenario voorspelt dat een grote hoeveelheid materiaal efficiënt wordt uitgestoten door middel van een vorm van feedback (bijv. Quasar feedback). Echter, in dit proces wordt de centrale dichtheid en de snelheidsdispersie van een elliptisch sterrenstelsel veranderd (zie Figuur 2 voor meer details). Door de verschillende schalingrelaties op verschillende roodverschuivingen (tijdstippen) te vergelijken met de resultaten van simulaties kunnen we de verschillende scenario's toetsen voor de vorming en evolutie van sterrenstelsels.

Dit Proefschrift

De onzekerheden geassocieërd met de waargenomen eigenschappen van sterrenstelsels kunnen worden verminderd door extra observaties die gebruik maken van diepere data met grotere gebieden aan de hemel en goed gedefinieerde selectiemethoden. Metingen op meerdere golflengtes zijn krachtige instrumenten voor dit soort studies. Door gebruik te maken van de snelle recente ontwikkeling op het gebied van infrarood metingen van sterrenstelsels, en met behulp van aanvullende optische en nabije-infrarood waarnemingen, is het nu mogelijk geworden om de eigenschappen van verschillende typen sterrenstelsels over een groot bereik in roodverschuiving te bestuderen en de observationele limieten verder vooruit te schuiven tot het tijdstip van de formatie van de eerste sterrenstelsels ($z \sim 10$).

In dit proefschrift ligt de focus op het bestuderen van de structurele eigenschappen van sterrenstelsels, zoals hun afmetingen en helderheidsprofielen, en te analyseren hoe deze eigenschappen veranderen als functie van tijd. In het bijzonder bestuderen we de stellaire massa-grootte relatie van sterrenstelsels tussen $z = 7$ en $z = 0$, door gebruik te maken van recente diepe observaties in het nabije infrarood. De combinatie van diepe optische en nabije-infrarood waarnemingen maakt het mogelijk om de spectra van sterrenstelsels te karakteriseren over een groot bereik in roodverschuiving, in het bijzonder tijdens de piek in de sterformatie activiteit ($z \sim 2$). Het bestuderen van de eigenschappen van sterrenstelsels en het bepalen van de schalingrelaties op verschillende tijdstippen is van groot belang om onderscheid te kunnen maken tussen de verschillende fysische processen die invloed zouden kunnen hebben op de vorming van deze sterrenstelsels (bijv., aanwas van gas op sterrenstelsels, of grote/kleine botsingen en feedback effecten).

Hoofdstuk 2: In dit hoofdstuk presenteren we de eerste studie naar de evolutie van de afmetingen van sterrenstelsels die gebruik maakt van een verzameling van objecten met een spectroscopische roodverschuiving tussen $z \sim 0.5 - 2.5$ in het GOODS-Noord veld. Over het algemeen maken studies slechts gebruik van fotometrische roodverschuivingen; door stelsels met spectroscopische roodverschuivingen te gebruiken kunnen we

belangrijke selectie effecten verwijderen. Verder bestuderen we de afmeting van verschillende type UV-heldere stervormende sterrenstelsels op hoge roodverschuiving. Dat wil zeggen, we meten de afmetingen van verschillende soorten sterrenstelsels, zoals Lyman Break Sterrenstelsels, BM/BX sterrenstelsels, en Lyman Break analogen, op een roodverschuiving van $z \sim 1$. Bovendien vergelijken we de afmetingen van deze sterrenstelsels met andere type stervormende sterrenstelsels, zoals BzKs en sub-millimeter sterrenstelsels (SMGs). De positie van deze sterrenstelsels ten opzichte van de massa-grootte relatie kan aanwijzingen geven over hun connectie met andere soorten sterrenstelsels.

Hoofdstuk 3: Met de komst van de recent geïnstalleerde Wide Field Camera 3 (WFC3) op de *Hubble Space Telescope* en de daarmee gemaakte ultradiepe nabije-infrarood observaties van de Hubble Ultra Deep Field (HUDF), is het mogelijk geworden om een groot aantal nieuwe kandidaat-Lyman Break Sterrenstelsels (LBGs) te identificeren, reikend tot de beginfase van de formatie van de eerste sterrenstelsels (bijv. tot $z \sim 8$). De meeste onderzoeken zijn vooral gericht geweest op de evolutie van de helderheidsfunctie, stellaire massa, en mate van sterformatie in LBGs op deze roodverschuiving (bijv., Bouwens et al. 2011, Gonzalez et al. 2011). Echter, de stellaire massa-grootte relatie van deze sterrenstelsels op $z \gtrsim 4$ zijn nog niet in detail onderzocht. In dit Hoofdstuk maken we daarom gebruik van de ultra diepe WFC3 nabije-infrarood en IRAC observaties in de HUDF en het Early Release Science (ERS) veld, om de stellaire massa-grootte relatie van LBGs te bestuderen tot een roodverschuiving van $z \sim 7$.

Op $z \gtrsim 4$ wordt optisch licht roodverschoven naar het mid-infrarood, wat een probleem is voor het bepalen van stellaire massa's. Met de Spitzer Space Telescope is het mogelijk om gevoelige fotometrische metingen uit te voeren op deze golflengtes; helaas zorgt zijn grote PSF voor problemen, doordat sterrenstelsels optisch vermengen. Echter, er bestaan robuuste technieken om voor deze versmeerde objecten individueel de fotometrie te bepalen, wat weer gebruikt kan worden om de stellaire massa van sterrenstelsels op hoge roodverschuiving accuraat te bepalen (Labbé et al. 2006). Bovendien hebben we de afmetingen van deze stelsels gemeten met een meettechniek (uitgaande van een Sérsic model) die consistent is met de manier waarop dit veelal wordt gedaan op lagere roodverschuivingen. Met behulp van deze methoden zijn we in staat om de stellaire massa-grootte relatie te bepalen voor sterrenstelsels tot $z \sim 7$.

Hoodstuk 4: De stellaire massa-grootte relatie van sterrenstelsels in het huidige Heelal kan gebruikt worden als een basislijn voor de evolutie van de afmetingen van sterrenstelsels als een functie van tijd. Om die reden bestuderen we in dit Hoofdstuk de massa-grootte relatie voor een verzameling van sterrenstelsels op $z = 0.01 - 0.02$, waarbij de verzameling is opgedeeld aan de hand van algemene classificatiemethoden. We bestuderen verschillende technieken om de afmetingen van sterrenstelsels te bepalen: een enkel Sérsic profiel, een twee-componenten Sérsic profiel, en een non-parametrische methode, met als doel om de systematische onzekerheid te kwantificeren die bij elke techniek hoort. Tot slot testen de we de potentiële systematische fouten in de bepaling van afmetingen op hoge roodverschuiving door onze sterrenstelsels op $z = 0$ artificieel te verschuiven naar $z = 1$ en de metingen opnieuw uit te voeren, gebruik makend van een enkel Sérsic profiel.

Hoofdstuk 5: Vele studies hebben aangetoond dat de meerderheid van sterrenstelsels een kleur-morfologie relatie vertoont, zowel op lage als hoge roodverschuiving. In andere woorden, morfologische transformatie en het einde van sterformatie zouden gecorreleerd kunnen zijn. Echter, er is een populatie van rode, dode spiraal sterrenstelsels (zonder enige vorm van sterformatie), als eerste opgemerkt door van den Bergh (1976) en Couch et al. (1998) , die niet binnen deze relatie past.

In dit Hoofdstuk maken we gebruik van zorgvuldig geselecteerde schijfstelsels (op $z \sim 0$) uit de Galaxy Zoo morfologische catalogus (visueel geselecteerd), om een verzameling op te bouwen van echt passieve schijf sterrenstelsels. We proberen de verschillende fysische processen te onderzoeken die verantwoordelijk kunnen zijn voor stopzetten van de sterformatie in deze rode passieve spiraalsterrenstelsels zonder de spiraal morfologie te verstoren. We bestuderen de eigenschappen van het stof en stellaire populaties in deze sterrenstelsels in vergelijking tot blauwe, nog levende spiraalstelsels. Bovendien analyseren wij het effect van de omgeving op deze sterrenstelsels en onderzoeken we of er aanwijzingen zijn voor AGN activiteit. Verder onderzoeken wij de fractie van objecten met bepaalde morfologische kenmerken (zoals bijvoorbeeld een balk) in rode en blauwe spiraalstelsels.

Curriculum vitae

I was born on September 16, 1980 in Shiraz, Iran. My interest in Astronomy grew with me from the time I was a child and started when I read Isaac Asimov's book. During high school, my keen desire triggered me to register at the first Iranian Astronomical Institute for learning elementary Astronomy. The total solar eclipse in 1995 in Iran and the passage of the Comet Hale-Bopp a year later inspired me to choose the subject of physics at university (1998) in order to find the answers to thousands questions which arose in my mind. My first year of studying at Shiraz University ended with the last total eclipse of twentieth century (Aug 11 1999). This event led me to become a member of a student group at Biruni Observatory, Shiraz University. This Observatory was active with the photometry and data analysis of variable stars, especially eclipsing binary stars using photomultiplier tube (PMT) with its 20" telescope.

During my undergraduate studies I attended small workshops, seminars and schools to learn more about astronomy. While I was giving lectures in astronomy to the general public and visitors of the Biruni Observatory, I also became acquainted with photometry of variable stars and started to collaborate with postgraduate students o data acquisition, photometry and photometric data reduction of eclipsing binary stars. I then decided to do my B.Sc. project on a photometry of a delta scuti star under the supervision of Prof. N. Riazi of Shiraz University. This experience introduced me to a wide area of observational Astronomy and gave me an impulse to be enthusiastic in the field of observations.

The association with Biruni Observatory was continued after completing the B.Sc. (2002) and I had the opportunity to work with a CCD camera. Because of lack of experiences with CCD imaging in my country, I tried to obtain experience with CCD imaging and compiling information from different sources. The result of this effort was then published as a book (in Persian) in 2006 on "Digital Imaging and Astronomical Image Processing" in 263 pages, in which I have introduced the structure of CCDs, practical ways for CCD imaging, photometry with CCDs, using digital cameras for astronomical imaging and introduction to image processing. The book is at the level of advance amateurs and undergraduate students.

In September 2006, I started a master program in Astronomy at the university of Sussex (Brighton, UK). I carried out my Msc project on the "Extraction of luminous red galaxies (LRGs) from the Dark Energy Survey (DES) simulation", under supervision of Dr. Kathy Romer. After my Msc., I started to collaborate with the Galaxy Zoo team, specifically, Prof. R. C.Nichol and Dr. K. Masters at the Institute of Cosmology and Gravitation (ICG) in Portsmouth, on studying the properties of red spiral galaxies.

In January 2009, I started my PhD in Astronomy at the Sterrewacht Leiden (Leiden University) under the supervision of Prof. Marijn Franx and Dr. Rik Williams funded by the Marie Curie Initial Training Network of the European Union (ELIXIR). My research has been dedicated to investigate how structural properties of galaxies such as their sizes,

surface brightness profiles and other physical properties change with time.

During my PhD, I participated in the many schools, such as three ELIXIR Schools in Astrium (Germany), ESA/ESTEC (Netherlands) and also a summer school in Heidelberg (Germany) and NOVA fall school (Netherlands) and Oort Workshop (Leiden). I also presented my work in workshops, conferences and seminars, specifically in Lorentz Center (Leiden), Oxford (UK), Madrid (Spain), Cambridge (IoA, UK) and Durham (UK).

I would like to continue my career in Astrophysics and I be will considering upcoming postdoc opportunities.

Acknowledgements

The completion of this thesis would not have been possible without the encouragement, support and help of many people. I would like to express my gratitude to all those who gave me the support, inspiration and help to complete my thesis.

First, my family, which I am deeply indebted. Mahsan, your precious words, love, kindness and encouragement brighten every day of my life. Mom and Dad, you are great supporters. You taught me to be hard working, strong, patient and to be committed to achieve the best. Mom and Dad, thank you for all of your love and valuable things you have provided for me and all your dedication in every step of my life. My sisters, Najmeh and Negin, you always gave me a lot of energy. I am very grateful to them.

My group members have been great supporters and help in many ways. Shannon, I am very fortunate to have you as a friend and officemate, in one word, you are awesome. Jesse, thank you for all your help, especially with the Dutch summary. Daniel, thanks for useful discussions. Mattia, I am really happy for being in the same group. Adam, I always enjoyed brightening discussions with you. Rychard and Ivo, thanks for all your help. Ryan, thank you for the great supports at the beginning of my PhD. Maaike, thanks for your friendship and all your help especially in my beginning days in the Netherlands. Rik, I very much appreciated your stimulating suggestions, encouragement and all your valuable hints all the time.

I am grateful to my other friends and colleagues in Leiden. Ali, Maryam, thanks for your support and encouragements. Sean, I really enjoyed sharing our office with you and I will definitely miss the useful conversations and discussions with you. Joakim, thanks for your hospitality. Akbar, Behnam, Hossein and Behrooz, Maryam Hashemi, I am very grateful for your friendship and warm and supportive words over the last four years.

I am very grateful to Ali Dariush whose helps, encouragements and friendship mean a lot for me. I also would like to thank Kathy Romer, for inspiring me and encourage to continue my study. Karen, Bob, I really enjoyed and learned a lot by collaborating with you.

I also would like to acknowledge a large amount of support from the staff and computer group at Leiden Observatory over the last four years. I had also few visits to Carnegie Observatories in Pasadena, and benefit from the staff and supports scientist there. Thank you all.